DISS. ETH NO. 26074

EXACT NONLINEAR MODEL REDUCTION IN STRUCTURAL DYNAMICS

A thesis submitted to attain the degree of

DOCTOR OF SCIENCES of ETH ZURICH

(Dr. sc. ETH Zurich)

presented by

STEN LAURENT PONSIOEN

M.Sc. Mechanical Engineering,
Delft University of Technology

born on 06.03.1991

citizen of
the Kingdom of the Netherlands

accepted on the recommendation of

Prof. Dr. George Haller (ETH Zurich)
Prof. Dr. Eleni Chatzi (ETH Zurich)

2019

Acknowledgments

I wish to acknowledge my adviser Prof. Dr. George Haller, for the advice and support I received during my doctoral studies. I couldn't have wished for a better and more inspiring mentor. Thank you George for all the opportunities that you gave me. I am truly honored that I was able to work with you and learn from you.

I would like to thank all the members of the Haller group for the great time we spent together for the last three years. Specifically I would like to thank Mattia Serra for being a great inspiration on a professional and personal level. Additionally, I would like to thank Tiemo Pedergnana for his outstanding work during our collaborations.

I want to express my deepest gratitude to my parents, Bou and Wil, and my sister, Roos, for always being there for me.

Above all, I would like to thank my beautiful wife, Alexandra, for her unconditional love and support during our whole adventure together, starting all the way back in Trieste. Without you by my side, this journey would not have been so incredible. I dedicate this milestone to you.

Abstract

In this thesis, we develop the tools to construct exact reduced-order models for nonlinear mechanical systems using spectral submanifold (SSM) theory. SSMs are the unique, smoothest, nonlinear continuations of spectral subspaces of the linearized, unforced limit of a mechanical system. We demonstrate that the reduced dynamics on a two-dimensional SSM serves as an exact, single-degree-of-freedom reduced-order model that can be constructed for each vibration mode of the full nonlinear system.

In the first part of this work, we discuss an automated computational methodology for computing two-dimensional SSMs in autonomous nonlinear mechanical systems. We construct the SSMs up to arbitrary orders of accuracy, using the parameterization method. Additionally, we develop an automated a posteriori error estimation feature that enables a systematic increase in the orders of the SSM computation until the required accuracy is reached.

We then extend the work from the autonomous setting to the non-autonomous setting. We show how spectral submanifold theory can be used to extract forced-response curves (FRCs) of high-degree-of-freedom periodically forced mechanical systems. We use multivariate recurrence relations during the construction of the SSMs for computational efficiency, providing a major-speed up relative to the autonomous SSM algorithm. The increase in computational efficiency allows us to close the gap between analyzing typical lower-dimensional academic examples and larger systems obtained using a finite-element-method package. We find that our SSM-based forced-response predictions remain accurate in high-dimensional systems, in which numerical continuation of the periodic response, using a collocation method or harmonic balance method, is becoming computationally expensive.

In the last part of the thesis we show how SSM theory, in combination with the developed computational engine, can be used to provide analytic predictions for the response of periodically forced multi-degree-of-freedom mechanical systems. These predictions include an explicit criterion for the existence of isolated forced responses that will generally be missed by numerical continuation techniques. The analytic predictions can be refined to arbitrary precision via an algorithm that does not require the numerical solutions of the mechanical system. We illustrate these results on low- and high-dimensional nonlinear vibration problems.

Sommario

In questo lavoro di tesi, sviluppiamo gli strumenti per definire modelli ridotti per la descrizione di sistemi meccanici tramite l'utilizzo della teoria delle sottovarietà spettrali (SSM). Le SSM sono le più regolari, ed uniche, continuazioni nonlineari dei sottospazi spettrali del sistema lineare non forzato. Dimostriamo che la dinamica ridotta su un SSM bidimensionale costituisce un modello ridotto esatto, ad un grado di libertà, che puo essere costruito per ogni modo di vibrare del sistema non lineare completo.

Nella prima parte della tesi, discutiamo una metodologia computazionale automatizzata per calcolare SSM bi-dimensionali in sistemi meccanici nonlineari autonomi. Costruiamo SSM con ordine di accuratezza arbitrariamente alto tramite l'utilizzo del metodo di parametrizzazione. In aggiunta, abbiamo sviluppato un approccio per identificare a posteriori l'accuratezza del modello ridotto ed aumentare il grado di approssimazione di conseguenza fino a raggiungere l'accuratezza desiderata.

Nel seguito, estendiamo i risultati a sistemi meccanici non autonomi. Mostriamo come la teoria SSM può essere usata per estrarre curve di risposta in frequenza per sistemi con elevati gradi di libertà forzati periodicamente. Utilizzando relazioni di ricorrenza multivariate nella costruzione di SSMs, otteniamo una migliore efficienza computazionale e velocità di calcolo significativamente maggiori rispetto al caso dei sistemi autonomi. Questo incremento in efficienza ci permette di analizzare sistemi ad elevato numero di gradi di libertà come quelli prevenienti da simulazioni ad elementi finiti. Le curve di risposta in frequenza basate sulla teoria SSM rimangono accurate anche in sistemi con molti di gradi di libertà, dove schemi numerici di continuazione delle risposte periodiche che utilizzano metodi di collocazione o bilancio armonico diventano computazionalmente molto costosi.

Nell'ultima parte della tesi mostriamo come la teoria delle SSM, insieme allo schema computazionale sviluppato, può essere utilizzata per calcolare predizioni analitiche della risposta di sistemi meccanici a diversi gradi di libertà sottoposti a forzante periodica. Tali predizioni includono un criterio esplicito riguardo l'esistenza di risposte forzate isolate che sono generalmente non rilevate da tecniche computazionali numeriche. Le predizioni analitiche possono essere raffinate a piacimento tramite un algoritmo che non richiede la risoluzione numerica del sistema. Illustriamo tali risultati in sistemi meccanici nonlineari sia con pochi che con molti gradi di libertà.

Contents

Chapter 1

General Introduction

1.1 Motivation and background

Modern-day nonlinear mechanical systems, constructed, e.g., using a finite-element method package, can contain thousands of degrees of freedom. As a direct consequence, obtaining a qualitative and quantitative understanding of the response of such systems can be troublesome or even impossible.

In order to overcome this obstacle, model-reduction methods are often employed to reduce the total dimension of the system, as it will be easier to interrogate the reduced-order model (ROM) and extract information of interest. However, the question that arises is how well do these reduced-order models capture the response of the full system.

In linear conservative mechanical systems, one often reduces the full system by projecting the equations of motion on a linear invariant subspace $\mathcal{E}$, spanned by a collection of the linear vibration modes of the system at the origin. As this space is invariant, an initial position of the system in $\mathcal{E}$ will result in a motion of the system that remains in $\mathcal{E}$. As a result, the response of the system can be expressed as a summation of the vibration modes that span the invariant subspace, effectively reducing the dimension of the full system to the dimension of $\mathcal{E}$. However, if the system is given an initial position that is outside of $\mathcal{E}$, then there is no a priori reason for the response of the system to remain restricted to $\mathcal{E}$, therefore rendering the originally proposed reduced model invalid. We illustrate this concept in Fig. 1.1.

In a general nonlinear setting, the response of the system can no longer be represented by a linear summation of the vibration modes. However, the concept of decomposing nonlinear oscillations in analogy with linear modal analysis has been an active field of research for several decades. The concept of a *nonlinear normal mode* (NNM) was first introduced by Rosenberg [1] and defined as a synchronous periodic oscillation of the system that reaches its maximum in all modal coordinates at the same time. A more geometrical approach to the concept of an NNM was given by Shaw and Pierre [2], envisioning a NNM as a two-dimensional invari-

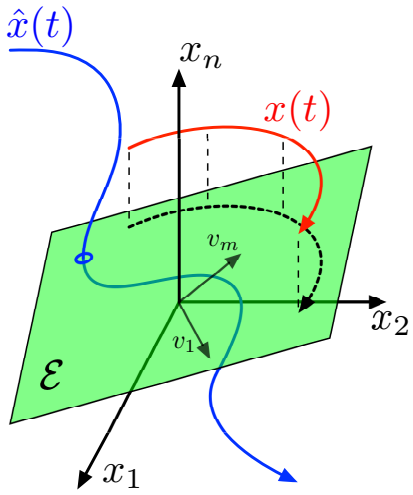

Figure 1.1: Model reduction by projection of a full trajectory $\mathbf{x}(t)$ on a linear subspace $\mathcal{E}$ of dimension m, spanned by the linear eigenvectors $\mathbf{v}_1, \ldots, \mathbf{v}_m$, at the origin. A general trajectory, starting from a point $\hat{\mathbf{x}}(0) \notin \mathcal{E}$ might enter $\mathcal{E}$ but also leave it again.

ant manifold tangent to a two-dimensional modal subspace of the linearized system. In a conservative autonomous setting, the two proposed views on NNMs is unified by the Lyapunov subcenter-manifold theorem [3], proving that, under appropriate non-resonance conditions, the Shaw and Pierre type of invariant manifolds will be filled with the Rosenberg type of periodic orbits.

For non-conservative systems, however, such a clear relationship doesn't hold anymore, as periodic orbits can become isolated in the phase space. Additionally, it is a priori unclear if either none or infinitely many such invariant manifolds tangent to an eigenspace may exist. Haller and Ponsioen [4] came up with a unified mathematical approach to nonlinear normal modes in non-conservative systems, where they define a nonlinear normal mode as a recurrent motion with finitely many frequencies. Included in their theory is a trivial NNM (or fixed point), a periodic NNM and a quasi-periodic NNM, where the frequencies are rationally incommensurate, with the orbit filling an invariant torus.

Using this NNM definition, Haller and Ponsioen [4] define a spectral submanifold (SSM) as the smoothest invariant manifold tangent to a modal subspace of an NNM. They then invoke rigorous existence, uniqueness and persistence results for autonomous and non-autonomous SSMs, providing an exact mathematical foundation for constructing nonlinear reduced-order models over appropriately chosen spectral subspaces. These models are obtained by reducing the full dynamics to the

exactly invariant SSM surfaces, tangent to those subspaces.

The SSM reduced-order models are defined on invariant sets of the full nonlinear system. Additionally, the reduced models are robust and therefore persist under small perturbations. The SSM-reduced-order models constructed over the slowest spectral subspaces are normally-hyperbolic attracting invariant manifolds [5], and therefore will attract typical trajectories making the reduced model relevant.

1.2 Summary of the results and thesis organization

In this thesis, we develop the the tools to construct exact reduced-order models for nonlinear mechanical systems using SSM theory. The underlying SSM theory used in all chapters is based on the following publication:

- G. Haller and S. Ponsioen. Nonlinear normal modes and spectral submanifolds: existence, uniqueness and use in model reduction. *Nonlinear dynamics* 86.3: 1493-1534, 2016. [4]

The following chapters are a collection of the author's results that are either published, submitted or to be submitted as research articles. Therefore, each chapter will be self contained, starting with an introduction, followed by the problem formulation, results and conclusions. The theories and methods are applied to problems varying from academic examples to models obtained using finite elements.

The work presented in chapter 2 is based on

- S. Ponsioen, T. Pedergnana and G. Haller. Automated computation of autonomous spectral submanifolds for nonlinear modal analysis. *Journal of Sound and Vibration*, 420, 269-295, 2018 [6],

where we discuss an automated computational methodology for computing two-dimensional SSMs in autonomous nonlinear mechanical systems. The SSMs are constructed up to arbitrary orders of accuracy, using the parameterization method. We developed an automated a posteriori error estimation feature that enables a systematic increase in the orders of the SSM computation until the required accuracy is reached. We find that the present algorithm provides a major speed-up, relative to numerical continuation methods, in the computation of backbone curves, especially in higher-dimensional problems. We illustrate the accuracy and speed of the automated SSM algorithm on lower- and higher-dimensional mechanical systems.

Chapter 3 is based on

- S. Ponsioen and G. Haller. Exact model reduction and fast forced response calculation in high-dimensional nonlinear mechanical systems. *submitted*, 2019 [7],

where we extended the work presented in chapter 2 to the non-autonomous setting. We used the reduced dynamics on a two-dimensional SSM to extract the forced-response curve around a particular mode of interest. The automated computation of non-autonomous SSMs can additionally be seen as a generalization of Breunung and Haller [8], which compute the non-autonomous part of the SSM up to zeroth order in the parameterization coordinates.

Chapter 4 is based on

- S. Ponsioen, T. Pedergnana and G. Haller. Analytic Prediction of Isolated Forced Response Curves from Spectral Submanifolds. *Nonlinear Dynamics*, 2019 [9],

were we show how SSM theory, in combination with the computational engine developed in chapter 3, can be used to provide analytic predictions for the response of periodically forced multi-degree-of-freedom mechanical systems. These predictions include an explicit criterion for the existence of isolated forced responses that will generally be missed by numerical continuation techniques. The analytic predictions can be refined to arbitrary precision via an algorithm that does not require the numerical solutions of the mechanical system. We illustrate all these results on low- and high-dimensional nonlinear vibration problems. We find that our SSM-based forced-response predictions remain accurate in high-dimensional systems, in which numerical continuation of the periodic response, using a collocation method, is no longer feasible.

As a byproduct of this thesis, we created a MATLAB based computational tool called SSMtool for computing two-dimensional spectral submanifolds in nonlinear mechanical systems with arbitrary degrees of freedom. SSMtool is intended for researchers and students who are interested in extracting key-information, such as reduced-order models, backbone curves or forced-response curves from a nonlinear, dissipative mechanical system with a potentially large number of degrees of freedom. The software achieves this without using any numerical integration or numerical continuation techniques, purely based on a reduction to SSMs. SSMtool can be downloaded from the Haller Group software page at the ETH Zürich:

`http://www.georgehaller.com`

SSMtool requires MATLAB R2016b or newer.

An additional effort was made in applying SSM theory directly on the second-order equations of motion, constructing explicit third-order reduced models for general nonlinear mechanical systems, and can be found in

- Z. Veraszto, S. Ponsioen and G. Haller. Explicit third-order model reduction formulas for general nonlinear mechanical systems. *Journal of Sound and Vibration*, 2020 [10].

This work has not been included in the thesis but is listed here for completeness.

Chapter 2

Autonomous SSMs

Chapter Summary

We discuss an automated computational methodology for computing two-dimensional spectral submanifolds (SSMs) in autonomous nonlinear mechanical systems of arbitrary degrees of freedom. In our algorithm, SSMs, the smoothest nonlinear continuations of modal subspaces of the linearized system, are constructed up to arbitrary orders of accuracy, using the parameterization method. An advantage of this approach is that the construction of the SSMs does not break down when the SSM folds over its underlying spectral subspace. A further advantage is an automated a posteriori error estimation feature that enables a systematic increase in the orders of the SSM computation until the required accuracy is reached. We find that the present algorithm provides a major speed-up, relative to numerical continuation methods, in the computation of backbone curves, especially in higher-dimensional problems. We illustrate the accuracy and speed of the automated SSM algorithm on lower- and higher-dimensional mechanical systems.

2.1 Introduction

A fundamental notion in decomposing nonlinear mechanical oscillations, is the *nonlinear normal mode* (NNM) concept of Rosenberg [1], who defined a nonlinear normal mode as a synchronous periodic oscillation that reaches its maximum in all modal coordinates at the same time. An alternative definition of a NNM, proposed by Shaw and Pierre [2], is an invariant manifold that serves as the nonlinear continuation of two-dimensional subspaces formed by normal modes of the linearized system. Shaw and Pierre seek such invariant manifolds as graphs over those two-dimensional subspaces. For several extensive discussions about these two NNM definitions, we refer the reader to the work of Kerschen et al. [11], Peeters et al. [12], Mikhlin and Avramov [13] and Vakakis et al. [14].

If one relaxes the synchronicity requirement of Rosenberg, a clear relationship between the above two views on NNMs emerges for conservative oscillatory systems by the Lyapunov subcenter-manifold theorem [3, 15]. Indeed, under appropriate non-

resonance conditions, these references guarantee the existence of a unique, analytic and robust Shaw—Pierre-type invariant manifold tangent to each two-dimensional modal subspace of the linearized system. This manifold, in turn, is filled with Rosenberg-type periodic orbits.

In a non-conservative setting, this geometrical relationship between the two classic NNM concepts no longer holds, as periodic orbits become rare and isolated in the phase space, whereas infinitely many invariant manifolds tangent to each two-dimensional modal subspace will exist. A unified approach has been proposed by Haller and Ponsioen [4] to clarify the relationship between the Rosenberg and Shaw—Pierre NNM concepts. Specifically, [4] defines a nonlinear normal mode simply as a recurrent motion with finitely many frequencies. Included in this theory is a trivial NNM or fixed point (no frequencies), a periodic NNM (the frequencies are rationally commensurate, as for a Rosenberg-type periodic orbit) and a quasiperiodic NNM (the frequencies are rationally incommensurate, with the orbit filling an invariant torus).

Using this NNM definition, Haller and Ponsioen [4] define a spectral submanifold (SSM) as the smoothest invariant manifold tangent to a modal subspace of a NNM. They then invoke rigorous existence, uniqueness and persistence results for autonomous and non-autonomous SSMs, providing an exact mathematical foundation for constructing nonlinear reduced-order models over appropriately chosen spectral subspaces. These models are obtained by reducing the full dynamics to the exactly invariant SSM surfaces, tangent to those subspaces.

More recently, Szalai et al. [16] have shown that the dynamics on a single-mode SSM can be seen as a nonlinear extension of the linear dynamics of the underlying modal subspace, making it possible to extract the *backbone curve*, defined as a graph plotting the instantaneous amplitude of vibration as a function of the instantaneous frequency of vibration. This approach to backbone-curve computations assumes that the Lyapunov subcenter-manifold perturbs smoothly to a unique SSM under appropriate non-resonance conditions and under small enough damping, which is consistent with the numerical observations as shown by Kerschen et al. [17], Peeters et al. [18] and Szalai et al. [16].

Computing invariant manifolds tangent to modal subspaces in realistic applications has been a challenge. Prior approaches have mostly focussed on solving the invariance equations that such manifolds have to satisfy (Blanc et al. [19], Pesheck et al. [20] and Renson et al. [21]). These invariance equations have infinitely many solutions, out of which the numerical approaches employed by different authors selected one particular solution. In contrast, the SSM theory employed here guarantees a unique solution that can be approximated with arbitrary high precision via the parameterization method of Cabré et al. [22, 23, 24]. In the present work, we describe an automated computational algorithm for two-dimensional SSMs constructed over

two-dimensional modal subspaces. This algorithm[1] allows us to compute the SSMs, their reduced dynamics and associated backbone curves to arbitrary orders of accuracy, limited only by available memory. An important feature of the algorithm is a direct a posteriori estimation of the error in computing the SSM at a given approximation order. This error estimate measures directly the extend to which the SSM is invariant. If the error is unsatisfactory, the user can select higher order approximations until the error falls below a required bound.

In technical terms, we construct the SSMs as embeddings of the modal subspaces into the phase space of the mechanical system, as required by the parameterization method (Cabré et al. [22, 23, 24]). A major advantage compared to most earlier calculations (Haller and Ponsioen [4]) is that the parameterized construction of SSMs does not break down when the SSM folds over the underlying modal subspace. Another advantage of the method is its suitability for algorithmic implementations for arbitrary orders of accuracy in arbitrary dimensions. For applications of the parameterization method to other types of dynamical systems, we refer the reader to the work of Haro et al. [25], van den Berg and Mireles James [26] and Mireles James [27].

[1] SSMtool is available at: www.georgehaller.com

2.2 System set-up

We consider n-degree-of-freedom, autonomous mechanical systems of the form

$$\mathbf{M}\ddot{\mathbf{y}} + \mathbf{C}\dot{\mathbf{y}} + \mathbf{K}\mathbf{y} + \mathbf{f}(\mathbf{y}, \dot{\mathbf{y}}) = \mathbf{0}, \qquad \mathbf{f}(\mathbf{y}, \dot{\mathbf{y}}) = \mathcal{O}\left(|\mathbf{y}|^2, |\mathbf{y}|\,|\dot{\mathbf{y}}|, |\dot{\mathbf{y}}|^2\right), \tag{2.1}$$

where $\mathbf{y} \in \mathbb{R}^n$ is the generalized position vector; $\mathbf{M} = \mathbf{M}^T \in \mathbb{R}^{n\times n}$ is the positive definite mass matrix; $\mathbf{C} = \mathbf{C}^T \in \mathbb{R}^{n\times n}$ is the damping matrix; $\mathbf{K} = \mathbf{K}^T \in \mathbb{R}^{n\times n}$ is the stiffness matrix and $\mathbf{f}(\mathbf{x}, \dot{\mathbf{x}})$ denotes all the nonlinear terms in the system. These nonlinearities are assumed to be of class C^r in $(\mathbf{x}, \dot{\mathbf{x}})$, with $r \in \mathbb{N}^+ \cup \{\infty, a\}$. Here $r \in \mathbb{N}^+$ refers to finite differentiability, $r = \infty$ refers to infinite differentiability, and $r = a$ refer to analyticity, all three of which are allowed in our treatment.

System (2.1) can be transformed into a set of $2n$ first-order ordinary differential equations by introducing a change of variables $\mathbf{x}_1 = \mathbf{y}$, $\mathbf{x}_2 = \dot{\mathbf{y}}$, with $\mathbf{x} = (\mathbf{x}_1, \mathbf{x}_2) \in \mathbb{R}^{2n}$, which gives,

$$\dot{\mathbf{x}} = \begin{pmatrix} \mathbf{0} & \mathbf{I} \\ -\mathbf{M}^{-1}\mathbf{K} & -\mathbf{M}^{-1}\mathbf{C} \end{pmatrix} \mathbf{x} + \begin{pmatrix} \mathbf{0} \\ -\mathbf{M}^{-1}\mathbf{f}(\mathbf{x}_1, \mathbf{x}_2) \end{pmatrix} = \mathbf{A}\mathbf{x} + \mathbf{F}(\mathbf{x}), \tag{2.2}$$
$$\mathbf{x} \in \mathbb{R}^{2n}, \qquad \mathbf{F}(\mathbf{x}) = \mathcal{O}\left(|\mathbf{x}|^2\right).$$

The transformed system (2.2) has a fixed point at $\mathbf{x} = \mathbf{0}$, $\mathbf{A} \in \mathbb{R}^{2n\times 2n}$ is a constant matrix and $\mathbf{F}(\mathbf{x})$ is a class C^r function containing all the nonlinearities. Note that the inverse of the mass matrix is well-defined because $\mathbf{M}$ is assumed positive definite.

The linearized part of (2.2) is

$$\dot{\mathbf{x}} = \mathbf{A}\mathbf{x}, \tag{2.3}$$

where the matrix $\mathbf{A}$ has $2n$ eigenvalues $\lambda_k \in \mathbb{C}$ for $k = 1, \ldots, 2n$. Counting multiplicities, we sort these eigenvalues based on their real parts in the decreasing order,

$$\mathrm{Re}(\lambda_{2n}) \leq \mathrm{Re}(\lambda_{2n-1}) \leq \ldots \leq \mathrm{Re}(\lambda_1) < 0, \tag{2.4}$$

assuming that the real part of each eigenvalue is less than zero and hence the fixed point is asymptotically stable. We further assume that the constant matrix $\mathbf{A}$ is semisimple, which implies that the algebraic multiplicity of each λ_k is equal to its geometric multiplicity, i.e. $\mathrm{alg}(\lambda_k) = \mathrm{geo}(\lambda_k)$. We can therefore identify $2n$ linearly independent eigenvectors $\mathbf{v}_k \in \mathbb{C}^{2n}$, with $k = 1, \ldots, 2n$, each spanning a real eigenspace $E_k \subset \mathbb{R}^{2n}$ with $\dim(E_k) = 2 \times \mathrm{alg}(\lambda_k)$ in case $\mathrm{Im}(\lambda_k) \neq 0$, or $\dim(E_k) = \mathrm{alg}(\lambda_k)$ in case $\mathrm{Im}(\lambda_k) = 0$.

2.3 Autonomous SSMs for continuous mechanical systems

As $\mathbf{A}$ is semisimple, the linear part of system (4.2) can be diagonalized by introducing a linear change of coordinates $\mathbf{x} = \mathbf{T}\mathbf{q}$, with $\mathbf{T} = [\mathbf{v}_{j_1}, \mathbf{v}_{j_2}, \ldots, \mathbf{v}_{j_{2n}}] \in \mathbb{C}^{2n\times 2n}$ and $\mathbf{q} \in \mathbb{C}^{2n}$,

$$\begin{aligned}\dot{\mathbf{q}} = \mathbf{T}^{-1}\mathbf{A}\mathbf{T}\mathbf{q} + \mathbf{T}^{-1}\mathbf{F}(\mathbf{T}\mathbf{q}) &= \underbrace{\operatorname{diag}(\lambda_{j_1}, \lambda_{j_2} \ldots, \lambda_{j_{2n}})}_{\mathbf{\Lambda}}\mathbf{q} + \underbrace{\mathbf{T}^{-1}\mathbf{F}(\mathbf{T}\mathbf{q})}_{\mathbf{G}(\mathbf{q})} \\ &= \mathbf{\Lambda}\mathbf{q} + \mathbf{G}(\mathbf{q}).\end{aligned} \tag{2.5}$$

We now seek a two-dimensional modal subspace $\mathcal{E} = \operatorname{span}\{\mathbf{v}_{j_1}, \mathbf{v}_{j_2}\} \subset \mathbb{C}^{2n}$, with $\mathbf{v}_{j_2} = \bar{\mathbf{v}}_{j_1}$. Note that $\mathbf{v}_{j_1}$ and $\mathbf{v}_{j_2}$ are purely real if $\lambda_{j_1}, \lambda_{j_2} \in \mathbb{R}$, in which case $\mathcal{E}$ corresponds to either a single critically damped mode ($\lambda_{j_1} = \lambda_{j_2}$), or to two overdamped modes ($\lambda_{j_1} \neq \lambda_{j_2}$). In contrast, if $\lambda_{j_1}, \bar{\lambda}_{j_2} \in \mathbb{C}$ with $\operatorname{Im}\lambda_{j_1} \neq 0$, then $\mathcal{E}$ corresponds to a single underdamped mode.

The remaining linearly independent eigenvectors $\mathbf{v}_{j_3}, \ldots, \mathbf{v}_{j_{2n}}$ span a complex subspace $\mathcal{C} \subset \mathbb{C}^{2n}$ such that the full phase space of (2.5) can be expressed as the direct sum

$$\mathbb{C}^{2n} = \mathcal{E} \oplus \mathcal{C}. \tag{2.6}$$

The diagonal matrix $\mathbf{\Lambda}$ is the representation of the linear matrix $\mathbf{A}$ with respect to this decomposition, which we can also write as

$$\mathbf{\Lambda} = \begin{bmatrix} \mathbf{\Lambda}_{\mathcal{E}} & 0 \\ 0 & \mathbf{\Lambda}_{\mathcal{C}} \end{bmatrix}, \quad \operatorname{Spect}(\mathbf{\Lambda}_{\mathcal{E}}) = \{\lambda_{j_1}, \lambda_{j_2}\}, \quad \operatorname{Spect}(\mathbf{\Lambda}_{\mathcal{C}}) = \{\lambda_{j_3}, \ldots, \lambda_{j_{2n}}\}, \tag{2.7}$$

with $\mathbf{\Lambda}_{\mathcal{E}} = \operatorname{diag}(\lambda_{j_1}, \lambda_{j_2})$ and $\mathbf{\Lambda}_{\mathcal{C}} = \operatorname{diag}(\lambda_{j_3}, \ldots, \lambda_{j_{2n}})$.

Following the work of Haller and Ponsioen [4], we now define a spectral submanifold of the nonlinear system (2.5) as an invariant manifold tangent to the spectral subspace $\mathcal{E}$.

Definition 2.1 *A spectral submanifold (SSM), $\mathcal{W}(\mathcal{E})$, corresponding to a spectral subspace $\mathcal{E}$ of $\mathbf{\Lambda}$ is an invariant manifold of the dynamical system (2.5) such that*

(i) *$\mathcal{W}(\mathcal{E})$ is tangent to $\mathcal{E}$ and has the same dimension as $\mathcal{E}$.*

(ii) *$\mathcal{W}(\mathcal{E})$ is strictly smoother than any other invariant manifold satisfying (i).*

We define the *outer spectral quotient* $\sigma_{\text{out}}(\mathcal{E})$ as the positive integer

$$\sigma_{\text{out}}(\mathcal{E}) = \text{Int}\left[\frac{\min_{\lambda\in\text{Spect}(\mathbf{\Lambda}_\mathcal{C})}\text{Re}\lambda}{\max_{\lambda\in\text{Spect}(\mathbf{\Lambda}_\mathcal{E})}\text{Re}\lambda}\right] \in \mathbb{N}^+. \tag{2.8}$$

Which is the integer part of the ratio between the strongest decay rate of the linearized oscillations outside $\mathcal{E}$ and the weakest decay rate of the linearized oscillations inside $\mathcal{E}$. As we will see shortly, $\sigma_{\text{out}}(\mathcal{E})$ determines the smoothness class in which $\mathcal{W}(\mathcal{E})$ turns out to be unique.

To state the main results on SSMs from Haller and Ponsioen [4], we need the following two assumptions:

(A1) $\sigma_{\text{out}}(\mathcal{E}) \leq r$,

(A2) The *outer* non-resonance conditions

$$a\lambda_{j_1} + b\lambda_{j_2} \neq \lambda_l, \quad \forall\lambda_l \in \text{Spect}(\mathbf{\Lambda}_\mathcal{C}). \tag{2.9}$$

hold for all positive integers a and b satisfying $2 \leq a + b \leq \sigma_{\text{out}}(\mathcal{E})$.

Under these assumptions, we have the following main result on an SSM tangent to the modal subspace $\mathcal{E}$ in system (2.5).

Theorem 1

(i) There exist a two-dimensional SSM, $\mathcal{W}(\mathcal{E})$, that is tangent to the spectral subspace $\mathcal{E}$ at the fixed point $\mathbf{q} = \mathbf{0}$.

(ii) $\mathcal{W}(\mathcal{E})$ is of class C^r and is unique among all class $C^{\sigma_{\text{out}}(\mathcal{E})+1}$ two-dimensional invariant manifolds that are tangent to $\mathcal{E}$ at $\mathbf{q} = \mathbf{0}$.

(iii) $\mathcal{W}(\mathcal{E})$ can be parameterized over an open set $\mathcal{U} \subset \mathbb{C}^2$ via the map

$$\mathbf{W} : \mathcal{U} \subset \mathbb{C}^2 \to \mathbb{C}^{2n}, \tag{2.10}$$

into the phase space of system (2.5).

(iv) There exist a C^r polynomial function $\mathbf{R} : \mathcal{U} \to \mathcal{U}$ satisfying the following invariance relationship

$$\mathbf{\Lambda W} + \mathbf{G} \circ \mathbf{W} = \nabla\mathbf{W}\mathbf{R}, \tag{2.11}$$

such that the reduced dynamics on the SSM can be expressed as

$$\dot{\mathbf{z}} = \mathbf{R}(\mathbf{z}), \quad \mathbf{R}(\mathbf{0}) = \mathbf{0}, \quad \nabla\mathbf{R}(\mathbf{0}) = \mathbf{\Lambda}_{\mathcal{E}} = \begin{bmatrix} \lambda_{j_1} & 0 \\ 0 & \lambda_{j_2} \end{bmatrix}, \qquad (2.12)$$
$$\mathbf{z} = (z_{j_1}, z_{j_2}) \in \mathcal{U}.$$

(v) If the *inner* non-resonance conditions

$$a\lambda_{j_1} + b\lambda_{j_2} \neq \lambda_{j_i}, \quad i = 1, 2 \qquad (2.13)$$

hold for all positive integers a and b with

$$2 \leq a + b \leq \sigma_{\text{in}}(\mathcal{E}) = \text{Int}\left[\frac{\min_{\lambda \in \text{Spect}(\mathbf{\Lambda}_{\mathcal{E}})} \text{Re}\lambda}{\max_{\lambda \in \text{Spect}(\mathbf{\Lambda}_{\mathcal{E}})} \text{Re}\lambda}\right] \in \mathbb{N}^+,$$

then the mapping $\mathbf{W}$ can be chosen in such a way that $\mathbf{R}(\mathbf{z})$ does not contain the terms $z_{j_1}^a z_{j_2}^b$. In particular, if no inner resonances arise, then the reduced dynamics on the SSM can be linearized.

The proof of Theorem 1 can be found in the work of Haller and Ponsioen [4], which is based on the more abstract results of Cabré et al. [22, 23, 24] for mappings on Banach spaces.

2.4 Autonomous SSM computation

In this section we show how the parameterized spectral submanifolds are approximated, around a fixed point, using polynomials. We express $\mathbf{W}(\mathbf{z})$, $\mathbf{R}(\mathbf{z})$ and $\mathbf{G}(\mathbf{q})$ as multivariate polynomial functions, which is done by using the Kronecker product. Substituting the expressions in the invariance equation (2.11), we obtain, for each order, a linear system of equations that can be solved under appropriate non-resonance conditions. For a different application of the parameterization method, we refer to the work of Mireles James [27]. Where the parameterization method is used for approximating (un)stable manifolds of one parameter families of analytic dynamical systems, by using polynomials. For a more elaborate discussion about the numerical computation of the coefficients of higher order power series expansions of parameterized invariant manifolds around a fixed point of an elementary vector field, where the coefficients of the power series expansions are obtained using methods of Automatic Differentiation, we refer to Haro et al. [25].

2.4.1 The Kronecker product

We now describe a computational algorithm for constructing the mapping $\mathbf{W}(\mathbf{z})$ in (2.10) that maps $\mathcal{U} \subset \mathbb{C}^2$ into the phase space of system (4.2), and the reduced dynamics $\mathbf{R}(\mathbf{z})$ in (2.12). To handle the polynomial calculations arising in the algorithm efficiently, we first need to recall the notion and some properties of the Kronecker product [28].

Definition 2.2 *Let* $\mathbf{A} \in \mathbb{C}^{m\times n}$, $\mathbf{B} \in \mathbb{C}^{p\times q}$. *Then we define the Kronecker product of* $\mathbf{A}$ *and* $\mathbf{B}$ *as*

$$\mathbf{A} \otimes \mathbf{B} = \begin{bmatrix} a_{11}\mathbf{B} & \cdots & a_{1n}\mathbf{B} \\ \vdots & \ddots & \vdots \\ a_{m1}\mathbf{B} & \cdots & a_{mn}\mathbf{B} \end{bmatrix} \in \mathbb{C}^{mp\times nq}. \tag{2.14}$$

In accordance with Definition 2.2, the Kronecker product of two vectors $\mathbf{x} \in \mathbb{C}^m$ and $\mathbf{y} \in \mathbb{C}^n$ is given by the vector

$$\mathbf{x} \otimes \mathbf{y} = \begin{bmatrix} x_1\mathbf{y} \\ \vdots \\ x_m\mathbf{y} \end{bmatrix} = [x_1y_1 \cdots x_1y_n \cdots x_my_1 \cdots x_my_n]^T \in \mathbb{C}^{mn}, \tag{2.15}$$

or equivalently, written in index notation,

$$\mathbf{x} \otimes \mathbf{y} = \sum_{i=1}^{m}\sum_{j=1}^{n} x_iy_j\mathbf{e}_i^x \otimes \mathbf{e}_j^y, \tag{2.16}$$

where $\mathbf{e}_i^x \in \mathbb{C}^m$ and $\mathbf{e}_j^y \in \mathbb{C}^n$ are basis vectors containing a one in their i^{th} and j^{th} entries, respectively, and zeros elsewhere. Differentiating equation (2.16) with respect to time yields

$$\frac{d}{dt}(\mathbf{x} \otimes \mathbf{y}) = \frac{d}{dt}\left(x_iy_j\mathbf{e}_i^x \otimes \mathbf{e}_j^y\right) = \dot{x}_iy_j\mathbf{e}_i^x \otimes \mathbf{e}_j^y + x_i\dot{y}_j\mathbf{e}_i^x \otimes \mathbf{e}_j^y = \dot{\mathbf{x}} \otimes \mathbf{y} + \mathbf{x} \otimes \dot{\mathbf{y}}. \tag{2.17}$$

which is simply the product rule. By using the same reasoning, one shows that the product rule also applies to the time derivative of the Kronecker product of multiple vectors. We will use the shorthand notation $\mathbf{z}^{\otimes i}$ defined as

$$\mathbf{z}^{\otimes i} = \begin{cases} \mathbf{z} & \text{for } i = 1. \\ \underbrace{\mathbf{z} \otimes \mathbf{z} \otimes \cdots \otimes \mathbf{z}}_{i \text{ times}} & \text{for } i > 1. \end{cases} \tag{2.18}$$

For subsequent derivations, we will make use of several properties of the Kronecker product, which we list in 2.A for convenience.

We Taylor expand $\mathbf{W}(\mathbf{z})$ and $\mathbf{R}(\mathbf{z})$ and express them as multivariate polynomial functions

$$\mathbf{W}(\mathbf{z}) = \sum_{i=1}^{n_w} \mathbf{W}_i \mathbf{z}^{\otimes i} = \mathbf{W}_1\mathbf{z} + \mathbf{W}_2\mathbf{z}\otimes\mathbf{z} + \mathbf{W}_3\mathbf{z}\otimes\mathbf{z}\otimes\mathbf{z} + \dots, \tag{2.19}$$
$$\mathbf{W}_i \in \mathbb{C}^{2n\times 2^i}, \quad \mathbf{z}\in\mathbb{C}^2,$$

$$\mathbf{R}(\mathbf{z}) = \sum_{i=1}^{n_w} \mathbf{R}_i \mathbf{z}^{\otimes i} = \mathbf{R}_1\mathbf{z} + \mathbf{R}_2\mathbf{z}\otimes\mathbf{z} + \mathbf{R}_3\mathbf{z}\otimes\mathbf{z}\otimes\mathbf{z} + \dots, \tag{2.20}$$
$$\mathbf{R}_i \in \mathbb{C}^{2\times 2^i}, \quad \mathbf{z}\in\mathbb{C}^2,$$

with $n_w \geq \sigma_{\text{out}}(\mathcal{E}) + 1$ denoting the order of the SSM expansion. We also Taylor expand the nonlinear part of our dynamical system (2.5) up to order n_w, around the fixed point $\mathbf{q} = \mathbf{0}$, such that we can represent the nonlinearities, in a fashion similar to equations (2.19) and (2.20), as

$$\mathbf{G}(\mathbf{q}) = \sum_{i=2}^{\Gamma} \mathbf{G}_i \mathbf{q}^{\otimes i} = \mathbf{G}_2\mathbf{q}\otimes\mathbf{q} + \mathbf{G}_3\mathbf{q}\otimes\mathbf{q}\otimes\mathbf{q} + \dots, \tag{2.21}$$
$$\mathbf{G}_i \in \mathbb{C}^{2n\times(2n)^i}, \quad \mathbf{q}\in\mathbb{C}^{2n},$$

with Γ denoting the maximum order of nonlinearity considered.

By construction, the vector $\mathbf{q}^{\otimes i}$ will have redundant terms along its elements, and hence $\mathbf{G}_i$ will have infinitely many possible representations at the i^{th} order in equation (2.5). The redundancy in $\mathbf{q}^{\otimes i}$ allows us to introduce constraints between the different coefficients that are related to the same monomial term. We can always set these constraints such that $\mathbf{G}(\mathbf{q})$ will represent the $2n$-dimensional polynomial vector $\mathbf{T}^{-1}\mathbf{F}(\mathbf{T}\mathbf{q})$. For more detail, we refer the reader to 2.C.

2.4.2 The coefficient equations

We recall here the diagonalized dynamical system (2.5)

$$\dot{\mathbf{q}} = \mathbf{\Lambda}\mathbf{q} + \mathbf{G}(\mathbf{q}). \tag{2.22}$$

Substituting $\mathbf{q} = \mathbf{W}(\mathbf{z})$ on the right-hand side of equation (2.22), then differentiating $\mathbf{q} = \mathbf{W}(\mathbf{z})$ with respect to time and substituting the result $\dot{\mathbf{q}} = \nabla\mathbf{W}(\mathbf{z})\dot{\mathbf{z}}$ on

the left-hand side of equation (2.22), we obtain the invariance relation (2.11) in the form

$$\begin{aligned}
&\mathbf{W}_1\mathbf{R}(\mathbf{z}) + \mathbf{W}_2\left(\mathbf{R}(\mathbf{z})\otimes\mathbf{z} + \mathbf{z}\otimes\mathbf{R}(\mathbf{z})\right)\\
&+ \mathbf{W}_3\left(\mathbf{R}(\mathbf{z})\otimes\mathbf{z}\otimes\mathbf{z} + \mathbf{z}\otimes\mathbf{R}(\mathbf{z})\otimes\mathbf{z} + \mathbf{z}\otimes\mathbf{z}\otimes\mathbf{R}(\mathbf{z})\right) + \ldots\\
&+ \mathbf{W}_k\left(\mathbf{R}(\mathbf{z})\otimes\mathbf{z}^{\otimes k-1} + \Sigma_{j=1}^{k-2}\left(\mathbf{z}^{\otimes j}\otimes\mathbf{R}(\mathbf{z})\otimes\mathbf{z}^{\otimes k-j-1}\right) + \mathbf{z}^{\otimes k-1}\otimes\mathbf{R}(\mathbf{z})\right)\\
&= \mathbf{\Lambda}\mathbf{W}(\mathbf{z}) + \mathbf{G}_2\mathbf{W}(\mathbf{z})^{\otimes 2} + \ldots + \mathbf{G}_\Gamma\mathbf{W}(\mathbf{z})^{\otimes\Gamma},
\end{aligned} \tag{2.23}$$

for $k = \{2,\ldots,n_w\}$. The time derivative of $\mathbf{q} = \mathbf{W}(\mathbf{z}) = \sum_i \mathbf{W}_i\mathbf{z}^{\otimes i}$ can be expressed, using the product rule for the Kronecker product of vectors, as

$$\begin{aligned}
\dot{\mathbf{q}} = \mathbf{W}_1\dot{\mathbf{z}} + \mathbf{W}_2\left(\dot{\mathbf{z}}\otimes\mathbf{z} + \mathbf{z}\otimes\dot{\mathbf{z}}\right)\\
+ \mathbf{W}_3\left(\dot{\mathbf{z}}\otimes\mathbf{z}\otimes\mathbf{z} + \mathbf{z}\otimes\dot{\mathbf{z}}\otimes\mathbf{z} + \mathbf{z}\otimes\mathbf{z}\otimes\dot{\mathbf{z}}\right) + \ldots.
\end{aligned} \tag{2.24}$$

Substituting $\dot{\mathbf{z}} = \mathbf{R}(\mathbf{z})$ into (2.24), we precisely obtain the left-hand side of equation (2.23). Rewriting equation (2.23) and collecting terms of equal power $\mathbf{z}^{\otimes i}$ for $i = \{1,\ldots n_w\}$, we obtain, for $i = 1$,

$$\underbrace{\begin{bmatrix}\mathbf{\Lambda}_{\mathcal{E}} & \mathbf{0}\\ \mathbf{0} & \mathbf{\Lambda}_{\mathcal{C}}\end{bmatrix}}_{\mathbf{\Lambda}}\mathbf{W}_1 = \mathbf{W}_1\mathbf{R}_1. \tag{2.25}$$

From (2.12), we then require that $\nabla\mathbf{R}(\mathbf{0}) = \mathbf{\Lambda}_{\mathcal{E}} = \mathbf{R}_1$. Therefore, equation (2.25) will be satisfied if we set $\mathbf{W}_1 \in \mathcal{C}^{2n\times 2}$ equal to

$$\mathbf{W}_1 = \begin{bmatrix}1 & 0\\ 0 & 1\\ 0 & 0\\ \vdots & \vdots\\ 0 & 0\end{bmatrix}. \tag{2.26}$$

For $2 \leq i \leq n_w$ we have

$$\mathbf{\Lambda}\mathbf{W}_i - \mathbf{W}_i \overbrace{\sum_{|\mathbf{s}|=1} \mathbf{\Lambda}_{\mathcal{E}}^{s_1} \otimes \cdots \otimes \mathbf{\Lambda}_{\mathcal{E}}^{s_i}}^{\tilde{\mathbf{\Lambda}}_{\mathcal{E},i}} = \mathbf{W}_1\mathbf{R}_i \tag{2.27}$$
$$+ \sum_{m=2}^{i-1} \mathbf{W}_m \sum_{|\mathbf{p}|=1} \mathbf{R}_{i+1-m}^{p_1} \otimes \ldots \otimes \mathbf{R}_{i+1-m}^{p_m} - \mathbf{G}_i\mathbf{W}_1^{\otimes i}$$
$$- \sum_{m=2}^{i-1} \mathbf{G}_m \sum_{|\mathbf{r}|=i} \mathbf{W}_{r_1} \otimes \ldots \otimes \mathbf{W}_{r_m},$$

where we make use of multi-index notation for $\mathbf{s} = \{s_1, \ldots, s_i\} \in \mathbb{N}^i$, $\mathbf{p} = \{p_1, \ldots, p_m\} \in \mathbb{N}^m$ and $\mathbf{r} = \{r_1, \ldots, r_m\} \in \mathbb{N}^m$. The notation $\mathbf{\Lambda}_{\mathcal{E}}^{s_j}$ is used to indicate that the matrix $\mathbf{\Lambda}_{\mathcal{E}}$ is taken to the power $s_j \in \mathbb{N}$, where the zeroth power will simply return the identity matrix of the same dimension as $\mathbf{\Lambda}_{\mathcal{E}}$. Note that we also adopt the same notation for $\mathbf{R}_{i+1-m} \in \mathbb{C}^{2\times 2^{i+1-m}}$, where we set $\mathbf{R}_{i+1-m}^0 \triangleq \mathbf{I} \in \mathbb{R}^{2\times 2}$.

The right hand side of equation (2.27) consists of the lower-order terms $\mathbf{W}_j$ for $2 \leq j < i-1$, which are known for the current order i. The term $\mathbf{R}_i$ represents the coefficient matrix corresponding to the i^{th}-order of the polynomial $\mathbf{R}(\mathbf{z})$. This polynomial depends on the preferred style of parameterization and will be chosen to remove near-inner resonances from the SSM expressions, as explained later in section 2.5. The matrices $\mathbf{G}_j$, for $2 \leq j \leq i$, are known by definition because they represent the nonlinearities of system (4.5).

Partitioning the coefficient equations

Due to the diagonal structure of $\mathbf{\Lambda}$, we can partition equation (2.27) into the two separate matrix equations

$$\mathbf{\Lambda}_{\mathcal{E}}\mathbf{W}_i^{\mathcal{E}} - \mathbf{W}_i^{\mathcal{E}}\tilde{\mathbf{\Lambda}}_{\mathcal{E},i} = \mathbf{R}_i + \mathbf{B}_i^{\mathcal{E}}, \tag{2.28}$$
$$\mathbf{\Lambda}_{\mathcal{C}}\mathbf{W}_i^{\mathcal{C}} - \mathbf{W}_i^{\mathcal{C}}\tilde{\mathbf{\Lambda}}_{\mathcal{E},i} = \mathbf{B}_i^{\mathcal{C}}, \tag{2.29}$$

where $\mathbf{W}_i$ is partitioned as

$$\mathbf{W}_i = \begin{bmatrix} \mathbf{W}_i^{\mathcal{E}} \\ \mathbf{W}_i^{\mathcal{C}} \end{bmatrix} \in \mathbb{C}^{2n\times 2^i}, \quad \mathbf{W}_i^{\mathcal{E}} \in \mathbb{C}^{2\times 2^i}, \quad \mathbf{W}_i^{\mathcal{C}} \in \mathbb{C}^{(2n-2)\times 2^i}. \tag{2.30}$$

The matrices $\mathbf{B}_i^{\mathcal{E}} \in \mathcal{C}^{2\times 2^i}$ and $\mathbf{B}_i^{C} \in \mathcal{C}^{(2n-2)\times 2^i}$ are such that

$$\begin{bmatrix} \mathbf{B}_i^{\mathcal{E}} \\ \mathbf{B}_i^{\mathcal{C}} \end{bmatrix} = \sum_{m=2}^{i-1} \mathbf{W}_m \sum_{|\mathbf{p}|=1} \mathbf{R}_{i+1-m}^{p_1} \otimes \ldots \otimes \mathbf{R}_{i+1-m}^{p_m} - \mathbf{G}_i \mathbf{W}_1^{\otimes i} \\ - \sum_{m=2}^{i-1} \mathbf{G}_m \sum_{|\mathbf{r}|=i} \mathbf{W}_{r_1} \otimes \ldots \otimes \mathbf{W}_{r_m}. \tag{2.31}$$

Equations (2.28) and (2.29) are also known as the Sylvester equations [28], having the unknown coefficient matrices $\mathbf{W}_i^{\mathcal{E}}$ and $\mathbf{W}_i^{\mathcal{C}}$. Using the Kronecker product and the vectorization operation

$$\operatorname{vec}(\mathbf{A}) = \operatorname{vec}\left([\mathbf{a}_1 \mathbf{a}_2 \ldots \mathbf{a}_n]\right) = \begin{bmatrix} \mathbf{a}_1 \\ \vdots \\ \mathbf{a}_n \end{bmatrix} \in \mathbb{C}^{mn}, \quad \mathbf{A} \in \mathbb{C}^{m \times n}, \tag{2.32}$$

with $\mathbf{a}_1, \ldots, \mathbf{a}_n$ denoting the column vectors of $\mathbf{A}$, we rewrite equation (2.28) and equation (2.29) as

$$\underbrace{\left(\mathbf{I}_{2^i \times 2^i} \otimes \mathbf{\Lambda}_{\mathcal{E}} - \tilde{\mathbf{\Lambda}}_{\mathcal{E},i}^T \otimes \mathbf{I}_{2\times 2}\right)}_{\mathbf{\Theta}_i^{\mathcal{E}}} \operatorname{vec}\left(\mathbf{W}_i^{\mathcal{E}}\right) = \operatorname{vec}\left(\mathbf{R}_i\right) + \operatorname{vec}\left(\mathbf{B}_i^{\mathcal{E}}\right). \tag{2.33}$$

$$\underbrace{\left(\mathbf{I}_{2^i \times 2^i} \otimes \mathbf{\Lambda}_{\mathcal{C}} - \tilde{\mathbf{\Lambda}}_{\mathcal{E},i}^T \otimes \mathbf{I}_{(2n-2)\times(2n-2)}\right)}_{\mathbf{\Theta}_i^{\mathcal{C}}} \operatorname{vec}\left(\mathbf{W}_i^{\mathcal{C}}\right) = \operatorname{vec}\left(\mathbf{B}_i^{\mathcal{C}}\right). \tag{2.34}$$

Invertibility of $\mathbf{\Theta}_i^{\mathcal{E}}$ and $\mathbf{\Theta}_i^{\mathcal{C}}$

Finding a unique solution for $\mathbf{W}_i^{\mathcal{C}}$ in equation (2.34) for a nonzero right-hand side requires the matrix $\mathbf{\Theta}_i^{\mathcal{C}}$ to be non-singular. If, however, $\mathbf{\Theta}_i^{\mathcal{E}}$ is singular, which arises from exact inner resonances, it suffices for the vectorized solution for $\mathbf{W}_i^{\mathcal{E}}$ to be in the kernel of $\mathbf{\Theta}_i^{\mathcal{E}}$. We can ensure this by choosing $\operatorname{vec}\left(\mathbf{R}_i\right)$ such that the right-hand side of equation (2.33) is zero. To carry out all this, we need to find the eigenvalues of $\mathbf{\Theta}_i^{\mathcal{E}}$ and $\mathbf{\Theta}_i^{\mathcal{C}}$.

It can be shown [28] that for a matrix $\mathbf{A} \in \mathbb{C}^{n\times n}$, with the eigenvalues λ_i and a matrix $\mathbf{B} \in \mathbb{C}^{m\times m}$ with eigenvalues μ_j, the matrix $\mathbf{I}_{m\times m} \otimes \mathbf{A} - \mathbf{B} \otimes \mathbf{I}_{n\times n}$ has the mn eigenvalues

$$\lambda_1 - \mu_1, \ldots, \lambda_1 - \mu_m, \lambda_2 - \mu_1, \ldots, \lambda_2 - \mu_m, \ldots, \lambda_n - \mu_1, \ldots, \lambda_n - \mu_m. \tag{2.35}$$

In the current setting of (2.33) and (2.34), we know that the eigenvalues of $\mathbf{\Lambda}_{\mathcal{E}}$ and $\mathbf{\Lambda}_{\mathcal{C}}$ are $\lambda_{j_1}, \lambda_{j_2}$ and $\lambda_{j_3} \ldots, \lambda_{j_{2n}}$, respectively. By further exploiting the structure of

$$\begin{aligned}\tilde{\mathbf{\Lambda}}_{\mathcal{E},i}^{T} = \tilde{\mathbf{\Lambda}}_{\mathcal{E},i} &= \sum_{|\mathbf{s}|=1} \mathbf{\Lambda}_{\mathcal{E}}^{s_1} \otimes \cdots \otimes \mathbf{\Lambda}_{\mathcal{E}}^{s_i} \\ &= \mathbf{\Lambda}_{\mathcal{E}} \otimes \mathbf{I} \otimes \cdots \otimes \mathbf{I} + \ldots + \mathbf{I} \otimes \mathbf{I} \otimes \cdots \otimes \mathbf{\Lambda}_{\mathcal{E}},\end{aligned} \tag{2.36}$$

or, equivalently,

$$\tilde{\mathbf{\Lambda}}_{\mathcal{E},i} = \operatorname{diag}\left(a_1\lambda_1 + b_1\lambda_2, \ldots, a_{2^i}\lambda_1 + b_{2^i}\lambda_2\right) \in \mathbb{C}^{2^i \times 2^i}, \tag{2.37}$$

we observe that each diagonal term of the matrix $\tilde{\mathbf{\Lambda}}_{\mathcal{E}}$ for a given order i will consist of a linear combination of λ_1 and λ_2, i.e., $a_j\lambda_1 + b_j\lambda_2$ for $j = \left\{1, \ldots, 2^i\right\}$, with $a_j, b_j \in \mathbb{N}$. Now let $\mathbf{\Omega}_i$ be a 2^i-dimensional vector containing all possible lexicographically ordered i-tuples made out of elements of the set $\{1, 2\}$, in which repetition is allowed. The multiplicity corresponding to the numbers 1 and 2, in the j^{th} element of $\mathbf{\Omega}_i$, will represent a_j and b_j respectively. To illustrate this, we give an example

Example 2.3 [Constructing the matrix $\tilde{\mathbf{\Lambda}}_{\mathcal{E},2}$] For $i = 2$, the diagonal matrix $\tilde{\mathbf{\Lambda}}_{\mathcal{E},2}$ is equal to

$$\begin{aligned}\tilde{\mathbf{\Lambda}}_{\mathcal{E},2} = \mathbf{\Lambda}_{\mathcal{E}} \otimes \mathbf{I} + \mathbf{I} \otimes \mathbf{\Lambda}_{\mathcal{E}} &= \begin{bmatrix} \lambda_{j_1} & 0 \\ 0 & \lambda_{j_2} \end{bmatrix} \otimes \begin{bmatrix} 1 & 0 \\ 0 & 1 \end{bmatrix} + \begin{bmatrix} 1 & 0 \\ 0 & 1 \end{bmatrix} \otimes \begin{bmatrix} \lambda_{j_1} & 0 \\ 0 & \lambda_{j_2} \end{bmatrix} \\ &= \begin{bmatrix} 2\lambda_{j_1} & 0 & 0 & 0 \\ 0 & \lambda_{j_1} + \lambda_{j_2} & 0 & 0 \\ 0 & 0 & \lambda_{j_2} + \lambda_{j_1} & 0 \\ 0 & 0 & 0 & 2\lambda_{j_2} \end{bmatrix}.\end{aligned} \tag{2.38}$$

The four-dimensional array $\mathbf{\Omega}_2$ can be expressed as

$$\mathbf{\Omega}_2 = (11, 12, 21, 22)\,,$$

from which we obtain the coefficients (a_j, b_j) by determining the multiplicity of the numbers 1 and 2 for each element j in $\mathbf{\Omega}_2$.

As $\tilde{\mathbf{\Lambda}}_{\mathcal{E},i}$ is diagonal by construction, its eigenvalues are positioned on the diagonal and take the form of

$$a\lambda_{j_1} + b\lambda_{j_2}, \quad a, b \in \mathbb{N} : a + b = i. \tag{2.39}$$

We, therefore, conclude from (2.35) that the eigenvalues of $\mathbf{\Theta}_i^{\mathcal{E}}$ and $\mathbf{\Theta}_i^{\mathcal{C}}$ can be written as

$$\lambda_l - (a\lambda_{j_1} + b\lambda_{j_2}), \quad a, b \in \mathbb{N} : a + b = i, \quad \forall \lambda_l \in \mathrm{Spect}(\Lambda_{\mathcal{E}}), \tag{2.40}$$

$$\lambda_l - (a\lambda_{j_1} + b\lambda_{j_2}), \quad a, b \in \mathbb{N} : a + b = i, \quad \forall \lambda_l \in \mathrm{Spect}(\Lambda_{\mathcal{C}}). \tag{2.41}$$

Equations (2.40) and (2.41) lead precisely to the inner and outer non-resonance conditions (2.13) and (2.9), respectively, related to the i^{th}-order of the SSM expansion. If there exists an inner resonance in (2.40), for a particular order i, the matrix $\mathbf{\Theta}_i^{\mathcal{E}}$ will be singular. This means that for a nonzero right-hand side of equation (2.33), there will be no solution for $\mathrm{vec}(\mathbf{W}_i^{\mathcal{E}})$. However, we can then set $\mathbf{R}_i$ in equation (2.33) equal to -$\mathbf{B}_i^{\mathcal{E}}$, which gives a zero right-hand side. As a consequence, the solution $\mathrm{vec}(\mathbf{W}_i^{\mathcal{E}})$ has to be in the kernel of $\mathbf{\Theta}_i^{\mathcal{E}}$, creating an opportunity to remove resonant terms in the expression for $\mathbf{W}(\mathbf{z})$. The presence of an outer resonance in (2.41) will result in a breakdown of the SSM. In this case, we do not have the freedom to alter the right-hand side of equation (2.34).

2.5 Reduced dynamics on the autonomous SSM

2.5.1 Near-inner-resonances

Based on eq. (2.33), the polynomial dynamics on the SSM must be parameterized as nonlinear when an inner resonance arises in the spectral subspace $\mathcal{E}$ over which the SSM is constructed. When the eigenvalues λ_{j_1} and λ_{j_2} are complex conjugate, the inner non-resonance conditions (2.13) will never be violated. However, as explained by Szalai et al. [16], for a lightly damped spectral subspace corresponding to a complex pair of eigenvalues, the following near-inner-resonance conditions will always hold:

$$2\lambda_{j_1} + \bar{\lambda}_{j_1} \approx \lambda_{j_1}, \quad \lambda_{j_1} + 2\bar{\lambda}_{j_1} \approx \bar{\lambda}_{j_1}. \tag{2.42}$$

These near-inner-resonances, in turn, will lead to small denominators in the coefficients related to the monomial terms $z_{j_1}^2 \bar{z}_{j_1}$ and $z_{j_1} \bar{z}_{j_1}^2$ in the third-order coefficient matrix $\mathbf{W}_3^{\mathcal{E}}$ (cf. eqs. (2.33-2.34)). Such small denominators generally reduce the domain of convergence of the Taylor series we compute for $\mathbf{W}(\mathbf{z})$.

Luckily, we have the freedom to remove these resonant terms in $\mathbf{W}_3^{\mathcal{E}}$ by setting $\mathbf{R}_3$ on the right-hand side of equation (2.28) equal to -$\mathbf{B}_3^{\mathcal{E}}$. However, due to the particular diagonal structure of equation (2.33), it is possible to specifically remove the resonant terms $z_{j_1}^2 \bar{z}_{j_1}$ and $z_{j_1} \bar{z}_{j_1}^2$ in $\mathbf{W}_3^{\mathcal{E}}$ by only setting the coefficients in $\mathbf{R}_3$ related to the the resonant terms equal to the coefficients in -$\mathbf{B}_3^{\mathcal{E}}$. This corresponds

to a mixed parameterization style, as explained in Haro et al. [25], which can also be applied to higher orders.

The third order near-inner-resonance condition (2.42) can be extended to higher-order near-inner-resonances by introducing an appropriate resonance-closeness measure

$$I(a,b,\lambda_l) = \left| \frac{\langle \mathbf{c}(a,b), \mathbf{v}_{\mathcal{E}}(\lambda_l) \rangle}{\|\mathbf{c}(a,b)\| \, \|\mathbf{v}_{\mathcal{E}}(\lambda_l)\|} \right| < \delta, \quad 0 < \delta \ll 1, \tag{2.43}$$

for δ sufficiently small, with

$$\mathbf{c}(a,b) = \begin{bmatrix} a \\ b \\ -1 \end{bmatrix}, \quad \mathbf{v}_{\mathcal{E}}(\lambda_l) = \begin{bmatrix} \lambda_{j_1} \\ \lambda_{j_2} \\ \lambda_l \end{bmatrix}, \quad a,b \in \mathbb{N}, \quad \forall \lambda_l \in \{\lambda_{j_1}, \lambda_{j_2}\}.$$

The resonance-closeness measure I takes values between $I_{\min} = 0$ and $I_{\max} = 1$. We consider δ to be small when δ is at least one order of magnitude smaller than $I_{\max}$. In the presence of near-inner resonances, the choice of δ affects the accuracy of the SSM and the reduced dynamics. If the observed invariance error of the SSM (cf. section 2.6) is unsatisfactory, δ can be increased in order to account for even weaker near-inner resonances.

In the case of an exact inner resonance, $I(a,b,\lambda_l)$ in equation (2.43) will be zero. Using the same measure, we can also quantify closeness to outer resonances by substituting all possible $\lambda_l \notin \{\lambda_{j_1}, \lambda_{j_2}\}$ into (2.43).

2.5.2 Instantaneous amplitude and frequency

When the chosen spectral subspace $\mathcal{E}$ is spanned by a complex pair of eigenvectors, which in turn corresponds to a complex conjugate pair of eigenvalues λ_{j_1} and λ_{j_2}, the complex conjugate pair of coordinates z_{j_1} and $z_{j_2} = \bar{z}_{j_1}$ in the reduced dynamics $\mathbf{R}(\mathbf{z})$ can be expressed in real amplitude-phase coordinates (ρ, θ) as

$$z_{j_1} = \rho \mathrm{e}^{\mathrm{i}\theta}, \quad \bar{z}_{j_1} = \rho \mathrm{e}^{-\mathrm{i}\theta}. \tag{2.44}$$

Assume now that the spectral subspace $\mathcal{E}$ has higher-order near-inner-resonances, i.e.

$$I(a,b,\lambda_{j_1}) < \delta, \quad I(b,a,\lambda_{j_2}) < \delta, \quad (a,b) \in \{(2,1),(3,2),(4,3),\ldots\} = S,$$

and, additionally, the coefficients in $\mathbf{B}_i^{\mathcal{E}}$ for $i = 3, 5, 7\ldots$, corresponding to the monomial terms $z_{j_1}^a \bar{z}_{j_1}^b$ and $z_{j_1}^s \bar{z}_{j_1}^r$, on the right hand side of (2.28) are nonzero. We then obtain the following expression for the reduced dynamics on the spectral submanifold $\mathcal{W}(\mathcal{E})$:

$$\dot{\mathbf{z}} = \mathbf{R}(\mathbf{z}) = \begin{bmatrix} \lambda_{j_1} z_{j_1} + \sum\limits_{\forall (a,b) \in S} \gamma_{a,b} z_{j_1}^a \bar{z}_{j_1}^b \\ \bar{\lambda}_{j_1} \bar{z}_{j_1} + \sum\limits_{\forall (a,b) \in S} \bar{\gamma}_{a,b} z_{j_1}^b \bar{z}_{j_1}^a \end{bmatrix}. \tag{2.45}$$

Here $\gamma_{a,b}$ depends directly on $\mathbf{B}_i^{\mathcal{E}}$, which is known for the current order i. Alternatively, $\gamma_{a,b}$ will be equal to the sum of all nonzero coefficients in $\mathbf{R}_i$, with $i = a + b$ corresponding to the monomial term $z_{j_1}^a \bar{z}_{j_1}^b$. Substituting equation (2.44) into the left- and right-hand side of equation (2.45) gives

$$\dot{\rho} = \mathrm{Re}(\lambda_{j_1})\rho + \sum_{\forall (a,b) \in S} \mathrm{Re}(\gamma_{a,b}) \rho^{(a+b)}, \tag{2.46}$$

$$\omega = \dot{\theta} = \mathrm{Im}(\lambda_{j_1}) + \sum_{\forall (a,b) \in S} \mathrm{Im}(\gamma_{a,b}) \rho^{(a+b-1)}. \tag{2.47}$$

for $\rho \neq 0$. Equation (2.47) determines an instantaneous frequency $\dot{\theta}$ that depends solely upon ρ. To any ρ value, we assign an instantaneous physically observable amplitude by defining

$$A(\rho) = \frac{1}{2\pi} \int_0^{2\pi} |\mathbf{T}_{\mathbf{y}} \mathbf{W}(\mathbf{z}(\rho, \theta))| \, d\theta, \tag{2.48}$$

where the transformation matrix $\mathbf{T}_{\mathbf{y}}$ acts on $\mathbf{W}(\mathbf{z}(\rho, \theta))$ and hence returns physical position coordinates $\mathbf{y} \in \mathbb{R}^n$ of our mechanical system (4.2). Then, following the definition of Szalai et al. [16], we define a backbone curve for the reduced dynamics on the SSM to be the parameterized curve

$$\mathcal{B} = \{\omega(\rho), A(\rho)\}_{\rho \in \mathbb{R}^+}. \tag{2.49}$$

An illustration of how the parametrized SSM, constructed over a lightly damped spectral subspace $\mathcal{E}$, can be used to construct the backbone curve $\mathcal{B}$ is shown in figure 2.1.

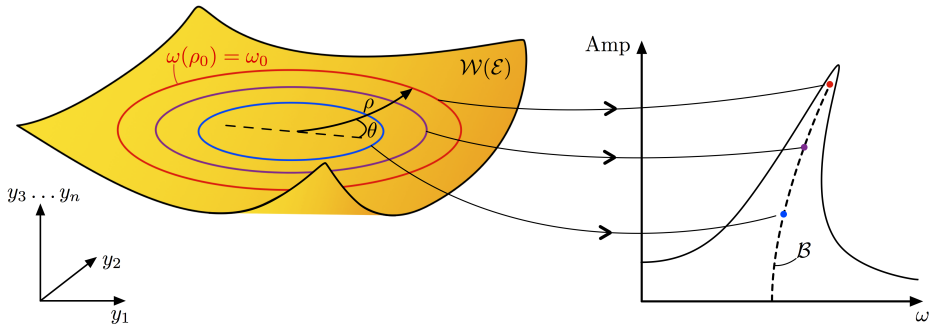

Figure 2.1: Illustration of the backbone curve construction using the parameterized SSM. For each fixed radius ρ_0 on the SSM, we can identify an instantaneous frequency (2.47). By averaging the physical coordinates over one period, evaluated on the SSM constraint to the fixed radius ρ_0, we obtain the instantaneous amplitude (2.48). For each $\rho = \rho_0 \in \mathbb{R}^+$, we obtain a point of the curve $\mathcal{B}$, shown in the amplitude-frequency plot. The continuous black line in the amplitude-frequency plot consists out of periodic orbits of the periodically forced system for varying forcing frequency.

2.6 Invariance measure and order selection

As stated in Theorem 1, the unique SSM is captured and approximated by Taylor expanding up to order $\sigma_{\text{out}}(\mathcal{E}) + 1$. The outer spectral quotient σ_{out}, is defined as the integer part of the ratio between the strongest decay rate of the linearized oscillations outside $\mathcal{E}$ and the weakest decay rate of the linearized oscillations inside $\mathcal{E}$. As explained by Géradin and Rixen [29], a first-order approximation of the real part of each eigenvalue of a lightly damped mechanical system, of the form (2.1), scales with the square of its natural eigenfrequency. This means that for a discretized non-conservative mechanical system with a high number of degrees of freedom, the order of the SSM needed to be unique can become large. An illustration of this is shown in figure 2.2.

As the outer spectral quotient $\sigma_{\text{out}}(\mathcal{E})$ increases, trajectories transverse to the slow SSM die out fast compared to trajectories on the SSM, as indicated in the lower part of figure 2.2. This collapsing nature of the transverse trajectories makes it harder to distinguish between the unique SSM and any other two-dimensional invariant manifold tangent the same modal subspace. In order to approximate the SSMs with a large outer spectral quotient, without having to compute the SSMs up to extremely high orders, we introduce an invariance error measure, δ_{inv}, that quantifies the accuracy of the computed invariant manifolds and the reduced dynamics on them.

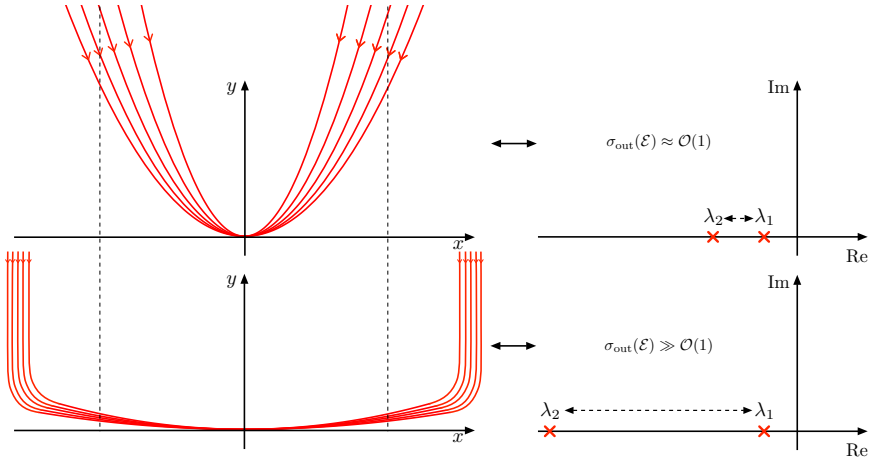

Figure 2.2: Illustration of a system having a low outer spectral quotient (top) and a high outer spectral quotient (bottom).

The invariance error measure compares trajectories of the full system $\mathbf{x}_i$, with trajectories of the reduced system $\tilde{\mathbf{x}}_i$. Trajectories from the full and reduced system are launched from a circle with fixed radius ρ_0, from the origin, and integrated until the reduced trajectories cross the inner circle of radius $\rho_\epsilon < \rho_0$, therefore removing the time dependency. An illustration of this is shown in figure 2.3. We mathematically formalize the invariance error as follows

$$\delta_{\text{inv}} = \frac{1}{N}\sum_{i=1}^{N} \frac{\text{dist}(i)}{\max\limits_{\theta \in S^1} \|\tilde{\mathbf{x}}(\rho_0, \theta)\|_2}, \quad \text{dist}(i) = \max \left\| \mathbf{x}_i|_{\rho_0}^{\rho_\epsilon} - \tilde{\mathbf{x}}_i|_{\rho_0}^{\rho_\epsilon} \right\|_2, \tag{2.50}$$

where we take the average of the maximum Euclidean distance between N trajectories $\mathbf{x}_i$ and $\tilde{\mathbf{x}}_i$, for $i = 1, \ldots, N$, traveling from a circle with radius ρ_0 to an inner circle with radius ρ_ϵ, and normalize the result by the maximum Euclidean distance from the origin to the circle with fixed radius ρ_0.

If the invariance error δ_{inv}, for a given order of the approximated SSM, is above a certain pre-specified bound, then the order of the SSM approximation has to be further increased.

2.7 Applications

We now apply our computational algorithm to three different mechanical systems. The numerical results and figures we show have all been generated directly by SSMtool.

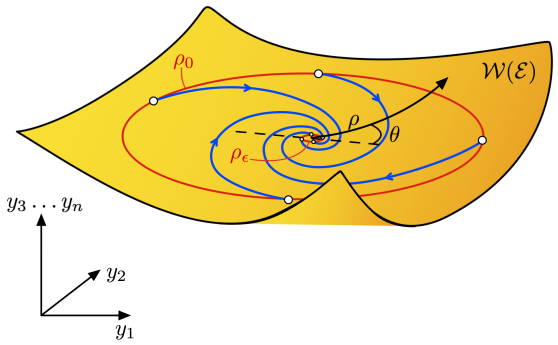

Figure 2.3: Illustration of the invariance error measure.

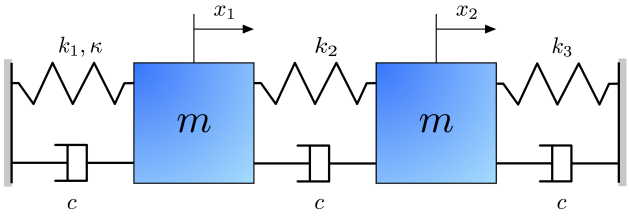

Figure 2.4: Two-degree-of-freedom modified Shaw–Pierre example.

2.7.1 The modified Shaw–Pierre example: Inner resonances

We first consider a slightly modified version of the example of Shaw and Pierre [30], shown in figure 2.4. The original Shaw–Pierre example involves a two-degree-of-freedom mechanical oscillator, which is modified in the current setting such that the damping matrix is proportional to the mass and stiffness matrices (also known as Rayleigh damping, see, e.g., Géradin and Rixen [29]). For this problem, the SSM coefficients have been explicitly calculated in Szalai et al. [16], up to third order.

For $k_1 = k_2 = k_3 = k$, the equations of motion of the system are

$$\begin{bmatrix} m & 0 \\ 0 & m \end{bmatrix} \begin{bmatrix} \ddot{x}_1 \\ \ddot{x}_2 \end{bmatrix} + \begin{bmatrix} 2c & -c \\ -c & 2c \end{bmatrix} \begin{bmatrix} \dot{x}_1 \\ \dot{x}_2 \end{bmatrix} + \begin{bmatrix} 2k & -k \\ -k & 2k \end{bmatrix} \begin{bmatrix} x_1 \\ x_2 \end{bmatrix} + \begin{bmatrix} \kappa x_1^3 \\ 0 \end{bmatrix} = \begin{bmatrix} 0 \\ 0 \end{bmatrix}, \tag{2.51}$$

with the linear part having the eigenvalue pairs

$$\lambda_{1,2} = -\frac{c}{2} \pm \mathrm{i}\sqrt{k\left(1 - \frac{c^2}{4k}\right)}, \quad \lambda_{3,4} = -\frac{3c}{2} \pm \mathrm{i}\sqrt{3k\left(1 - \frac{3c^2}{4k}\right)}, \tag{2.52}$$

when both linear normal modes are underdamped ($c < 2\sqrt{k/3}$) and the mass m is equal to 1 kg. As noted in Szalai et al. [16], the two spectral subspaces, $\mathcal{E}_1$ and $\mathcal{E}_2$, corresponding to the eigenvalues $\lambda_{1,2}$ and $\lambda_{3,4}$ respectively, have the outer and inner spectral quotients

$$\sigma_{\text{out}}(\mathcal{E}_1) = \text{Int}\left[\frac{\text{Re}\lambda_3}{\text{Re}\lambda_1}\right] = 3, \quad \sigma_{\text{out}}(\mathcal{E}_2) = \left[\frac{\text{Re}\lambda_1}{\text{Re}\lambda_3}\right] = 0, \tag{2.53}$$

$$\sigma_{\text{in}}(\mathcal{E}_1) = \text{Int}\left[\frac{\text{Re}\lambda_1}{\text{Re}\lambda_1}\right] = 1, \quad \sigma_{\text{in}}(\mathcal{E}_2) = \left[\frac{\text{Re}\lambda_3}{\text{Re}\lambda_3}\right] = 1. \tag{2.54}$$

The non-resonance conditions (2.9) and (2.13) are satisfied for both of these spectral subspaces, thus, there exist two two-dimensional analytic SSMs, $\mathbf{W}(\mathcal{E}_1)$ and $\mathbf{W}(\mathcal{E}_2)$, that are unique among all C^4 and C^1 invariant manifolds tangent to $\mathcal{E}_1$ and $\mathcal{E}_2$, respectively.

Rewriting the equations of motion (2.51) in first-order form, we obtain

$$\frac{d}{dt}\begin{bmatrix} x_1 \\ x_2 \\ \dot{x}_1 \\ \dot{x}_2 \end{bmatrix} = \underbrace{\begin{bmatrix} 0 & 0 & 1 & 0 \\ 0 & 0 & 0 & 1 \\ -2k & k & -2c & c \\ k & -2k & c & -2c \end{bmatrix}}_{\mathbf{A}} \begin{bmatrix} x_1 \\ x_2 \\ \dot{x}_1 \\ \dot{x}_2 \end{bmatrix} + \underbrace{\begin{bmatrix} 0 \\ 0 \\ -\kappa x_1^3 \\ 0 \end{bmatrix}}_{\mathbf{F}(\mathbf{x})}. \tag{2.55}$$

Computing $\mathbf{W}(\mathcal{E}_1)$ and $\mathbf{W}(\mathcal{E}_2)$

The spectral submanifolds, $\mathbf{W}(\mathcal{E}_1)$ and $\mathbf{W}(\mathcal{E}_2)$, will be tangent to their corresponding spectral subspaces, $\mathcal{E}_1$ and $\mathcal{E}_2$. To compute $\mathbf{W}(\mathcal{E}_1)$, we diagonalize (2.55) by introducing a linear change of coordinates $\mathbf{x} = \mathbf{T}\mathbf{q}$, where the columns of $\mathbf{T}$ contain the eigenvectors of (2.55), i.e.,

$$\mathbf{T} = [\mathbf{v}_1, \bar{\mathbf{v}}_1, \mathbf{v}_3, \bar{\mathbf{v}}_3] = \begin{bmatrix} 1 & 1 & 1 & 1 \\ 1 & 1 & -1 & -1 \\ \lambda_1 & \bar{\lambda}_1 & \lambda_3 & \bar{\lambda}_3 \\ \lambda_1 & \bar{\lambda}_1 & -\lambda_3 & -\bar{\lambda}_3 \end{bmatrix}. \tag{2.56}$$

We can rewrite equation (2.55) in the form of (2.22)

$$\dot{\mathbf{q}} = \text{diag}(\lambda_1, \bar{\lambda}_1, \lambda_3, \bar{\lambda}_3)\mathbf{q} + \mathbf{T}^{-1}\mathbf{F}(\mathbf{T}\mathbf{q}) = \mathbf{\Lambda}\mathbf{q} + \mathbf{G}(\mathbf{q}). \tag{2.57}$$

To compute $\mathbf{W}(\mathcal{E}_2)$, equation (2.55) must be diagonalized via a similar linear change of coordinates $\mathbf{x} = \tilde{\mathbf{T}}\tilde{\mathbf{q}}$, where the columns of $\tilde{\mathbf{T}}$ now contain the eigenvectors of (2.55) in the following order

$$\mathbf{T} = [\mathbf{v}_3, \bar{\mathbf{v}}_3, \mathbf{v}_1, \bar{\mathbf{v}}_1] = \begin{bmatrix} 1 & 1 & 1 & 1 \\ -1 & -1 & 1 & 1 \\ \lambda_3 & \bar{\lambda}_3 & \lambda_1 & \bar{\lambda}_1 \\ -\lambda_3 & -\bar{\lambda}_3 & \lambda_1 & \bar{\lambda}_1 \end{bmatrix}. \tag{2.58}$$

Similarly, equation (2.55) can be written in the form of (2.22), i.e.

$$\dot{\tilde{\mathbf{q}}} = \operatorname{diag}(\lambda_3, \bar{\lambda}_3, \lambda_1, \bar{\lambda}_1)\tilde{\mathbf{q}} + \tilde{\mathbf{T}}^{-1}\mathbf{F}(\tilde{\mathbf{T}}\tilde{\mathbf{q}}) = \tilde{\mathbf{\Lambda}}\tilde{\mathbf{q}} + \tilde{\mathbf{G}}(\tilde{\mathbf{q}}). \tag{2.59}$$

The polynomial expressions for the nonlinearities $\mathbf{G}(\mathbf{q})$ and $\tilde{\mathbf{G}}(\tilde{\mathbf{q}})$ only contain cubic nonlinearities and therefore only the nonlinear coefficient matrices $\mathbf{G}_3$ and $\tilde{\mathbf{G}}_3$ will be non-zero. We will compute $\mathbf{W}(\mathcal{E}_1)$ and $\mathbf{W}(\mathcal{E}_2)$ for the following parameter values

$$k = 1 \text{ N m}^{-1}, \quad c = 0.03 \text{ N s m}^{-1}, \quad \kappa = 0.5 \text{ N m}^{-3}, \quad \delta = 0.05. \tag{2.60}$$

We justify the choice up to which order we have to approximate the SSMs to get an accurate reduced order model, by evaluating the invariance error (2.50) for different approximation orders. For a given fixed radius $\rho_0 = 0.35$ we take 50 initial points, each corresponding to an angle θ_0, uniformly distributed in S^1.

As the order of the approximation of $\mathbf{W}(\mathcal{E}_1)$ and $\mathbf{W}(\mathcal{E}_2)$ is increased, the error δ_{inv} is substantially reduced, as expected. We conclude that the 15^{th} order approximation for both spectral submanifolds is high enough to guarantee them to be accurate for oscillation amplitudes up to $\rho_0 = 0.35$, which corresponds to a physical maximum displacement of $|x_1| \approx 0.66$ m and $|x_2| \approx 0.71$ m for $\mathbf{W}(\mathcal{E}_1)$ and $|x_1| \approx 0.73$ m and $|x_2| \approx 0.66$ m for $\mathbf{W}(\mathcal{E}_2)$.

We observe that the following near-inner-resonances conditions are satisfied within the spectral subspaces $\mathcal{E}_1$ and $\mathcal{E}_2$, see table (2.1) and (2.2) respectively.

We intend to remove the near-inner resonant terms $z_1^2 z_2$, $z_1 z_2^2$, $z_1^3 z_2^2$, $z_1^2 z_2^3$, $z_1^4 z_2^3$, $z_1^3 z_2^4$, $z_1^5 z_2^4$, $z_1^4 z_2^5$, $z_1^6 z_2^5$, $z_1^5 z_2^6$, $z_1^7 z_2^6$, $z_1^6 z_2^7$, $z_1^8 z_2^7$ and $z_1^7 z_2^8$ in the expressions of $\mathbf{W}(\mathcal{E}_1)$ and $\mathbf{W}(\mathcal{E}_2)$ and add them to the polynomial expressions for the reduced dynamics on the spectral submanifolds. Due to the choice of nonlinearities, all the coefficients of $\mathbf{W}(\mathcal{E}_1)$ and $\mathbf{W}(\mathcal{E}_2)$ corresponding to even powers in $|\mathbf{z}|$ are zero. Solving the partitioned Sylvester equations (2.33) and (2.34) for $\mathbf{W}_i^{\mathcal{E}}$ and $\mathbf{W}_i^{\mathcal{C}}$ for orders $i = 2, \ldots, 15$, we obtain the lower-dimensional projections of the full phase space for the 15^{th} order approximations of $\mathbf{W}(\mathcal{E}_1)$ and $\mathbf{W}(\mathcal{E}_2)$, shown in figure 2.6. The images are directly obtained from SSMtool, which detects resonant terms and adds them to the reduced dynamics $\mathbf{R}(\mathbf{z})$ when solving the partitioned Sylvester equations (2.33) and (2.34).

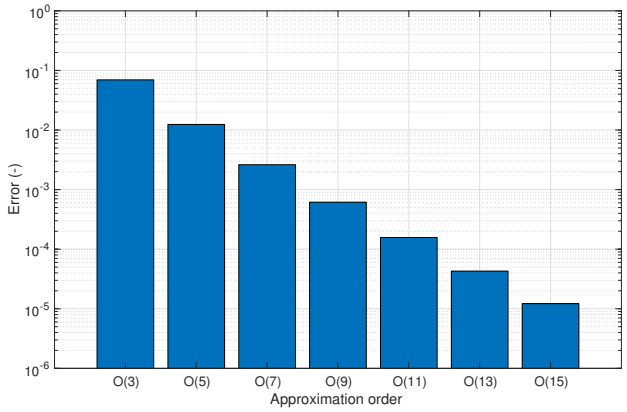

(a)

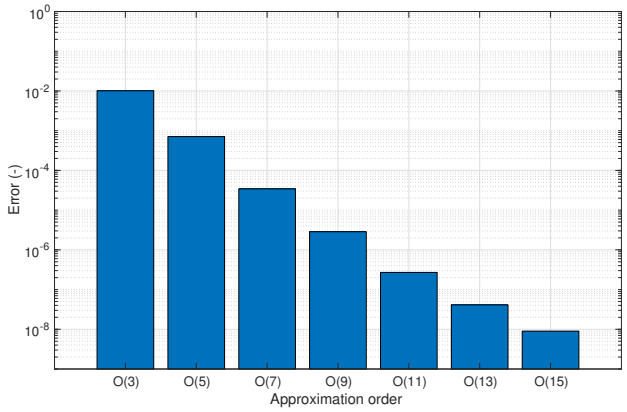

(b)

Figure 2.5: Normalized error for the 3^{th}-15^{th} order approximation of $\mathbf{W}(\mathcal{E}_1)$ (2.5(a)) and $\mathbf{W}(\mathcal{E}_2)$ (2.5(b)) for 50 evenly distributed initial positions lying on a fixed radius $\rho_0 = 0.35$ and $\theta_0 \in S^1$. For each trajectory traveling between ρ_0 and $\rho_\epsilon = 0.01$, we identify the maximum error and take the average over all trajectories.

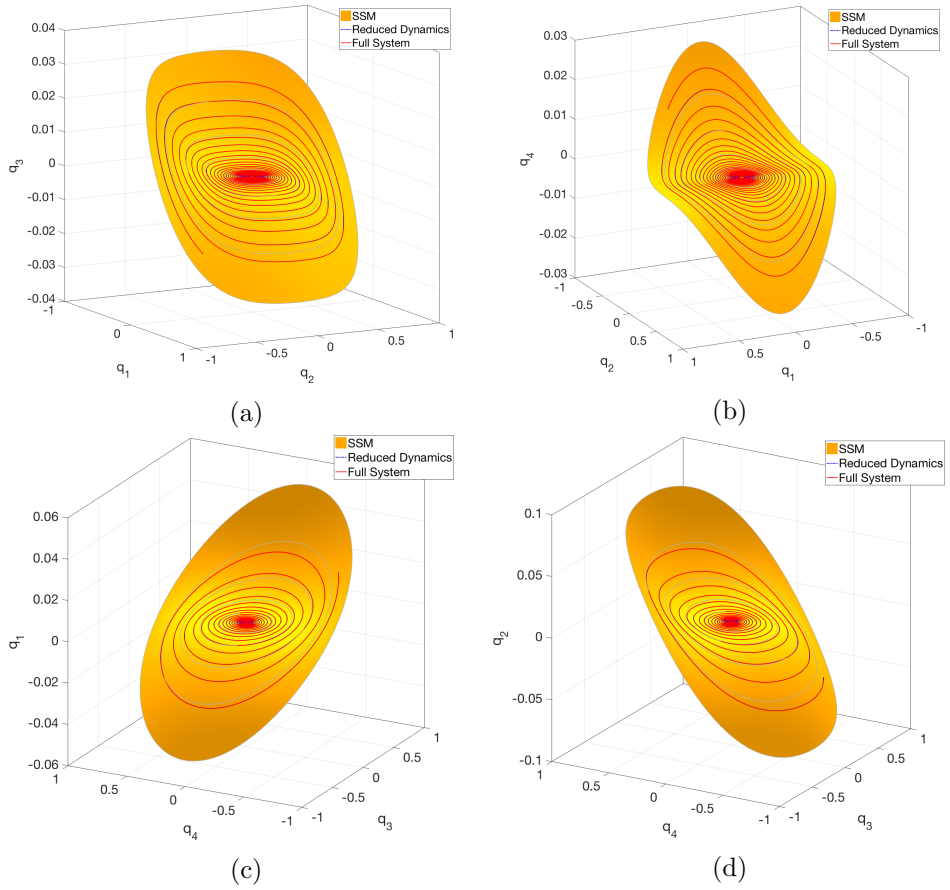

Figure 2.6: Lower-dimensional projections of the full phase space, showing the 15^{th} order approximations of $\mathbf{W}(\mathcal{E}_\mathbf{1})$ and $\mathbf{W}(\mathcal{E}_2)$. Figures 2.6(a) and 2.6(b) show the spectral submanifold $\mathbf{W}(\mathcal{E}_1)$ tangent to $\mathcal{E}_1$. Figures 2.6(c) and 2.6(d) show the spectral submanifold $\mathbf{W}(\mathcal{E}_2)$ tangent to $\mathcal{E}_2$. The dashed curves indicate different projections of a trajectory of the reduced system $\mathbf{R}(\mathbf{z})$, starting from the initial position $\rho = 0.35$ and $\theta = 1$. The solid curves represent trajectories of the full system for the same initial position. The solid gray curves represent contour lines of equal parameterized distance ρ.

$\mathcal{E}_1$				
	a	b	λ_l	I
$\mathcal{O}(\lvert\mathbf{z}\rvert^3)$	2	1	λ_1	0.00707
	1	2	$\bar{\lambda}_1$	0.00707
$\mathcal{O}(\lvert\mathbf{z}\rvert^5)$	3	2	λ_1	0.00926
	2	3	$\bar{\lambda}_1$	0.00926
$\mathcal{O}(\lvert\mathbf{z}\rvert^7)$	4	3	λ_1	0.01019
	3	4	$\bar{\lambda}_1$	0.01019
$\mathcal{O}(\lvert\mathbf{z}\rvert^9)$	5	4	λ_1	0.01069
	4	5	$\bar{\lambda}_1$	0.01069
$\mathcal{O}(\lvert\mathbf{z}\rvert^{11})$	6	5	λ_1	0.01100
	5	6	$\bar{\lambda}_1$	0.01100
$\mathcal{O}(\lvert\mathbf{z}\rvert^{13})$	7	6	λ_1	0.01121
	6	7	$\bar{\lambda}_1$	0.01121
$\mathcal{O}(\lvert\mathbf{z}\rvert^{15})$	8	7	λ_1	0.01136
	7	8	$\bar{\lambda}_1$	0.01136

Table 2.1: Near-inner-resonances for $\mathcal{E}_1$ with $\delta = 0.05$.

Reduced Dynamics

The near-inner resonances within the spectral subspaces $\mathcal{E}_1$ and $\mathcal{E}_2$ introduce nonlinear terms in the reduced dynamics on the spectral submanifolds. The reduced dynamics on $\mathbf{W}(\mathcal{E}_1)$ and $\mathbf{W}(\mathcal{E}_2)$ is of the general form (2.45). After transforming to polar coordinates, we obtain the following reduced equations for the in-phase mode of the system from SSMtool:

$$\begin{aligned}\dot{\rho} =& -0.015\rho - 0.00079121\rho^5 - 0.0012708\rho^7 \\ &+ 0.0090446\rho^9 - 0.03569\rho^{11} + 0.12918\rho^{13} - 0.45878\rho^{15},\end{aligned} \tag{2.61}$$

$$\begin{aligned}\omega =& 0.99989 + 0.37504\rho^2 - 0.60592\rho^4 + 1.1713\rho^6 \\ &- 2.5137\rho^8 + 5.7885\rho^{10} - 14.01\rho^{12} + 35.159\rho^{14}.\end{aligned} \tag{2.62}$$

$\mathcal{E}_2$				
	a	b	λ_l	I
$\mathcal{O}(\lvert\mathbf{z}\rvert^3)$	2	1	λ_3	0.01225
	1	2	$\bar{\lambda}_3$	0.01225
$\mathcal{O}(\lvert\mathbf{z}\rvert^5)$	3	2	λ_3	0.01604
	2	3	$\bar{\lambda}_3$	0.01604
$\mathcal{O}(\lvert\mathbf{z}\rvert^7)$	4	3	λ_3	0.01765
	3	4	$\bar{\lambda}_3$	0.01765
$\mathcal{O}(\lvert\mathbf{z}\rvert^9)$	5	4	λ_3	0.01852
	4	5	$\bar{\lambda}_3$	0.01852
$\mathcal{O}(\lvert\mathbf{z}\rvert^{11})$	6	5	λ_3	0.01905
	5	6	$\bar{\lambda}_3$	0.01905
$\mathcal{O}(\lvert\mathbf{z}\rvert^{13})$	7	6	λ_3	0.01941
	6	7	$\bar{\lambda}_3$	0.01941
$\mathcal{O}(\lvert\mathbf{z}\rvert^{15})$	8	7	λ_3	0.01967
	7	8	$\bar{\lambda}_3$	0.01967

Table 2.2: Near-inner-resonances for $\mathcal{E}_2$ with $\delta = 0.05$.

The reduced dynamics for the out-of-phase mode of the system is obtained from SSMtool as

$$\begin{aligned}\dot{\rho} =& -0.045\rho + 0.016267\rho^5 + 0.02614\rho^7 \\ &+ 0.015714\rho^9 - 0.012768\rho^{11} - 0.03437\rho^{13} - 0.0308\rho^{15},\end{aligned} \tag{2.63}$$

$$\begin{aligned}\omega =& 1.7315 + 0.21658\rho^2 + 0.19904\rho^4 + 0.14858\rho^6 \\ &+ 0.072849\rho^8 + 0.017657\rho^{10} + 0.004087\rho^{12} - 0.011824\rho^{14},\end{aligned} \tag{2.64}$$

where we set the order of computations to $\mathcal{O}(15)$. Both instantaneous frequencies (2.62) and (2.64) depend on ρ only. The two red curves in figure 2.7(a) and figure 2.7(b) represent the $\mathcal{O}(15)$ backbone curves for the in-phase and out-of-phase mode of the mechanical system, whereas the blue curves display the $\mathcal{O}(3)$ approximations of the backbone curves.

We used the numerical continuation software COCO [31] to find periodic orbits of the periodically forced system for a fixed forcing amplitude while varying the forcing frequency. We have extensively optimized the continuation parameters to ensure accurate but fast results. In the current work, COCO is used as an off-the-shelf open-source benchmark to which we compare SSMtool as a stand-alone package.

The promising techniques of Blanc et al. [19] and Renson et al. [21] would be expected to perform better than COCO in these computations, but have no available open-source implementations at this point.

The equations of motion of the forced system are

$$\begin{bmatrix} m & 0 \\ 0 & m \end{bmatrix} \begin{bmatrix} \ddot{x}_1 \\ \ddot{x}_2 \end{bmatrix} + \begin{bmatrix} 2c & -c \\ -c & 2c \end{bmatrix} \begin{bmatrix} \dot{x}_1 \\ \dot{x}_2 \end{bmatrix} + \begin{bmatrix} 2k & -k \\ -k & 2k \end{bmatrix} \begin{bmatrix} x_1 \\ x_2 \end{bmatrix} + \begin{bmatrix} \kappa x_1^3 \\ 0 \end{bmatrix} = \begin{bmatrix} A \cos \omega t \\ 0 \end{bmatrix}, \tag{2.65}$$

where we use the same parameter values (2.60) and introduced a forcing term with amplitude A and forcing frequency ω. The resulting periodic response amplitudes are shown in figure 2.7(a) and figure 2.7(b) in black for a forcing amplitude of $A = 0.05$ N and $A = 0.2$ N, respectively. As shown, the $\mathcal{O}(15)$ approximations for both backbone curves fit the forced peak responses well. The computational time for the continuation curve in figure 2.7(a) takes 8 minutes and 6 seconds on a Mac Pro 2×3.06 GHz 6-Core Intel Xeon, which technically corresponds to a single point on the backbone curve. The computational time for the backbone curve, extracted from the 15^{th} order approximation of $\mathbf{W}(\mathcal{E}_1)$, is approximately 3 minutes, resulting in a parameterized curve that can be subsequently evaluated at any required frequency. The computational time for the continuation curve in figure 2.7(b) takes a total of 11 minutes and 16 seconds, whereas the computational time for the backbone curve, extracted from the 15^{th} order approximation of $\mathbf{W}(\mathcal{E}_2)$, is also approximately 3 minutes.

2.7.2 The modified Shaw–Pierre example: Outer resonances

We now consider the same analytic example as in section 2.7.1, but with the linear springs k_1, k_2, k_3 and the damping c tuned such that there are near-outer resonances and no near-inner resonances. Here we only compute $\mathbf{W}(\mathcal{E}_1)$, the slow SSM arising from the slow complex pair of eigenvalues. By definition, it is impossible to obtain an outer resonance for the spectral subspace corresponding to the remaining fast complex pair of eigenvalues.

The current example is taken from work of Cirillo et al. [32], where a global parameterization method is proposed for the computation of invariant manifolds in a domain where the stringent non-resonance conditions of analytic linearization hold.

For the parameter values

$$k_1 = k_3 = 1 \text{ N m}^{-1}, \quad k_2 = 4.005 \text{ N m}^{-1}, \quad c = 0.4 \text{ N s m}^{-1}, \quad \kappa = 0.5 \text{ N m}^{-3}, \quad \delta = 0.05, \tag{2.66}$$

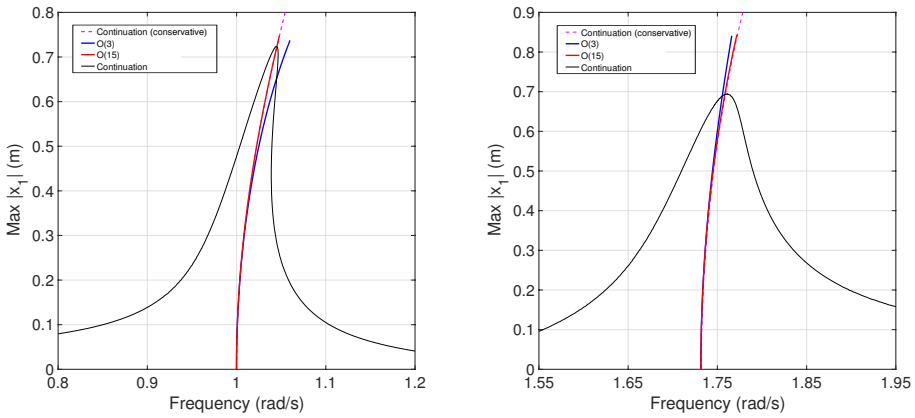

(a) (b)

Figure 2.7: Backbone curves and periodically forced responses for different amplitudes of the mechanical system (2.51). Figure 2.7(a) shows the $\mathcal{O}(15)$ (red) and $\mathcal{O}(3)$ (blue) approximations of the backbone curves for the in-phase mode of the system. Figure 2.7(b) shows the $\mathcal{O}(15)$ (red) and $\mathcal{O}(3)$ (blue) approximations of the backbone curves for the out-of-phase mode of the system. Black lines mark amplitudes of periodic orbits of the periodically forced system for different forcing amplitudes for varying forcing frequency. The dashed lines (magenta) represent the backbone curves extracted from COCO in the conservative limit of the mechanical system, without any forcing.

the system has two complex conjugate pairs of eigenvalues with

$$\lambda_1 = -0.2 + 0.9798\mathrm{i},$$
$$\lambda_2 = -0.6 + 2.9411\mathrm{i},$$

and their conjugates. We construct the two-dimensional spectral subspace $\mathcal{E}_1$ corresponding to the first conjugate pair of slow eigenvalues λ_1 and $\bar{\lambda}_1$, whose inner and outer spectral quotients are

$$\sigma_{\mathrm{in}}(\mathcal{E}_1) = \mathrm{Int}\left[\frac{\mathrm{Re}\lambda_1}{\mathrm{Re}\lambda_1}\right] = 1. \tag{2.67}$$

$$\sigma_{\mathrm{out}}(\mathcal{E}_1) = \mathrm{Int}\left[\frac{\mathrm{Re}\bar{\lambda}_2}{\mathrm{Re}\lambda_1}\right] = 3, \tag{2.68}$$

The exact inner and outer non-resonance conditions, (2.9) and (2.13) respectively, again are satisfied for the spectral subspace $\mathcal{E}_1$, i.e., there exists a two-dimensional

	$\mathcal{E}_1$			
	a	b	λ_l	I
$\mathcal{O}(\lvert\mathbf{z}\rvert^3)$	3	0	λ_2	0.000162
	0	3	$\bar{\lambda}_2$	0.000162

Table 2.3: Near-outer-resonances for $\mathcal{E}_1$ with $\delta = 0.05$.

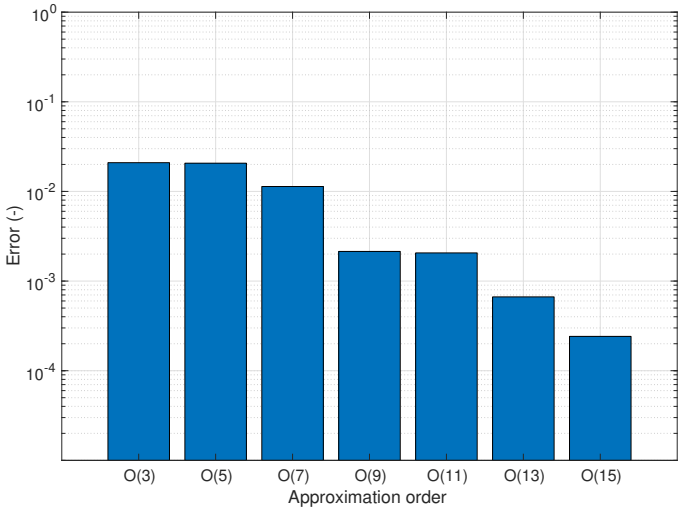

Figure 2.8: Invariance error for the 3^{th}-15^{th} order approximations of $\mathbf{W}(\mathcal{E}_1)$ for 50 evenly distributed initial positions lying on a fixed radius $\rho_0 = 0.28$ and $\theta_0 \in S^1$. For each trajectory traveling between ρ_0 and $\rho_\epsilon = 0.01$, we identify the maximum error and take the average over all trajectories.

analytic SSMs, $\mathbf{W}(\mathcal{E}_1)$, that is unique among all C^4 invariant manifolds tangent to $\mathcal{E}_1$. Due to the higher choice of damping, there are no near-inner resonances and hence the reduced dynamics on the manifold can be expressed as linear. However, the SSM is close to having two third-order outer resonances which in turn leads to the two near-outer resonances shown in table 2.3. For $k_2 = 4$ N m^{-1}, the SSM construction will break down as $\mathbf{\Theta}_3^{\mathcal{C}}$ becomes singular while equation (2.34) has a nonzero right-hand side.

As has been done in section 2.7.1, we would like to identify the order to which we have to approximate the SSM to obtain an accurate reduced order model. Using the invariance measure defined in equation (2.50), we test the invariance of $\mathbf{W}(\mathcal{E}_1)$ for different approximation orders. In figure 2.8, we show the invariance error for seven different approximations of $\mathbf{W}(\mathcal{E}_1)$. For a given fixed radius $\rho_0 = 0.28$ we take 50 initial points, each corresponding to an angle θ_0, uniformly distributed in S^1.

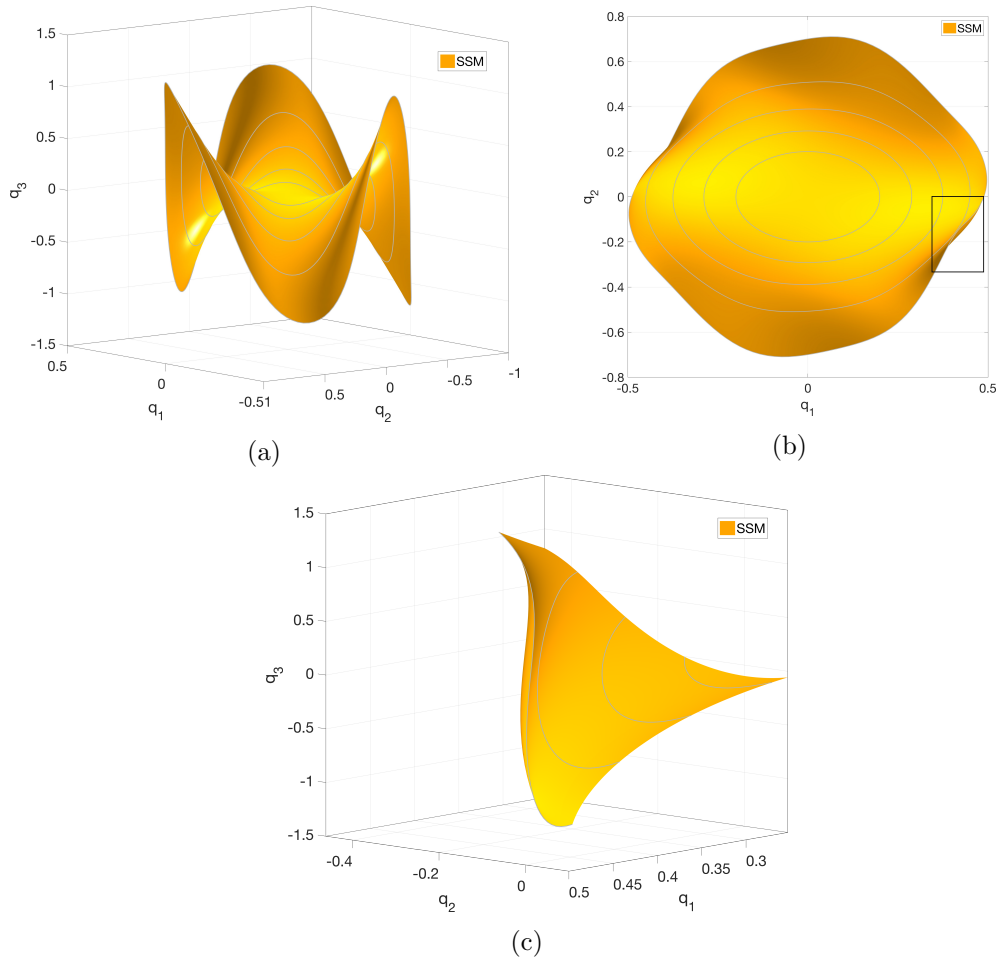

Figure 2.9: Lower-dimensional projections of the full phase space showing the 15^{th} order approximation of $\mathbf{W}(\mathcal{E}_1)$ in modal coordinates. Figures 2.9(a), 2.9(b) and 2.9(c) show the spectral submanifold $\mathbf{W}(\mathcal{E}_1)$ tangent to $\mathcal{E}_1$, being close to outer resonance. Figure 2.9(b), a top-view of $\mathbf{W}(\mathcal{E}_1)$, shows the development of a fold as indicated by the rectangle. Figure 2.9(c) is a zoomed-in version of the fold.

As a the SSM is near an outer resonance, a folding of the SSM over its underlying modal subspace is more likely to occur. Such a folding is illustrated in figure 2.9, showing a lower-dimensional projection of the full phase space of the 15^{th} order approximation of $\mathbf{W}(\mathcal{E}_1)$. This example brings out the power of the parameterization method, as constructing the SSM as a graph over its modal subspace would break down at the point of folding.

In figure 2.10, we show the SSM transformed to physical coordinates (also an option

Symbol	Meaning (unit)
L	Length of beam (mm)
h	Height of beam (mm)
b	Width of beam (mm)
ϱ	Density (kg mm^{-3})
E	Young's Modulus (MPa)
G	Shear Modulus (MPa)
η	Axial material damping constant (MPa s)
μ	Shear material damping constant (MPa s)
λ	External damping constant (MPa s mm^{-2})
$A = bh$	Cross-section of beam (mm^2)

Table 2.4: Notation used in subsequent derivations

in SSMtool), where we demonstrate the invariance of $\mathbf{W}(\mathcal{E}_1)$ (figure 2.10(a)) and that different trajectories converge towards $\mathbf{W}(\mathcal{E}_1)$ (figure 2.10(b)), when starting close to $\mathbf{W}(\mathcal{E}_1)$.

2.7.3 The discretized nonlinear Timoshenko beam

In this section, we construct a reduced order model for a discretized nonlinear Timoshenko beam by computing the reduced dynamics on the two-dimensional SSM arising from the slowest modal subspace. We will briefly outline the steps leading to the derivation of the partial differential equations (PDEs) governing the dynamics of the beam. Our reasoning largely follows the presentation given by Reddy [33]. The problem considered here is a square 2D beam placed in a cartesian coordinate system with coordinates (x, y, z) and basis $(\mathbf{e}_x, \mathbf{e}_y, \mathbf{e}_z)$. Initially, the beam is straight, with its main axis parallel to the x-axis, while its cross section lies in the $y-z$ plane. The relevant beam parameters are listed in table 2.4.

We call the line that initially coincides with the x-axis the beam's neutral axis. The kinematic assumptions underlying the Timoshenko beam model can be obtained by relaxing the restrictions of the Bernoulli hypothesis which is the basis of the more classical and well-known Euler-Bernoulli beam theory. The Bernoulli hypothesis states (cf. Reddy [33]) that initially straight material lines normal to the neutral axis remain (a) straight and (b) inextensible after deformation, and (c) rotate as rigid lines to remain perpendicular to the beam's neutral axis after deformation. We relax (c) by allowing for rigid rotation of the cross section about the y-axis. These kinematic assumptions are satisfied by the following displacement field

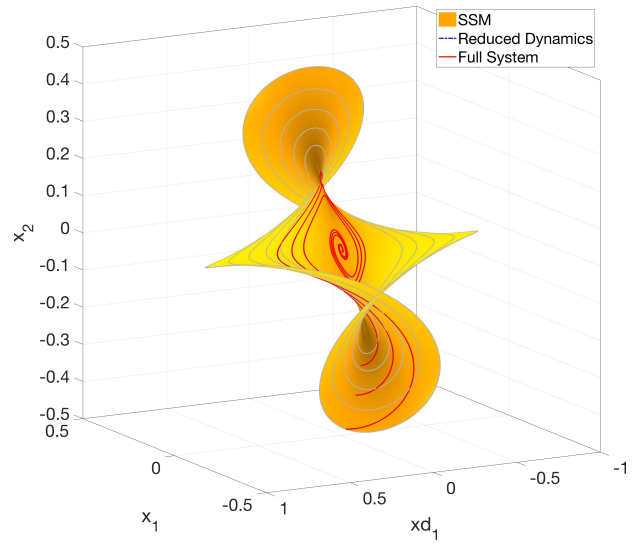

(a)

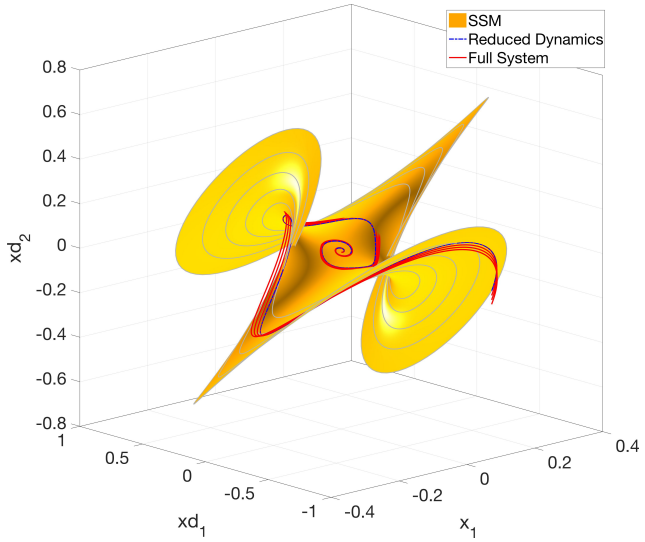

(b)

Figure 2.10: Lower-dimensional projections of the full phase space showing the 15^{th} order approximation of $\mathbf{W}(\mathcal{E}_1)$, transformed to physical coordinates. The dashed curves in figure 2.10(a) correspond to trajectories of the reduced system $\mathbf{R}(\mathbf{z})$ corresponding to the initial positions $\rho = \{0.15, 0.13, 0.11\}$ and $\theta = 3$. The solid curves represent trajectories of the full system for the same initial positions. In figure 2.10(b), the dashed curves corresponds to a trajectory of the reduced system $\mathbf{R}(\mathbf{z})$ for the initial position $\rho = 0.15$ and $\theta = 1$. The solid lines represent trajectories of the full system having an initial position off the manifold, showing the convergence towards $\mathbf{W}(\mathcal{E}_1)$.

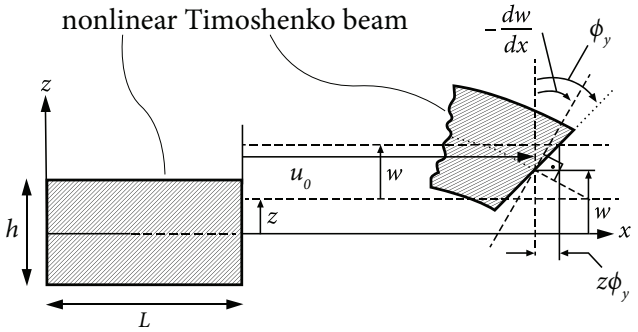

Figure 2.11: Kinematics of the nonlinear Timoshenko beam.

$$u_x(x, y, z) = u_0(x) + z\phi_y(x), \tag{2.69}$$
$$u_y(x, y, z) = 0, \tag{2.70}$$
$$u_z(x, y, z) = w(x). \tag{2.71}$$

Here (u_x, u_y, u_z) are the components of the displacement field $\mathbf{u}(x, y, z)$ for a material point in the (x, y, z) directions, respectively. The functions $u_0(x)$ and $w(x)$ represent the displacements of a material point with initial coordinates on the beam's neutral axis, given by $z = 0$. The rotation of a normal section about the y-axis is denoted by $\phi_y(x)$. We illustrate the kinematics in figure 2.11.

Following Reddy [33], we neglect all $(u_{0,x})^2$ terms in the Green-Lagrange strain tensor, where we use the shorthand notation $(\cdot)_{,x} = \partial_x(\cdot)$. This approximation accounts for geometric nonlinearities due to moderately large rotations while assuming small membrane strains. The relevant non-zero components of the simplified Green-Lagrange strain tensor ε_{ij} take the form

$$\varepsilon_{xx} = \varepsilon^0_{xx} + z\varepsilon^1_{xx}, \tag{2.72}$$
$$\gamma_{xz} = 2\varepsilon_{xy} = \gamma^0_{xz} + z\gamma^1_{xz}, \tag{2.73}$$

with

$$\varepsilon^0_{xx} = \partial_x u_0 + \frac{1}{2}(\partial_x w)^2,\ \varepsilon^1_{xx} = \partial_x \phi_y, \tag{2.74}$$
$$\gamma^0_{xz} = \phi_y + \partial_x w + \phi_y \partial_x u_0,\ \gamma^1_{xz} = \phi_y \partial_x \phi_y. \tag{2.75}$$

We assume a linear viscoelastic constitutive relation between the stresses and strains of the following form

$$\sigma_{xx} = E\varepsilon_{xx} + \eta\dot{\varepsilon}_{xx}, \tag{2.76}$$
$$\sigma_{xz} = G\gamma_{xz} + \mu\dot{\gamma}_{xz}. \tag{2.77}$$

Here σ_{xx} and σ_{xz} are the components of the Cauchy stress tensor $\boldsymbol{\sigma}$ (see, e.g., Lai et al. [34]). The relations given in (2.76) and (2.77) are a special case of the more general linear viscoelastic material models that can be found, for example, in Skrzypek and Ganczarski [35] and is also used, e.g., by Lesieutre and Kauffman [36]. We explain the derivation and discretization of the equations of motion of the beam in 2.B.

In the following computations, we will consider a beam that is clamped on one end and free on the other, which means that on the clamped end all displacements (u_0, w, ϕ_y) are zero, while on the free end no restrictions are placed on the displacements. After implementation of the essential boundary conditions, the number of degrees of freedom n of our system is given by

$$n = 5m + 1, \tag{2.78}$$

where m is the number of finite beam elements used in the discretization. Additionally, we set the external damping parameter c, discussed in 2.B, to zero and therefore the damping of our beam only enters through the viscoelastic constitutive relation.

We continue by constructing the slowest single-mode SSM for a specific beam, for which we will use the SSMtool to reduce the beam dynamics to a two-dimensional system of ordinary differential equations. The chosen geometric and material parameters are listed in Table 2.5.

We simulate the beam with three elements, resulting in a 32-dimensional phase space. For the chosen parameter values, the eigenvalues corresponding to the slowest modal subspace $\mathcal{E}$ are $\lambda_{1,2} = -0.02286 \pm 11.03\mathrm{i}$. In terms of its exponential decay rate, the eigenspace $\mathcal{E}$ is about 50 times slower compared to the second slowest eigenspace of the system. This spectral ratio indicates that trajectories of the system transverse to the slow SSM die out fast, making the slowest SSM an excellent choice for model reduction, because it will contain trajectories that remain active for the longest time.

In figure 2.12, we show the invariance error (2.50) for four different orders of approximations of $\mathbf{W}(\mathcal{E})$.

Parameter	Value
L	$1000\,\mathrm{mm}$
h	$100\,\mathrm{mm}$
b	$100\,\mathrm{mm}$
ϱ	$7850 \cdot 10^{-9}\,\mathrm{kg\ mm^{-3}}$
E	$90\,\mathrm{GPa}$
G	$34.6\,\mathrm{GPa}$
η	$33.6\,\mathrm{MPa\ s}$
μ	$20.9\,\mathrm{MPa\ s}$

Table 2.5: Geometric and material parameters.

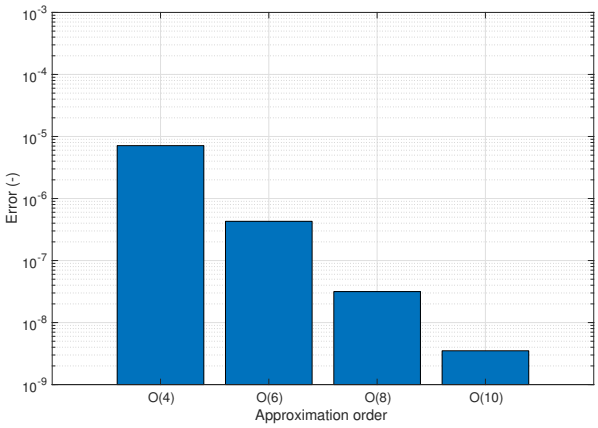

Figure 2.12: Invariance error for the 4^{th}, 6^{th}, 8^{th} and 10^{th} order approximations of $\mathbf{W}(\mathcal{E})$ for 50 evenly distributed initial positions lying on a fixed radius $\rho_0 = 1.5$ and $\theta_0 \in S^1$. The chosen value of $\rho_0 = 1.5$ corresponds to a maximum physical vertical displacement of the endpoint of the beam of 160 mm. For each trajectory traveling between ρ_0 and $\rho_\epsilon = 0.2$, we identify the maximum error and take the average over all trajectories.

We observe that the 4^{th} order approximation of $\mathbf{W}(\mathcal{E})$ is already accurate up to the chosen value of $\rho_0 = 1.5$, which corresponds to a maximum physical vertical displacement of the endpoint of the beam of 160 mm. By increasing the order of approximation to 10, the invariance error is reduced further by approximately three orders of magnitude. Figure 2.13 displays two lower-dimensional projections of the 32-dimensional phase space, showing the 10^{th} order approximation of $\mathbf{W}(\mathcal{E})$, with the the modal coordinates q_3 and q_4 plotted over the coordinates q_1 and q_2.

As λ_1 and $\bar{\lambda}_1$ have small negative real parts, the near-inner-resonances conditions related to $\mathcal{O}(|\mathbf{z}|^i)$ with $i = 3, 5, 7, 9$ are satisfied within the spectral subspaces $\mathcal{E}$. This in turn leads to the following expressions for reduced dynamics on $\mathbf{W}(\mathcal{E})$, obtained from SSMtool:

$$\begin{aligned}\dot{\rho} =& -0.022856\rho - 0.00017033\rho^3 - 4.9542 \cdot 10^{-6}\rho^5 \\ &+ 8.5365 \cdot 10^{-8}\rho^7 - 3.0348 \cdot 10^{-9}\rho^9, \end{aligned} \tag{2.79}$$

$$\begin{aligned}\omega =& 11.027 + 0.099097\rho^2 - 0.000020843\rho^4 - 2.8625 \cdot 10^{-6}\rho^6 \\ &+ 1.729 \cdot 10^{-7}\rho^8 \end{aligned} \tag{2.80}$$

Using the definition of the instantaneous amplitude (2.48) and the corresponding instantaneous frequency (2.80), SSMtool computes the parameterized backbone curve $\mathcal{B}$ (shown in figure 2.14) in less than 4 minutes time. The continuation curve, shown in black, has been computed using the numerical continuation software COCO [31], after applying a periodic force, $F = A \cos \omega t$, to the vertical displacement coordinate w at the free end of the beam with a forcing amplitude of $A = 300$ N.

The continuation algorithm takes 4 hours 42 minutes and 17 seconds to compute. Additionally, in figure 2.15 we show that trajectories starting off $\mathbf{W}(\mathcal{E}_1)$, will converge towards $\mathbf{W}(\mathcal{E}_1)$ as a consequence of having the high spectral quotient between the slowest and the remaining eigenspaces.

2.8 Conclusions

We have developed and tested an automated computational algorithm for two-dimensional autonomous SSMs that extends modal subspaces of linear systems to nonlinear systems. Implemented in the MATLAB package SSMtool, the algorithm can handle non-conservative mechanical systems of arbitrary (finite) degrees of freedom, subject to numerical memory limitations only. We used a systematic approach, the parameterization method, allowing us to construct the SSMs, their reduced dynamics and corresponding backbone curves up to any required order of precision.

Because the SSMs are embedded using the parameterization method, the construction of the SSMs does not break down when the SSM folds over its underlying

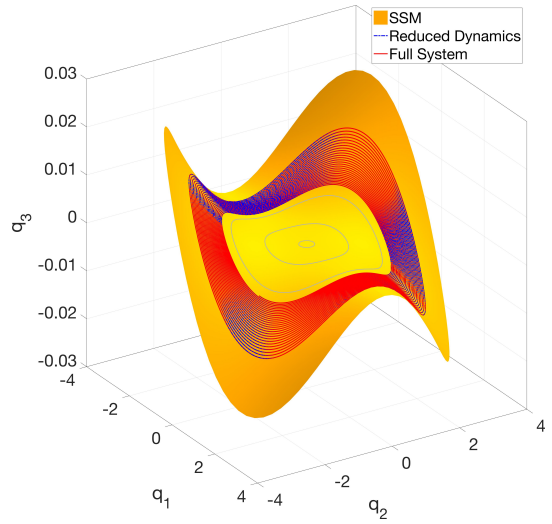

(a)

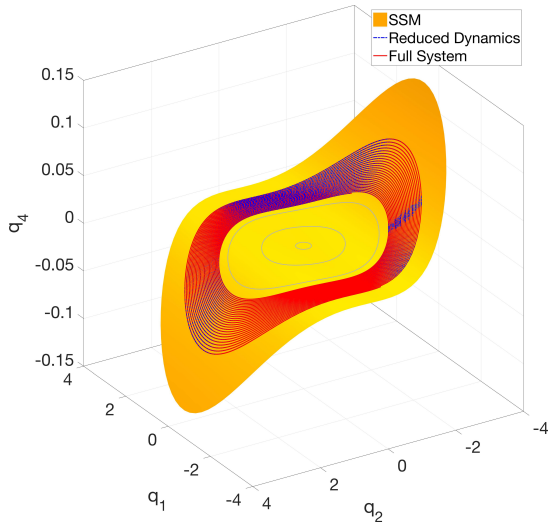

(b)

Figure 2.13: Lower-dimensional projections of the 32-dimensional phase space, of the discretized nonlinear Timoshenko beam, showing the 10^{th} order approximation of $\mathbf{W}(\mathcal{E})$. Figures 2.13(a), 2.13(b) show the spectral submanifold $\mathbf{W}(\mathcal{E})$ tangent to slowest modal subspace $\mathcal{E}$. The dashed curve corresponds to a trajectory of the reduced two-dimensional system $\mathbf{R}(z)$ corresponding to the initial positions $r = 1.5$ and $\theta = 3$. The solid curve represents a trajectory of the full system for the same initial position, with $t_{\text{end}} = 15$ s.

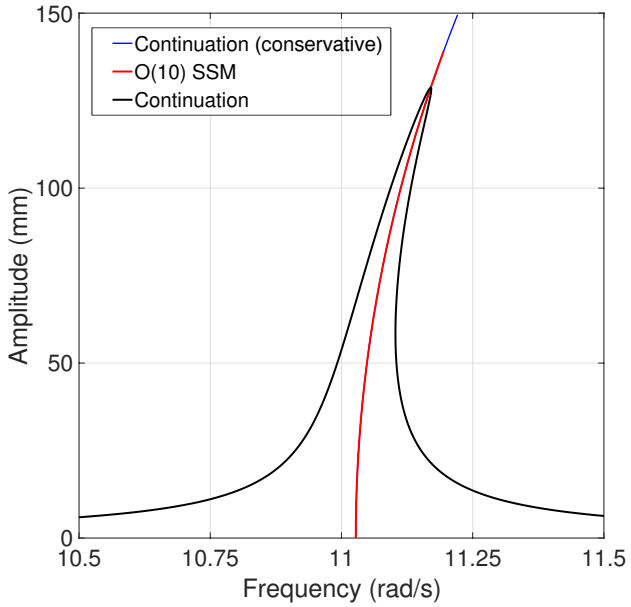

Figure 2.14: Backbone curve and periodically forced responses of the discretized Timoshenko beam having a 32-dimensional phase space. The $\mathcal{O}(10)$ (red) approximation of the backbone curve is computed up to $\rho = 1.3$. The black line corresponds to periodic orbits of the periodically forced system for varying forcing frequency. The blue line represents the backbone curve extracted from COCO in the conservative limit of the beam, without any forcing.

spectral subspace, as opposed to constructing the SSMs as graphs over a set of coordinates. The implementation (a MATLAB based graphical user interface called SSMtool) detects near-outer and near-inner resonances. In case of an exact outer resonance, the SSM construction will break down, whereas the presence of near-inner resonances in general leads to nonlinear terms in the reduced dynamics on the SSMs.

Szalai et al. [16] have exactly shown how backbone curves can be extracted from SSMs. We computed the backbone curves, in this fashion, up to 15^{th}-order for a two-degree-of-freedom non-conservative mechanical system and used the numerical continuation software COCO [31] to find periodic orbits of the periodically forced system for different forcing amplitudes while varying the forcing frequency to verify the accuracy of the backbone curves.

Under an approximate outer resonance, folding of the SSMs is likely to occur. We demonstrated such folding on the same two-degree-of-freedom non-conservative mechanical system by varying the system parameters accordingly to create a near-outer resonance.

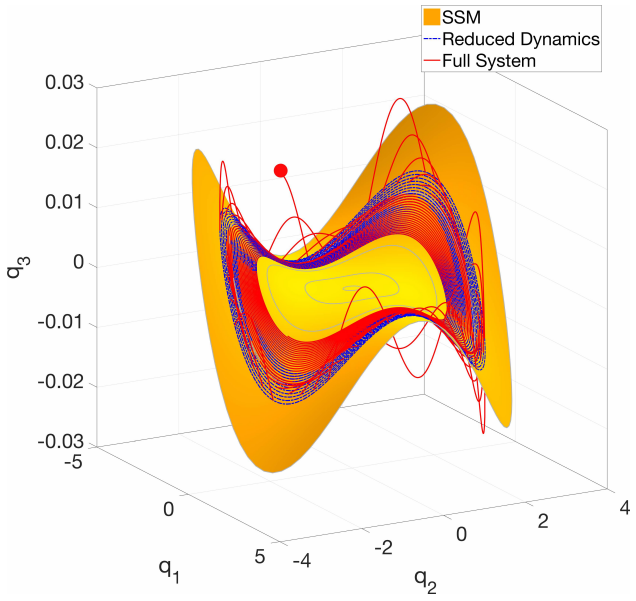

(a)

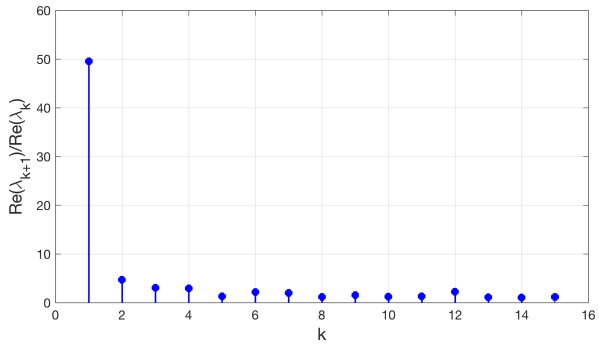

(b)

Figure 2.15: Lower-dimensional projections of the 32-dimensional phase space, of the discretized nonlinear Timoshenko beam, showing the 10^{th} order approximation of $\mathbf{W}(\mathcal{E})$. Figure 2.15(a) shows the spectral submanifold $\mathbf{W}(\mathcal{E})$ tangent to slowest subspace $\mathcal{E}$. The dashed (blue) curve corresponds to a trajectory of the reduced two-dimensional system $\mathbf{R}(\mathbf{z})$ corresponding to the initial positions $r = 1.5$ and $\theta = 3$. The solid (red) curve represents a trajectory of the full system having an initial position off the manifold, showing the convergence towards $\mathbf{W}(\mathcal{E}_1)$, with $t_{\text{end}} = 15$ s. The collapsing nature of the trajectories onto $\mathbf{W}(\mathcal{E})$, is a direct consequence of the high spectral ratio between the slowest eigenspace and the second slowest eigenspace shown in figure 2.15(b).

Finally, we have used the developed numerical method to construct a reduced-order model for a discretized nonlinear Timoshenko beam. We have computed the reduced dynamics on the two-dimensional slow SSM arising from the slowest modal subspace of the linearized system. The backbone curve obtained from the SSMtool shows close agreement with a single amplitude frequency sweep computed from COCO. While substantially limited in its scope relative to COCO's, SSMtool has returned backbone curves in a fraction of the times required by COCO to construct the response curve for one forcing amplitude. The spectral quotient between the slowest eigenspace and the second slowest eigenspace indicates that trajectories transverse to the slow SSM die out fast, making the slowest SSM an optimal choice for reducing our beam model to a two-dimensional system of ordinary differential equations.

Appendix

2.A Properties of the Kronecker product

In this section, we list several useful properties of the Kronecker product. For further reading, we refer the reader to A.J. Laub [28].

(i) The Kronecker product is associative, i.e.,

$$\begin{gathered}(\mathbf{A}\otimes\mathbf{B})\otimes\mathbf{C}=\mathbf{A}\otimes(\mathbf{B}\otimes\mathbf{C}),\\ \mathbf{A}\in\mathbb{C}^{m\times n},\quad \mathbf{B}\in\mathbb{C}^{p\times q},\quad \mathbf{C}\in\mathbb{C}^{r\times s}.\end{gathered}\tag{2.81}$$

(ii) The Kronecker product is right-distributive, i.e.,

$$\begin{gathered}(\mathbf{A}+\mathbf{B})\otimes\mathbf{C}=\mathbf{A}\otimes\mathbf{C}+\mathbf{B}\otimes\mathbf{C},\\ \mathbf{A},\mathbf{B}\in\mathbb{C}^{m\times n},\quad \mathbf{C}\in\mathbb{C}^{p\times q}.\end{gathered}\tag{2.82}$$

(iii) The Kronecker product is left-distributive, i.e.,

$$\begin{gathered}\mathbf{A}\otimes(\mathbf{B}+\mathbf{C})=\mathbf{A}\otimes\mathbf{B}+\mathbf{A}\otimes\mathbf{C},\\ \mathbf{A}\in\mathbb{C}^{m\times n},\quad \mathbf{B},\mathbf{C}\in\mathbb{C}^{p\times q}.\end{gathered}\tag{2.83}$$

(iv) The product of two Kronecker products yields another Kronecker product:

$$\begin{gathered}(\mathbf{A}\otimes\mathbf{B})(\mathbf{C}\otimes\mathbf{D})=\mathbf{AC}\otimes\mathbf{BD}\in\mathbb{C}^{mr\times pt},\\ \mathbf{A}\in\mathbb{C}^{m\times n},\quad \mathbf{B}\in\mathbb{C}^{r\times s},\quad \mathbf{C}\in\mathbb{C}^{n\times p},\quad \mathbf{D}\in\mathbb{C}^{s\times t}.\end{gathered}\tag{2.84}$$

2.B Equations of motion for the nonlinear Timoshenko beam

We derive the equations of motion for the nonlinear Timoshenko beam, based on the kinematical and constitutive assumptions made in section 2.7.3. Applying Hamilton's principle, we require that the true evolution of the displacement field between two specified time instances, t_1 and t_2, is a stationary point of the action functional S. Consequently, the variation of the action functional under a virtual displacement, of our system, should be identically zero at t_1 and t_2, i.e.,

$$\delta S = \int_{t_1}^{t_2} -\delta K + \delta U + \delta V \; dt = 0, \tag{2.85}$$

where δK and δU are the variations in kinetic and strain energy due to an arbitrary virtual displacement, and δV is the virtual work done by the external forces. For simplicity, we assume that the virtual work done by internal forces acting on the beam's cross section is large relative to the work done by internal forces due to out-of-plane stresses. This corresponds to assuming a state of either plane stress or plane strain, causing all terms related to out-of-plane stresses to drop out from the expression for the internal strain energy. This assumption can be justified by the fact that the respective neglected quantities would only contribute to the governing equations nonlinear terms of the fourth order in the stiffest (and hence typically the fastest decaying) degrees of freedom, ϕ_y, while all other nonlinearities are of order three or lower. Thus, those terms can be considered small compared to the rest. This can also be shown by nondimensionalizing the system and treating the ratio of the beam's length to its height, $\frac{h}{L}$, as a small parameter.

In addition to our viscoelastic constitutive law, we allow for external damping by introducing a simple damping model similar to the ones discussed in Lesieutre and Kauffman [36] and Lesieutre [37]. Our model assumes a body force acting proportional to the displacement velocity:

$$\mathbf{f}_c = c\dot{\mathbf{u}}(x, y, z). \tag{2.86}$$

The virtual work done by this force is

$$\delta V = \int_L \int_A \mathbf{f}_c \delta \mathbf{u} \; dA dx = \int_L \lambda(\dot{u}_0 \delta u_0 + \dot{w}\delta w + \frac{I_2}{I_0}\dot{\phi}_y \delta\phi_y) \; dx, \tag{2.87}$$

with

$$I_k = \int_A z^k dA, \quad \lambda = cI_0. \tag{2.88}$$

Equation (2.87) can be interpreted as the work done by two line-distributed forces, $f_x = \lambda \dot{u}_0$ and $f_z = \lambda \dot{w}$, proportional to the time derivative of the transverse displacement and the axial displacement, respectively. Additionally, we have a line-distributed force couple, $T_y = \lambda \frac{I_2}{I_0} \dot{\phi}_y$, proportional to the time derivative of the rotation of the cross section. The pre-factor I_2/I_0 in equation (2.87) ensures that the contribution of the external damping to the damping matrix of the FEM model derived below is proportional to the mass matrix. As a consequence, the entire system will be subjected to Rayleigh damping, a damping model which is frequently used in FEM simulations, see e.g. Takács et al. [38]. For more extensive discussions about how to model damping in beams, we refer the reader to the work of Lesieutre and Kauffman [36] and Lesieutre [37]. The preceding considerations lead to the following expressions

$$\delta K = \int_L m_0 \dot{u}_0 \delta \dot{u}_0 + m_0 \dot{w} \delta \dot{w} + m_2 \dot{\phi}_y \delta \dot{\phi}_y \, dx, \tag{2.89}$$

$$\delta U = \int_L \int_A \sigma_{xx} \delta \varepsilon_{xx} + \sigma_{xz} \delta \gamma_{xz} \, dA dx, \tag{2.90}$$

$$\delta V = \int_L f_x \delta u_0 + f_z \delta w + T_y \delta \phi_y \, dx, \tag{2.91}$$

with

$$m_k = \int_A \varrho z^k \, dA, \tag{2.92}$$

Substituting (2.89), (2.90) and (2.91) into (2.85), plugging in the kinematical assumptions and using integration by parts with respect to t and x we obtain

$$
\begin{aligned}
\delta S = \int_{t_1}^{t_2} \Bigg[\int_0^L \Bigg[& \Big(m_0 \ddot{u}_0 + \lambda \dot{u}_0 - \partial_x \left(M^0_{xx} + \phi_y M^0_{xz} \right) \Big) \delta u_0 \\
& + \Big(m_0 \ddot{w} + \lambda \dot{w} - \partial_x \left(M^0_{xz} + \partial_x w M^0_{xx} \right) \Big) \delta w \\
& + \Big(m_2 \ddot{\phi}_y + \lambda \frac{I_2}{I_0} \dot{\phi}_y - \partial_x \left(M^1_{xx} + \phi_y M^1_{xz} \right) \\
& + \left(M^0_{xz} + \partial_x u_0 M^0_{xz} + \partial_x \phi_y M^1_{xz} \right) \Big) \delta \phi_y \Bigg] dx \\
& + \left[\left(M^0_{xx} + \phi_y M^0_{xz} \right) \delta u_0 \right]_0^L + \left[\left(M^0_{xz} + \partial_x w M^0_{xx} \right) \delta w \right]_0^L \\
& + \left[\left(M^1_{xx} + \phi_y M^1_{xz} \right) \delta \phi_y \right]_0^L \Bigg] dt = 0,
\end{aligned}
\tag{2.93}
$$

where we have defined

$$
M^k_{ij} = \int_A \sigma_{ij} z^k \, dA. \tag{2.94}
$$

Equating the variational derivative of this functional with zero, we obtain the Euler-Lagrange equations

$$
m_0 \ddot{u}_0 + \lambda \dot{u}_0 - \partial_x \left(M^0_{xx} + \phi_y M^0_{xz} \right) = 0, \tag{2.95}
$$

$$
m_0 \ddot{w} + \lambda \dot{w} - \partial_x \left(M^0_{xz} + \partial_x w M^0_{xx} \right) = 0, \tag{2.96}
$$

$$
\begin{aligned}
& m_2 \ddot{\phi}_y + \lambda \frac{I_2}{I_0} \dot{\phi}_y - \partial_x \left(M^1_{xx} + \phi_y M^1_{xz} \right) \\
& + \left(M^0_{xz} + \partial_x u_0 M^0_{xz} + \partial_x \phi_y M^1_{xz} \right) = 0,
\end{aligned}
\tag{2.97}
$$

along with the corresponding boundary conditions

$$
\begin{aligned}
\left(M^0_{xx} + \phi_y M^0_{xz} \right)\big|_L \delta u_0(L) = 0, \quad & \left(M^0_{xx} + \phi_y M^0_{xz} \right)\big|_0 \delta u_0(0) = 0, \\
\left(M^0_{xz} + \partial_x w M^0_{xx} \right)\big|_L \delta w(L) = 0, \quad & \left(M^0_{xz} + \partial_x w M^0_{xx} \right)\big|_0 \delta w(0) = 0, \\
\left(M^1_{xx} + \phi_y M^1_{xz} \right)\big|_L \delta \phi_y(L) = 0, \quad & \left(M^1_{xx} + \phi_y M^1_{xz} \right)\big|_0 \delta \phi_y(0) = 0.
\end{aligned}
$$

The M^k_{ij} terms can be written as a function of our displacement field by using the kinematical and constitutive relations, i.e.,

$$
\begin{aligned}
M^0_{xx} &= I_0 \left(E(\partial_x u_0 + \frac{1}{2}(\partial_x w)^2) + \eta(\partial_x \dot{u}_0 + \partial_x \dot{w} \partial_x w) \right), \\
M^1_{xx} &= I_2 \left(E\partial_x \phi_y + \eta \partial_x \dot{\phi}_y \right), \\
M^0_{xz} &= I_0 \left(G(\phi_y + \partial_x w + \phi_y \partial_x u_0) + \mu(\dot{\phi}_y + \partial_x \dot{w} + \dot{\phi}_y \partial_x u_0 + \phi_y \partial_x \dot{u}_0) \right), \\
M^1_{xz} &= I_2 \left(G\phi_y \partial_x \phi_y + \mu(\dot{\phi}_y \partial_x \phi_y + \phi_y \partial_x \dot{\phi}_y) \right).
\end{aligned}
$$

We discretize equations (2.95)-(2.97) using a finite-element discretization (cf. Reddy [39] for a more detailed description). We use cubic shape functions to approximate u_0, quadratic shape functions for w and linear shape functions for ϕ_y. A beam element with three equally spaced nodes, situated at the beginning, the middle and at the end of the element is used. The node in the middle of the element is only needed for the interpolation of the transverse displacement w. To avoid shear and membrane locking, the ε^0_{xx} and γ^0_{xz} terms should be approximated by shape functions of the same order. After discretization, we obtain a set of n ordinary differential equations (ODEs) governing the dynamics the nonlinear Timoshenko beam:

$$
\mathbf{M}\ddot{\mathbf{y}} + \mathbf{C}\dot{\mathbf{y}} + \mathbf{K}\mathbf{y} + \mathbf{f}(\mathbf{y}, \dot{\mathbf{y}}) = \mathbf{0} \tag{2.98}
$$

where we have defined the vector

$$
\mathbf{y} = \begin{bmatrix} \tilde{u}_0 \\ \tilde{w} \\ \tilde{\phi}_y \end{bmatrix} \tag{2.99}
$$

representing the discretized degrees of freedom corresponding to the unknowns (u_0, w, ϕ_y). The quantities $\mathbf{M} \in \mathbb{R}^{n \times n}$, $\mathbf{C} \in \mathbb{R}^{n \times n}$, $\mathbf{K} \in \mathbb{R}^{n \times n}$ are the mass, damping and stiffness matrices of our discretized model, respectively, and the nonlinear force vector $\mathbf{f} \in \mathbb{R}^n$ is of the form

$$
f_i = D_{ijk} y_j y_k + G_{ijk} y_j \dot{y}_k + H_{ijkl} y_j y_k y_l + L_{ijkl} y_j y_k \dot{y}_l \tag{2.100}
$$

where $i \in \{1, \ldots, n\}$, and the Einstein summation convention is followed.

2.C Multiple representations for the nonlinear coefficient matrices

The vector $\mathbf{q}^{\otimes i}$ contains all possible combinations of its own elements up to order i, and therefore will contain all the monomial terms related to a homogeneous multivariate polynomial of degree i in the variables $\mathbf{q}$. The number of unique monomial terms $S(2n, i)$ in a multivariate polynomial of degree i with the variables $\mathbf{q} \in \mathbb{C}^{2n}$ is equal to the number of multisets of cardinality i, with elements taken from the set $\{1, 2, \ldots, 2n\} \in \mathbb{N}^{2n}$ [40], i.e,

$$S(2n, i) = \left(\begin{array}{c} i + 2n - 1 \\ i \end{array} \right) = \frac{(i + 2n - 1)!}{(2n - 1)!i!}. \tag{2.101}$$

To illustrate this, we now give an example.

Example 2.4 [Unique monomial terms representing a multivariate polynomial of degree two] Assume that $\mathbf{q} = (q_1, q_2, q_3, q_4)^T \in \mathbb{C}^4$, then the unique monomial terms related to the multivariate polynomial of degree two in the $\mathbf{q}$ variables are

$$\left(\begin{array}{c} q_1^2 \\ q_1 q_2 \\ q_1 q_3 \\ q_1 q_4 \\ q_2^2 \\ q_2 q_3 \\ q_2 q_4 \\ q_3^2 \\ q_3 q_4 \\ q_4 \end{array} \right) \rightarrow \left. \begin{array}{c} \{1,1\} \\ \{1,2\} \\ \{1,3\} \\ \{1,4\} \\ \{2,2\} \\ \{2,3\} \\ \{2,4\} \\ \{3,3\} \\ \{3,4\} \\ \{4,4\} \end{array} \right\} \quad S = \left(\begin{array}{c} 5 \\ 2 \end{array} \right) = 10. \tag{2.102}$$

Here we see the equivalence with the ten multisets of cardinality two, with elements taken from the set $\{1, 2, 3, 4\}$. Indeed, the Kronecker product $\mathbf{q} \otimes \mathbf{q}$ will result in a 16-dimensional vector containing 6 extra cross terms that are contained in the ten multisets.

As a direct consequence of this redundancy for a representation of $2n$ multivariate polynomials of degree i in the variables $\mathbf{q}$, there will be infinitely many possible representations for the nonlinear coefficient matrix $\mathbf{G}_i$ corresponding to the i^{th} order in equation (4.5). We show this in Example 2.5.

Example 2.5 [Multiple representations for the matrices $\mathbf{G}_i$] If we assume, for simplicity, that $\mathbf{q} = (q_1, q_2)^T \in \mathbb{C}^2$, and $\mathbf{G}(\mathbf{q})$ is only of $\mathcal{O}\left(|\mathbf{q}|^2\right)$, i.e. $\Gamma = 2$,

$$\mathbf{G}(\mathbf{q}) = \sum_{i=2}^{2} \mathbf{G}_i \mathbf{q}^{\otimes i} = \mathbf{G}_2 \mathbf{q} \otimes \mathbf{q} = \begin{bmatrix} g_{11} & g_{12} & g_{13} & g_{14} \\ g_{21} & g_{22} & g_{23} & g_{24} \end{bmatrix} \begin{bmatrix} q_1^2 \\ q_1 q_2 \\ q_2 q_1 \\ q_2^2 \end{bmatrix} \tag{2.103}$$
$$= \begin{bmatrix} g_{11} q_1^2 + (g_{12} + g_{13}) q_1 q_2 + g_{14} q_2^2 \\ g_{21} q_1^2 + (g_{22} + g_{23}) q_1 q_2 + g_{24} q_2^2 \end{bmatrix}.$$

Assume that the quadratic nonlinearities of the underlying system are modeled as follows

$$\mathbf{P}(\mathbf{q}) = \begin{bmatrix} a_1 q_1^2 + b_1 q_1 q_2 + c_1 q_2^2 \\ a_2 q_1^2 + b_2 q_1 q_2 + c_2 q_2^2 \end{bmatrix}. \tag{2.104}$$

If we want to transform $\mathbf{P}(\mathbf{q})$ into the form of $\mathbf{G}(\mathbf{q})$, equating $\mathbf{G}(\mathbf{q})$ and $\mathbf{P}(\mathbf{q})$ and collecting terms of equal power in q_1 and q_2 gives

$$\begin{aligned} g_{11} &= a_1, \quad (g_{12} + g_{13}) = b_1, \quad g_{14} = c_1, \\ g_{21} &= a_2, \quad (g_{22} + g_{23}) = b_2, \quad g_{24} = c_2. \end{aligned}$$

The presence of the redundant term $q_2 q_1$ in $\mathbf{q} \otimes \mathbf{q}$ introduces two extra coefficients g_{13} and g_{23}, giving us the freedom to introduce a constraint between g_{12} and g_{13}, and between g_{22} and g_{23}. We then have two independent equations, each containing two independent variables. For each equation, an independent constraint can be introduced such that g_{12}, g_{13}, g_{22} and g_{23} are uniquely determined and the product $\mathbf{G}_2 \mathbf{q} \otimes \mathbf{q} = \mathbf{G}(\mathbf{q})$ precisely represents $\mathbf{P}(\mathbf{q})$. Each monomial term in the vector $\mathbf{q}^{\otimes i}$ has a unique location in the vector itself, which in turn points to a unique location in the matrix $\mathbf{G}_i$ for each row. In this way, the constraints are automatically satisfied when SSMtool identifies the nonlinearities of the underlying mechanical system.

2.D Memory requirements for the coefficient matrices

In our current setting, the most computationally demanding terms in the SSM construction are the summation terms in equation (2.31), which are shown below for the i^{th} order

$$\sum_{m=2}^{i-1} \mathbf{W}_m \sum_{|\mathbf{p}|=1} \mathbf{R}_{i+1-m}^{p_1} \otimes \ldots \otimes \mathbf{R}_{i+1-m}^{p_m}, \tag{2.105}$$

$$\sum_{m=2}^{i-1} \mathbf{G}_m \sum_{|\mathbf{r}|=i} \mathbf{W}_{r_1} \otimes \ldots \otimes \mathbf{W}_{r_m}. \tag{2.106}$$

If we assume that all matrices in equations (2.105) and (2.106) are densely filled with doubles, where each double has an allocated memory of 8 bytes in MATLAB, the total amount of memory needed (in bytes) to store the matrices in equations (2.105) and (2.106) corresponding to a mechanical system of n degrees of freedom at the i^{th} order is equal to

$$M(n,i) = 8 \cdot \sum_{m=2}^{i-1} \left((2n)2^m + 2^{m+i}m + (2n)^{m+1} + (2n)^m 2^i c(m,i) \right), \tag{2.107}$$

where $c(m,i)$ is the number of all possible combinations of m positive integers $l_1, \ldots, l_m \in \mathbb{N}^+$, with $|\mathbf{l}| = i$.

Example 2.6 [Memory requirements for different orders] We consider a mechanical system of two degrees of freedom ($n = 2$) with a single cubic nonlinearity and arbitrary near-inner-resonances. The cubic nonlinear spring will only contribute to the $\mathbf{G}_3$ coefficient matrix, therefore the only contribution from equation (2.106) to equation (2.107) is for $m = 3$. In figure 2.D.1, we show the output of equation (2.107) for different orders of expansion.

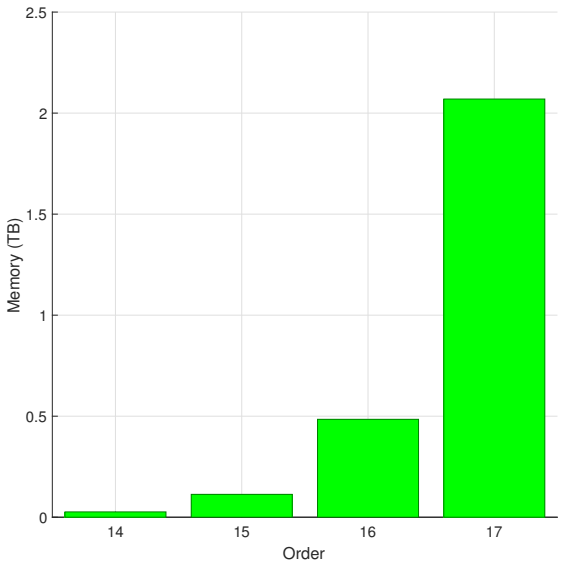

Figure 2.D.1: Memory requirements in terabytes for equations (2.105) and (2.106) for different orders of the two-degree-of-freedom mechanical system. The amount of memory needed drastically increases from 0.4846 TB for order 16 to 2.0696 TB for order 17.

Chapter 3

Non-autonomous SSMs

Chapter Summary

In this chapter, we show how spectral submanifold (SSM) theory can be used to extract forced-response curves, including isolas, without any numerical simulation in high-degree-of-freedom, periodically forced mechanical systems. We use multivariate recurrence relations to construct the SSMs, achieving a major speed-up relative to earlier autonomous SSM algorithms. The increase in computational efficiency promises to close the current gap between studying lower-dimensional academic examples and analyzing larger systems obtained from finite-element modeling, as we illustrate on a discretization of a damped-forced beam model.

3.1 Introduction

Determining the forced response curve (FRC) of a multi-degree-of-freedom nonlinear mechanical system under periodic forcing is one of the most common tasks in structural engineering, providing key insights into the nonlinear behavior of the system. Specifically, the FRC gives the amplitude of the periodic response of the system as a function of the frequency of the periodic forcing. This, in turn, provides valuable information about expected material stresses and strains that arise in the system under various external forcing conditions. The nonlinear FRC often differs significantly from the FRC of the linear part of the system, possibly containing also unexpected isolated response branches (isolas).

For low-dimensional mechanical systems, the steady-state response can simply be obtained by numerically integrating the equations of motion. However, mechanical models constructed by finite-element packages generally contain thousands of degrees of freedom. This high dimensionality, coupled with typically low damping and costly function evaluations, may result in excessively long integration times (up to days or weeks) until a steady-state response is reached.

To overcome this obstacle, one often reduces high-dimensional systems to lower-dimensional models whose FRCs can be faster extracted. Virtually all model-

reduction techniques in use involve projecting the full dynamics to a lower-dimensional subspace. Examples include the static condensation method, also known as the Guyan-Irons reduction method (Guyan [41] and Irons [42]; cf. Géradin and Rixen [29]), the Craig-Bampton method [43] and the proper orthogonal decomposition method [44, 45, 46, 47, 48]. These methods are generally applied without any a priori knowledge about the errors arising from the lack of invariance of the subspace involved in the projection. Similarly unclear is the error arising from the nonlinear method of modal derivatives [49], which formally restricts the full system into an envisioned quadratic surface in the configuration space. Haller and Ponsioen [50] showed that only under restrictive conditions can the static-condensation and modal-derivative techniques be justified as first- and second-order local approximations to an invariant manifold to which the full mechanical system can indeed be exactly reduced.

A more recent reduction method, proposed by Haller and Ponsioen [4], uses spectral submanifold (SSM) theory to reduce the full dynamics to exactly invariant SSM surfaces in the phase space. SSMs are the unique, smoothest, nonlinear continuations of spectral subspaces of the linearized, unforced limit of a mechanical system. SSM theory can be applied to nonlinear, damped mechanical systems with no forcing, periodic forcing or quasi-periodic forcing. As shown by [6, 8, 9, 16, 51, 52], the reduced dynamics on a two-dimensional SSM serves as an exact, one-degree-of-freedom reduced-order model, that can be constructed for any particular vibration mode of interest.

Once a reduced model has been obtained by any method, it is typically interrogated for a reduced forced response. A broadly used method for this analysis is the harmonic balance (HB) method, introduced first by Kryloff and Bogoliuboff [53] for a single-harmonic approximation. The HB method assumes that the system has a steady-state periodic solution, which can therefore be represented by a Fourier series. By substituting the assumed solution into the original ordinary differential equations and keeping only finitely many harmonics, one obtains a set of nonlinear algebraic equations for the unknown Fourier coefficients. The HB method can also be coupled to a continuation scheme in order to obtain the forced response over a forcing frequency domain of interest (cf. von Groll and Ewins [54] and Cochelin and Vergez [55]). While conceptually simple, the HB method also has several shortcomings. First, it requires a large number of nonlinear algebraic equations to be solved, and hence becomes ineffective in higher degrees of freedom. Second, the solvability of these equations for a few harmonics does not imply that a periodic orbit actually exists. Indeed, there are documented examples of systems, such as those with quadratic nonlinearities, for which the HB has been found not to work well [56]. More recently, Breunung and Haller [57] constructed mechanical examples in which the HB method indicates the existence of a periodic response even though no periodic orbits exist in the system. Finally, the HB method provides no

information about the stability of the periodic orbit that it approximates.

As alternatives to the HB method, several computational methods exist in the time domain for finding periodic solutions. Among these, the shooting method (cf. Peeters et al. [12], Slater [58], Roberts and Shipman [59]) solves a two-point boundary value problem to compute a steady-state solution of a periodically forced system. An initial guess, representing an initial position on the periodic orbit, is corrected by solving the equation of variations, which can be evaluated using a numerical finite-difference method by perturbing each of the initial conditions and integrating the full system. Similar to the HB method, the shooting method can be coupled to a path continuation technique to obtain the forced response curve.

To avoid numerical integration of the full system, a collocation method can be used to solve for the full periodic solution at once. This is done by approximating a periodic solution of the full system as a continuous function of time, expressed on a predefined number of time intervals as a polynomial of a certain degree, parameterized by unknown base points (see Dankowicz and Schilder [31]). Collocation methods, however, have generally not been applied to large systems due to their significant memory needs.

In the recent work of Jain et al. [60], an integral-equation approach is proposed for the fast computation of the steady-state response of (quasi-) periodically forced nonlinear systems by finding the zeros of an integral equation using a Picard and Newton–Raphson iteration method. A major advantage of this approach compared to the classical shooting method is its ability to handle quasi-periodic forcing. The integral equation approach also gives increased speed over other numerical continuation methods by exploiting the special structure of weakly nonlinear mechanical vibrations. Still, for higher degrees of freedom, even this increased speed can lead to calculations that are simply too big to be practical.

In contrast to all these prior approaches, here we use the reduced dynamics on a two-dimensional SSM to extract the forced-response curve around a particular mode of interest. By doing so, we extend the work of Ponsioen et al. [6], who developed a MATLAB-based computational tool (SSMtool) for computing two-dimensional SSMs in arbitrary autonomous mechanical systems, to the non-autonomous setting. The present work also builds on the approach of Breunung and Haller [8], who compute the non-autonomous part of the SSM up to zeroth order in appropriate coordinates in which the SSM-reduced dynamics simplifies to a normal form.

The reduced dynamics on each two-dimensional SSM provides us with two differential equations. The fixed points of the two-dimensional SSM-reduced system correspond to periodic orbits on the FRC for a particular forcing frequency. These fixed points can be instantaneously computed, irrespective of the dimensionality of the original mechanical system. The stability of the corresponding periodic orbits can directly be obtained from the eigenvalues of the linearized reduced system at

its fixed points. As a consequence, all periodic responses, including isolas, and their stability can be identified from a procedure in which the only numerical step in the end is the identification of the zeros of a two-dimensional autonomous vector field. A simple MATLAB implementation is now available for this procedure[1], allowing the user to apply SSM-based model reduction and forced-response calculations to systems with high degrees of freedom. We illustrate this by locating forced responses in a forced-damped beam, considering discretizations of this nonlinear system up to 10,000 degrees of freedom. We also present speed comparisons with the collocation and the HB methods up to the limits of applicability of those methods.

3.2 System set-up

We consider n-degree-of-freedom, periodically forced mechanical systems of the form

$$\begin{gathered}\mathbf{M}\ddot{\mathbf{y}}+\mathbf{C}\dot{\mathbf{y}}+\mathbf{K}\mathbf{y}+\mathbf{g}(\mathbf{y},\dot{\mathbf{y}})=\varepsilon\mathbf{f}(\Omega t),\quad 0\leq\varepsilon\ll 1,\\ \mathbf{g}(\mathbf{y},\dot{\mathbf{y}})=\mathcal{O}\left(|\mathbf{y}|^2,|\mathbf{y}|\,|\dot{\mathbf{y}}|,|\dot{\mathbf{y}}|^2\right),\end{gathered}\tag{3.1}$$

where $\mathbf{y}\in\mathbb{R}^n$ is the generalized position vector; $\mathbf{M}=\mathbf{M}^T\in\mathbb{R}^{n\times n}$ is the positive definite mass matrix; $\mathbf{C}=\mathbf{C}^T\in\mathbb{R}^{n\times n}$ is the damping matrix; $\mathbf{K}=\mathbf{K}^T\in\mathbb{R}^{n\times n}$ is the stiffness matrix and $\mathbf{g}(\mathbf{y},\dot{\mathbf{y}})$ contains all the nonlinear terms in the system, which are assumed to be analytic. The external forcing $\varepsilon\mathbf{f}(\Omega t)$ does not depend on the positions and velocities.

We transform system (3.1) into a set of $2n$ first-order ordinary differential equations by introducing the change of variables $\mathbf{x}_1=\mathbf{y}$, $\mathbf{x}_2=\dot{\mathbf{y}}$, with $\mathbf{x}=(\mathbf{x}_1,\mathbf{x}_2)\in\mathbb{R}^{2n}$, which gives

$$\begin{aligned}\dot{\mathbf{x}}&=\begin{pmatrix}\mathbf{0}&\mathbf{I}\\-\mathbf{M}^{-1}\mathbf{K}&-\mathbf{M}^{-1}\mathbf{C}\end{pmatrix}\mathbf{x}+\begin{pmatrix}\mathbf{0}\\-\mathbf{M}^{-1}\mathbf{g}(\mathbf{x}_1,\mathbf{x}_2)\end{pmatrix}\\&+\varepsilon\begin{pmatrix}\mathbf{0}\\\mathbf{M}^{-1}\mathbf{f}(\Omega t)\end{pmatrix}=\mathbf{A}\mathbf{x}+\mathbf{G}_{\mathrm{p}}(\mathbf{x})+\varepsilon\mathbf{F}_{\mathrm{p}}(\Omega t).\end{aligned}\tag{3.2}$$

System (3.2) has a fixed point at $\mathbf{x}=\mathbf{0}$ when the system is unforced ($\varepsilon=0$). Additionally we observe that $\mathbf{M}^{-1}$ is well-defined because $\mathbf{M}$ is assumed positive definite.

The linearized part of system (3.2) is

$$\dot{\mathbf{x}}=\mathbf{A}\mathbf{x},\tag{3.3}$$

where the matrix $\mathbf{A}$ has $2n$ eigenvalues $\lambda_k\in\mathbb{C}$ for $k=1,\ldots,2n$. Counting multiplicities, we sort these eigenvalues based on their real parts in the decreasing order

[1] SSMtool is available at: `www.georgehaller.com`.

$$\mathrm{Re}(\lambda_{2n}) \leq \mathrm{Re}(\lambda_{2n-1}) \leq \ldots \leq \mathrm{Re}(\lambda_1) < 0, \tag{3.4}$$

assuming that the real part of each eigenvalue is less than zero and hence the fixed point of Eq. (3.3) is asymptotically stable. We further assume that the constant matrix $\mathbf{A}$ is semisimple. Similarly to section 2.2, we can, therefore, identify $2n$ linearly independent eigenvectors $\mathbf{v}_k \in \mathbb{C}^{2n}$, with $k = 1, \ldots, 2n$, each spanning a real eigenspace $E_k \subset \mathbb{R}^{2n}$ with $\dim(E_k) = 2 \times \mathrm{alg}(\lambda_k)$ in case $\mathrm{Im}(\lambda_k) \neq 0$, or $\dim(E_k) = \mathrm{alg}(\lambda_k)$ in case $\mathrm{Im}(\lambda_k) = 0$.

3.3 Non-autonomous SSMs for continuous mechanical systems

As a result of $\mathbf{A}$ being semisimple, the linear part of system (3.2) is diagonalized by a linear change of coordinates $\mathbf{x} = \mathbf{T}\mathbf{q}$, with $\mathbf{T} = [\mathbf{v}_1, \mathbf{v}_2, \ldots, \mathbf{v}_{2n}] \in \mathbb{C}^{2n\times 2n}$ and $\mathbf{q} \in \mathbb{C}^{2n}$, yielding

$$\dot{\mathbf{q}} = \underbrace{\mathrm{diag}(\lambda_1, \lambda_2 \ldots, \lambda_{2n})}_{\mathbf{\Lambda}} \mathbf{q} + \mathbf{G}_{\mathrm{m}}(\mathbf{q}) + \varepsilon \mathbf{F}_{\mathrm{m}}(\phi). \tag{3.5}$$

We consider the two-dimensional modal subspace $\mathcal{E} = \mathrm{span}\{\mathbf{v}_1, \mathbf{v}_2\} \subset \mathbb{C}^{2n}$ with $\mathbf{v}_2 = \bar{\mathbf{v}}_1$. The remaining linearly independent eigenvectors $\mathbf{v}_3, \ldots, \mathbf{v}_{2n}$ span a complex subspace $\mathcal{C} \subset \mathbb{C}^{2n}$ such that the full phase space of (3.5) can be expressed as the direct sum

$$\mathbb{C}^{2n} = \mathcal{E} \oplus \mathcal{C}. \tag{3.6}$$

We write the diagonal matrix $\mathbf{\Lambda}$ as

$$\mathbf{\Lambda} = \begin{bmatrix} \mathbf{\Lambda}_{\mathcal{E}} & 0 \\ 0 & \mathbf{\Lambda}_{\mathcal{C}} \end{bmatrix}, \tag{3.7}$$
$$\mathrm{Spect}\,(\mathbf{\Lambda}_{\mathcal{E}}) = \{\lambda_1, \lambda_2\}, \quad \mathrm{Spect}\,(\mathbf{\Lambda}_{\mathcal{C}}) = \{\lambda_3, \ldots, \lambda_{2n}\},$$

with $\mathbf{\Lambda}_{\mathcal{E}} = \mathrm{diag}(\lambda_1, \lambda_2)$ and $\mathbf{\Lambda}_{\mathcal{C}} = \mathrm{diag}(\lambda_3, \ldots, \lambda_{2n})$.

Following Haller and Ponsioen [4], we now define a *non-autonomous spectral submanifold* (SSM), $\mathcal{W}(\mathcal{E}, \Omega t)$, corresponding to the spectral subspace $\mathcal{E}$ of $\mathbf{\Lambda}$ as a two-dimensional invariant manifold of the dynamical system (3.5) that is $\frac{2\pi}{\Omega}$-periodic in time and

(i) Perturbs smoothly from $\mathcal{E}$ at the trivial fixed point $\mathbf{q} = \mathbf{0}$ under the addition of the $\mathcal{O}(\varepsilon)$ terms in Eq. (3.5).

(ii) Is strictly smoother than any other $\frac{2\pi}{\Omega}$-periodic invariant manifold satisfying (i).

We also define the *absolute spectral quotient* $\Sigma(\mathcal{E})$ of $\mathcal{E}$ as the positive integer

$$\Sigma(\mathcal{E}) = \text{Int}\left[\frac{\min_{\lambda\in\text{Spect}(\mathbf{\Lambda})}\text{Re}\lambda}{\max_{\lambda\in\text{Spect}(\mathbf{\Lambda}_\mathcal{E})}\text{Re}\lambda}\right] \in \mathbb{N}. \tag{3.8}$$

Additionally, we introduce the non-resonance conditions

$$\begin{aligned} a\text{Re}\lambda_1 + b\text{Re}\lambda_2 \neq \text{Re}\lambda_l, \quad \forall\lambda_l \in \text{Spect}(\mathbf{\Lambda}_\mathcal{C}), \\ 2 \leq a+b \leq \Sigma(\mathcal{E}), \quad a,b \in \mathbb{N}_0. \end{aligned} \tag{3.9}$$

We now restate the following result from Haller and Ponsioen [4], for the existence of an SMM in system (3.5).

Theorem 3.1 *Under the non-resonance conditions (3.9), the following hold for system (3.5):*

(i) There exists a unique two-dimensional, time-periodic, analytic SSM, $\mathcal{W}(\mathcal{E},\Omega t)$ that depends smoothly on the parameter ε.

(ii) $\mathcal{W}(\mathcal{E})$ can be viewed as an embedding of an open set $\mathcal{U}$ into the phase space of system (3.5) via the map

$$\mathbf{W}(\mathbf{s},\phi) : \mathcal{U} \subset \mathbb{C}^2 \times S^1 \to \mathbb{C}^{2n}, \tag{3.10}$$

with the phase variable $\phi \in S^1$. We can approximate $\mathbf{W}(\mathbf{s},\phi)$ in a neighborhood of the origin using a Taylor expansion in the parameterization coordinates $\mathbf{s} = (s_1, s_2 = \bar{s}_1)$, with coefficients that depend periodically on the phase variable ϕ.

(iii) There exists a polynomial function $\mathbf{R}(\mathbf{s},\phi) : \mathcal{U} \to \mathcal{U}$ satisfying the invariance relationship

$$\begin{aligned} &\mathbf{\Lambda}\mathbf{W}(\mathbf{s},\phi) + \mathbf{G}_\text{m}(\mathbf{W}(\mathbf{s},\phi)) + \varepsilon\mathbf{F}_\text{m}(\phi) \\ &= D_\mathbf{s}\mathbf{W}(\mathbf{s},\phi)\mathbf{R}(\mathbf{s},\phi) + D_\phi\mathbf{W}(\mathbf{s},\phi)\Omega, \end{aligned} \tag{3.11}$$

such that the reduced dynamics on the SSM can be expressed as

$$\dot{\mathbf{s}} = \mathbf{R}(\mathbf{s},\phi). \tag{3.12}$$

Proof : We have simply restated the main theorem by Haller and Ponsioen [4], which is based on the more abstract results of Cabré et al. [22, 23, 24] for mappings on Banach spaces.

In the upcoming sections, we will explain how to construct non-autonomous SSMs and show that the fixed points of the reduced dynamics represent limit cycles in the full phase space. These limit cycles, in turn, each correspond to points on the FRC for a particular forcing frequency.

3.4 Non-autonomous SSM computation

By the smooth dependence of the SSM on ε, we can write

$$\mathbf{W}(\mathbf{s},\phi) = \mathbf{W}_0(\mathbf{s}) + \varepsilon\mathbf{W}_1(\mathbf{s},\phi) + \mathcal{O}(\varepsilon^2), \tag{3.13}$$

$$\mathbf{R}(\mathbf{s},\phi) = \mathbf{R}_0(\mathbf{s}) + \varepsilon\mathbf{R}_1(\mathbf{s},\phi) + \mathcal{O}(\varepsilon^2). \tag{3.14}$$

We now substitute Eqs. (3.13)-(3.14) into the invariance Eq. (3.11) and collect terms of equal order in ε. Given that $\mathbf{G}_\mathrm{m}(\mathbf{q}) = \mathcal{O}(|\mathbf{q}|^2)$, we can Taylor-expand $\mathbf{G}_\mathrm{m}(\mathbf{W}(\mathbf{s},\phi))$ around $\varepsilon = 0$, to obtain

$$\mathbf{G}_\mathrm{m}(\mathbf{W}(\mathbf{s},\phi)) = \mathbf{G}_\mathrm{m}(\mathbf{W}_0(\mathbf{s})) + \varepsilon D_\mathbf{q}\mathbf{G}_\mathrm{m}(\mathbf{W}_0(\mathbf{s}))\mathbf{W}_1(\mathbf{s},\phi) + \mathcal{O}(\varepsilon^2). \tag{3.15}$$

3.4.1 The autonomous coefficient equations

Collecting terms of $\mathcal{O}(1)$, we obtain the coefficient equations corresponding to the autonomous part of the SSM

$$\mathbf{\Lambda}\mathbf{W}_0(\mathbf{s}) + \mathbf{G}_\mathrm{m}(\mathbf{W}_0(\mathbf{s})) = D_\mathbf{s}\mathbf{W}_0(\mathbf{s})\mathbf{R}_0(\mathbf{s}). \tag{3.16}$$

The autonomous part of the SSM and the reduced dynamics, which have previously been derived from an expansion in ε, are in turn Taylor expanded in the parameterization coordinates $\mathbf{s}$, which we explicitly express as

$$\mathbf{W}_0(\mathbf{s}) = \begin{bmatrix} w_1^0(\mathbf{s}) \\ \vdots \\ w_{2n}^0(\mathbf{s}) \end{bmatrix}, \quad w_i^0(\mathbf{s}) = \sum_\mathbf{m} W_{i,\mathbf{m}}^0 \mathbf{s}^\mathbf{m}, \tag{3.17}$$

$$\mathbf{R}_0(\mathbf{s}) = \begin{bmatrix} r_1^0(\mathbf{s}) \\ r_2^0(\mathbf{s}) \end{bmatrix}, \quad r_i^0(\mathbf{s}) = \sum_\mathbf{m} R_{i,\mathbf{m}}^0 \mathbf{s}^\mathbf{m}, \tag{3.18}$$

where we use the multi-index notation $\mathbf{m} \in \mathbb{N}_0^2$.

Theorem 3.2 *The coefficient equation related to the $\boldsymbol{k}^{th}$-power term of the i^{th} row of the autonomous invariance Eq. (3.16), for $|\mathbf{k}| > 2$, is equal to*

$$\left(\lambda_i - \sum_{j=1}^{2} k_j\lambda_j\right) W_{i,\mathbf{k}}^0 = \sum_{j=1}^{2} \delta_{ij} R_{j,\mathbf{k}}^0 + Q_{i,\mathbf{k}}, \tag{3.19}$$

where $Q_{i,\mathbf{k}}$ can be written as

$$\sum_{j=1}^{2} \sum_{\substack{\mathbf{m}\leq\tilde{\mathbf{k}}_j \\ \mathbf{m}\neq\mathbf{e}_j \\ \mathbf{m}\neq\mathbf{k} \\ m_j>0}} m_j W_{i,\mathbf{m}}^0 R_{j,\tilde{\mathbf{k}}_j-\mathbf{m}}^0 - \left[g_i(\mathbf{W}_0(\mathbf{s}))\right]_\mathbf{k}.$$

Proof We derive this result in Appendix 3.A.

Solving the autonomous invariance equation for $|\mathbf{k}| > 0$

As the autonomous part of the SSM is tangent to the spectral subspace $\mathcal{E}$ by construction (see Cabré et al. [24]), we have that

$$\begin{aligned} \mathbf{W}_0(\mathbf{0}) &= \mathbf{0}, \quad D_{\mathbf{s}}\mathbf{W}_0(\mathbf{0})\mathcal{E} = \mathcal{E}, \\ \mathbf{R}_0(\mathbf{0}) &= \mathbf{0}, \quad D_{\mathbf{s}}\mathbf{R}_0(\mathbf{0}) = \Lambda_{\mathcal{E}}, \end{aligned}$$

which satisfies the autonomous coefficient Eq. (3.16) for $|\mathbf{k}| = 0$ and $|\mathbf{k}| = 1$. For $|\mathbf{k}| \geq 2$, we solve Eq. (3.19) for $W^0_{i,\mathbf{k}}$, which yields

$$W^0_{i,\mathbf{k}} = \frac{\sum_{j=1}^{2} \delta_{ij} R^0_{j,\mathbf{k}} + Q_{i,\mathbf{k}}}{\lambda_i - \sum_{j=1}^{2} k_j \lambda_j}. \tag{3.20}$$

3.4.2 Removing near-resonant terms from the autonomous SSM

As observed by Szalai et al. [16], if the spectral subspace $\mathcal{E}$ is lightly damped, the near-resonance relationships

$$\lambda_1 - ((k+1)\lambda_1 + k\lambda_2) \approx 0, \quad \lambda_2 - (k\lambda_1 + (k+1)\lambda_2) \approx 0 \tag{3.21}$$

hold for $k \in \mathbb{N}^+$. Specifically, we consider the damping in the spectral subspace $\mathcal{E}$ light if

$$|\mathrm{Re}(\lambda_1)| \ll \frac{1}{2k}. \tag{3.22}$$

When this relation holds, Eq. (3.20) will have large denominators, generally reducing the domain of convergence of the Taylor series approximations for $\mathbf{W}(\mathbf{s})$. To counter this effect, we will remove these near-resonant terms from the expression of the autonomous SSM and place them in the autonomous part of the reduced dynamics by setting

$$R^0_{1,(k+1,k)} = -Q_{1,(k+1,k)} := \gamma_k \quad \Rightarrow \quad W^0_{1,(k+1,k)} = 0, \tag{3.23}$$

$$R^0_{2,(k,k+1)} = -Q_{2,(k,k+1)} := \bar{\gamma}_k \quad \Rightarrow \quad W^0_{2,(k,k+1)} = 0. \tag{3.24}$$

This results in

$$\mathbf{R}_0(\mathbf{s}) = \begin{bmatrix} \lambda_1 s_1 + \sum_{i=1}^{M} \gamma_i s_1^{i+1} \bar{s}_1^{i} \\ \bar{\lambda}_1 \bar{s}_1 + \sum_{i=1}^{M} \bar{\gamma}_i s_1^{i} \bar{s}_1^{i+1} \end{bmatrix}, \quad M \in \mathbb{N}^+. \tag{3.25}$$

where we assumed that

$$|\mathrm{Re}(\lambda_1)| \ll \frac{1}{2M}. \tag{3.26}$$

3.4.3 The non-autonomous coefficient equations

Collecting terms of $\mathcal{O}(\varepsilon)$ we obtain

$$\begin{aligned}&\mathbf{\Lambda W}_1(\mathbf{s},\phi) + D_{\mathbf{q}}\mathbf{G}_{\mathrm{m}}(\mathbf{W}_0(\mathbf{s}))\mathbf{W}_1(\mathbf{s},\phi) + \mathbf{F}_{\mathrm{m}}(\phi) \\ &= D_{\mathbf{s}}\mathbf{W}_0(\mathbf{s})\mathbf{R}_1(\mathbf{s},\phi) + D_{\mathbf{s}}\mathbf{W}_1(\mathbf{s},\phi)\mathbf{R}_0(\mathbf{s}) + D_{\phi}\mathbf{W}_1(\mathbf{s},\phi)\Omega.\end{aligned} \tag{3.27}$$

The non-autonomous part of the SSM and the reduced dynamics, are Taylor-expanded in the parameterization coordinates $\mathbf{s}$, which we explicitly express as

$$\mathbf{W}_1(\mathbf{s},\phi) = \begin{bmatrix} w_1^1(\mathbf{s},\phi) \\ \vdots \\ w_{2n}^1(\mathbf{s},\phi)\end{bmatrix}, \quad w_i^1(\mathbf{s},\phi) = \sum_{\mathbf{m}} W_{i,\mathbf{m}}^1(\phi)\mathbf{s}^{\mathbf{m}}, \tag{3.28}$$

$$\mathbf{R}_1(\mathbf{s},\phi) = \begin{bmatrix} r_1^1(\mathbf{s},\phi) \\ r_2^1(\mathbf{s},\phi)\end{bmatrix}, \quad r_i^1(\mathbf{s},\phi) = \sum_{\mathbf{m}} R_{i,\mathbf{m}}^1(\phi)\mathbf{s}^{\mathbf{m}}. \tag{3.29}$$

Theorem 3.3 *For $\phi \in S^1$, the coefficient equation related to the $\boldsymbol{k}^{th}$-power term of the i^{th} row of the non-autonomous invariance Eq. (3.27), is equal to*

$$\left(\lambda_i - \sum_{j=1}^{2} k_j\lambda_j\right) W_{i,\mathbf{k}}^1(\phi) - D_{\phi}W_{i,\mathbf{k}}^1(\phi)\Omega = \sum_{j=1}^{2}\delta_{ij}R_{j,\mathbf{k}}^1(\phi) + P_{i,\mathbf{k}}(\phi), \tag{3.30}$$

where $P_{i,\mathbf{k}}(\phi)$ can be written as

$$\begin{aligned}P_{i,\mathbf{k}}(\phi) = &\sum_{j=1}^{2}\sum_{\substack{\mathbf{m}\le\tilde{\mathbf{k}}_j \\ \mathbf{m}\neq\mathbf{e}_j \\ m_j>0}} m_j W_{i,\mathbf{m}}^0 R_{j,\tilde{\mathbf{k}}_j-\mathbf{m}}^1(\phi) + \sum_{j=1}^{2}\sum_{\substack{\mathbf{m}\le\tilde{\mathbf{k}}_j \\ \mathbf{m}\neq\mathbf{k} \\ m_j>0}} m_j W_{i,\mathbf{m}}^1(\phi) R_{j,\tilde{\mathbf{k}}_j-\mathbf{m}}^0 \\ &- F_{i,\mathbf{k}}(\phi) - \left[\sum_{j=1}^{2n} D_{q_j}g_i(\mathbf{W}_0(\mathbf{s}))w_j^1(\mathbf{s},\phi)\right]_{\mathbf{k}}.\end{aligned} \tag{3.31}$$

Proof We derive this result in Appendix 3.B.

Solving the non-autonomous invariance equation for $|\mathrm{k}| = 0$

For $|\mathbf{k}| = \mathbf{0}$, Eq. (3.30) becomes

$$\lambda_i W_{i,\mathbf{0}}^1(\phi) - D_{\phi}W_{i,\mathbf{0}}^1(\phi)\Omega = \sum_{j=1}^{2}\delta_{ij}R_{j,\mathbf{0}}^1(\phi) - F_{i,\mathbf{0}}(\phi), \tag{3.32}$$

Assuming that the forcing term $F_{i,\mathbf{0}}(\phi)$ can be written as

$$F_{i,\mathbf{0}}(\phi) = \tilde{F}_{i,\mathbf{0}} \frac{\mathrm{e}^{\mathrm{i}\phi} + \mathrm{e}^{-\mathrm{i}\phi}}{2}, \tag{3.33}$$

we express $W^1_{i,\mathbf{0}}(\phi)$ and $R^1_{i,\mathbf{0}}(\phi)$ in the following form

$$W^1_{i,\mathbf{0}}(\phi) = a_{i,\mathbf{0}}\mathrm{e}^{\mathrm{i}\phi} + b_{i,\mathbf{0}}\mathrm{e}^{-\mathrm{i}\phi}, \quad R^1_{i,\mathbf{0}}(\phi) = c_{i,\mathbf{0}}\mathrm{e}^{\mathrm{i}\phi} + d_{i,\mathbf{0}}\mathrm{e}^{-\mathrm{i}\phi}. \tag{3.34}$$

We can now write the solution of Eq. (3.32) as

$$W^1_{i,\mathbf{0}} = \frac{\delta_{i1}c_{1,\mathbf{0}} + \delta_{i2}c_{2,\mathbf{0}} - \frac{1}{2}\tilde{F}_{i,\mathbf{0}}}{\lambda_i - \mathrm{i}\Omega}\mathrm{e}^{\mathrm{i}\phi} + \frac{\delta_{i1}d_{1,\mathbf{0}} + \delta_{i2}d_{2,\mathbf{0}} - \frac{1}{2}\tilde{F}_{i,\mathbf{0}}}{\lambda_i + \mathrm{i}\Omega}\mathrm{e}^{-\mathrm{i}\phi}. \tag{3.35}$$

For lightly damped systems where $\mathrm{Re}\lambda_1$ is small, we obtain small denominators in Eq. (3.35) if the forcing frequency Ω is approximately equal to $\mathrm{Im}\lambda_1$. We, therefore, intend to remove this near-resonance by setting

$$c_{1,\mathbf{0}} = \frac{1}{2}\tilde{F}_{1,\mathbf{0}}, \quad c_{2,\mathbf{0}} = 0, \quad d_{1,\mathbf{0}} = 0, \quad d_{2,\mathbf{0}} = \frac{1}{2}\tilde{F}_{2,\mathbf{0}}. \tag{3.36}$$

Solving the non-autonomous invariance equation for $|\mathbf{k}| > 0$

For $|\mathbf{k}| > 0$, the solution to the non-autonomous invariance Eq. (3.30) takes the form

$$W^1_{i,\mathbf{k}}(\phi) = \underbrace{\frac{\sum_{j=1}^2 \delta_{ij}c_{j,\mathbf{k}} + \alpha_{i,\mathbf{k}}}{\lambda_i - \sum_{j=1}^2 k_j\lambda_j - \mathrm{i}\Omega}}_{a_{i,\mathbf{k}}}\mathrm{e}^{\mathrm{i}\phi} + \underbrace{\frac{\sum_{j=1}^2 \delta_{ij}d_{j,\mathbf{k}} + \beta_{i,\mathbf{k}}}{\lambda_i - \sum_{j=1}^2 k_j\lambda_j + \mathrm{i}\Omega}}_{b_{i,\mathbf{k}}}\mathrm{e}^{-\mathrm{i}\phi}, \tag{3.37}$$

where we introduced the following notation for $P_{i,\mathbf{k}}$ in Eq. (3.31)

$$P_{i,\mathbf{k}} = \alpha_{i,\mathbf{k}}\mathrm{e}^{\mathrm{i}\phi} + \beta_{i,\mathbf{k}}\mathrm{e}^{-\mathrm{i}\phi}.$$

3.4.4 Removing near-resonant terms from the non-autonomous SSM

Using the same reasoning as in section 3.4.3, we want to choose $c_{i,\mathbf{k}}$ and $d_{i,\mathbf{k}}$ in Eq. (3.37) in such a way that we prevent the coefficients $a_{i,\mathbf{k}}$ and $b_{i,\mathbf{k}}$ form having any small denominators. We observe that if the spectral subspace $\mathcal{E}$ is lightly damped and the forcing frequency Ω is close to $\mathrm{Im}\lambda_1$, the near-resonance relationships

$$\begin{aligned}
&\lambda_1 - (k\lambda_1 + k\lambda_2) - \mathrm{i}\Omega \approx 0,\\
&\lambda_1 - ((k+1)\lambda_1 + (k-1)\lambda_2) + \mathrm{i}\Omega \approx 0,\\
&\lambda_2 - (k\lambda_1 + k\lambda_2) + \mathrm{i}\Omega \approx 0,\\
&\lambda_2 - ((k-1)\lambda_1 + (k+1)\lambda_2) - \mathrm{i}\Omega \approx 0,
\end{aligned}$$

hold for $k \in \mathbb{N}^+$, where, for the non-autonomous expressions, a lightly damped spectral subspace $\mathcal{E}$ implies that

$$|\mathrm{Re}(\lambda_1)| \ll \frac{1}{|1-2k|}. \tag{3.38}$$

Eq. (3.38) is automatically satisfied if the small damping assumption in Eq. (3.22) is satisfied, because

$$\frac{1}{2k} < \frac{1}{|1-2k|}, \quad k \in \mathbb{N}^+. \tag{3.39}$$

The near-resonance terms are removed from the expressions of $\mathbf{W}_1(\mathbf{s},\phi)$ and included into the non-autonomous part of the reduced dynamics $\mathbf{R}_1(\mathbf{s},\phi)$ if we set

$$\begin{aligned} c_{1,(k,k)} = -\alpha_{1,(k,k)} \quad &\Rightarrow \quad a_{1,(k,k)} = 0, \\ d_{2,(k,k)} = -\beta_{2,(k,k)} \quad &\Rightarrow \quad b_{2,(k,k)} = 0, \\ d_{1,(k+1,k-1)} = -\beta_{1,(k+1,k-1)} \quad &\Rightarrow \quad b_{1,(k+1,k-1)} = 0, \\ c_{2,(k-1,k+1)} = -\alpha_{2,(k-1,k+1)} \quad &\Rightarrow \quad a_{2,(k-1,k+1)} = 0, \end{aligned}$$

where, by construction, we have

$$\begin{aligned} d_{2,(k,k)} &= \bar{c}_{1,(k,k)}, \\ c_{2,(k-1,k+1)} &= \bar{d}_{1,(k+1,k-1)}. \end{aligned}$$

This results in the following form for the non-autonomous part of the reduced dynamics:

$$\mathbf{R}_1(\mathbf{s},\phi) = \begin{bmatrix} c_{1,\mathbf{0}}\mathrm{e}^{\mathrm{i}\phi} & + \sum_{i=1}^{M} \left(c_{1,(i,i)}(\Omega) s_1^i \bar{s}_1^i \mathrm{e}^{\mathrm{i}\phi} + d_{1,(i+1,i-1)}(\Omega) s_1^{i+1} \bar{s}_1^{i-1} \mathrm{e}^{-\mathrm{i}\phi} \right) \\ \bar{c}_{1,\mathbf{0}}\mathrm{e}^{-\mathrm{i}\phi} & + \sum_{i=1}^{M} \left(\bar{c}_{1,(i,i)}(\Omega) s_1^i \bar{s}_1^i \mathrm{e}^{-\mathrm{i}\phi} + \bar{d}_{1,(i+1,i-1)}(\Omega) s_1^{i-1} \bar{s}_1^{i+1} \mathrm{e}^{\mathrm{i}\phi} \right) \end{bmatrix},$$

where Eq. (3.26) implies that $|\mathrm{Re}(\lambda_1)| \ll \frac{1}{2M} < \frac{1}{|1-2M|}$.

3.5 Reduced dynamics on the non-autonomous SSM

Our next result concerns the dynamics on the SSM described in Theorem 3.1

Theorem 3.4 *Under the assumption that $|Re(\lambda_1)| \ll \frac{1}{2M}$, the dynamics on the two-dimensional SSM given in Theorem 3.1 can approximately be written in polar coordinates (ρ,ψ) as*

$$\dot{\rho} = a(\rho) + \varepsilon \left(f_1(\rho,\Omega)\cos(\psi) + f_2(\rho,\Omega)\sin(\psi) \right), \tag{3.40}$$

$$\dot{\psi} = (b(\rho) - \Omega) + \frac{\varepsilon}{\rho} \left(g_1(\rho,\Omega)\cos(\psi) - g_2(\rho,\Omega)\sin(\psi) \right), \tag{3.41}$$

where

$$a(\rho) = \mathrm{Re}(\lambda_1)\rho + \sum_{i=1}^{M} \mathrm{Re}(\gamma_i)\rho^{2i+1}, \tag{3.42}$$

$$b(\rho) = \mathrm{Im}(\lambda_1) + \sum_{i=1}^{M} \mathrm{Im}(\gamma_i)\rho^{2i}, \tag{3.43}$$

$$f_1(\rho,\Omega) = \mathrm{Re}(c_{1,\mathbf{0}}) + \sum_{i=1}^{M} \left(\mathrm{Re}(c_{1,(i,i)}(\Omega)) + \mathrm{Re}(d_{1,(i+1,i-1)}(\Omega))\right)\rho^{2i}, \tag{3.44}$$

$$f_2(\rho,\Omega) = \mathrm{Im}(c_{1,\mathbf{0}}) + \sum_{i=1}^{M} \left(\mathrm{Im}(c_{1,(i,i)}(\Omega)) - \mathrm{Im}(d_{1,(i+1,i-1)}(\Omega))\right)\rho^{2i}, \tag{3.45}$$

$$g_1(\rho,\Omega) = \mathrm{Im}(c_{1,\mathbf{0}}) + \sum_{i=1}^{M} \left(\mathrm{Im}(c_{1,(i,i)}(\Omega)) + \mathrm{Im}(d_{1,(i+1,i-1)}(\Omega))\right)\rho^{2i}, \tag{3.46}$$

$$g_2(\rho,\Omega) = \mathrm{Re}(c_{1,\mathbf{0}}) + \sum_{i=1}^{M} \left(\mathrm{Re}(c_{1,(i,i)}(\Omega)) - \mathrm{Re}(d_{1,(i+1,i-1)}(\Omega))\right)\rho^{2i}, \tag{3.47}$$

with $2M+1$ denoting the order of the expansion.

Proof : We derive this result in Appendix 3.C.

We note that Theorem 3.1, upon which Theorem 3.4 is based, is specifically geared towards constructing the SSM corresponding to the slowest vibration mode of system (3.5). However, the main result of Haller and Ponsioen [4] is general enough to allow for the construction of an SSM over any mode of interest as long as appropriate non-resonance conditions are satisfied. Therefore, an approach similar to the one described in this section can be applied to extract the FRCs of higher-order modes.

In the unforced limit ($\varepsilon = 0$), the reduced system (3.40)-(3.41) can have fixed points but no nontrivial periodic orbits. This is because (3.40) decouples from (3.41), representing a one-dimensional ordinary differential equation that cannot have non-constant periodic solutions. By construction, the trivial fixed point of (3.40)-(3.41) is asymptotically stable and will persist for $\varepsilon > 0$. These persisting fixed points satisfy the system of equations

$$\begin{aligned}\mathbf{F}(\mathbf{u}) &= \begin{bmatrix} F_1(\mathbf{u}) \\ F_2(\mathbf{u}) \end{bmatrix} \\ &= \begin{bmatrix} a(\rho) + \varepsilon\left(f_1(\rho,\Omega)\cos(\psi) + f_2(\rho,\Omega)\sin(\psi)\right) \\ (b(\rho)-\Omega)\rho + \varepsilon\left(g_1(\rho,\Omega)\cos(\psi) - g_2(\rho,\Omega)\sin(\psi)\right) \end{bmatrix} = \mathbf{0},\end{aligned} \tag{3.48}$$

where

$$\mathbf{F}(\mathbf{u}) : \mathbb{R}^3 \to \mathbb{R}^2, \quad \mathbf{u} = \begin{bmatrix} \rho \\ \Omega \\ \psi \end{bmatrix}.$$

If there exists a regular point $\mathbf{p} = (\rho, \Omega, \psi)$, such that $\mathbf{F}(\mathbf{p}) = \mathbf{0}$ in (3.48) and the Jacobian of $\mathbf{F}$ evaluated at $\mathbf{p}$ is surjective, then by the implicit function theorem, locally there exists a one-dimensional submanifold of $\mathbb{R}^3$ which will represent the forced response curve when projected onto the (Ω, ρ)-space. The stability of these fixed points (which correspond to periodic solutions of the full mechanical system) is determined by the real parts of the eigenvalues of the Jacobian of $\mathbf{F}(\mathbf{u})$, as illustrated in Fig. 3.1.

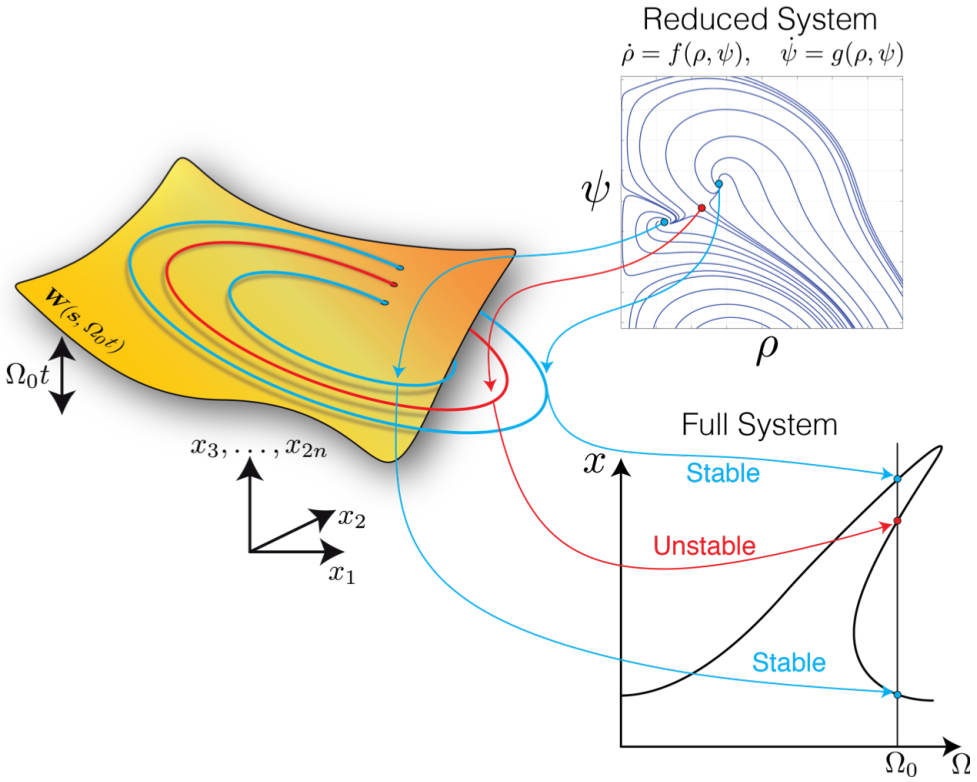

Figure 3.1: Illustration of how the fixed points of the reduced dynamics for a fixed forcing frequency Ω_0 are mapped to periodic orbits in the full phase space by the mapping $\mathbf{W}(\mathbf{s}, \Omega_0 t)$.

In Appendix 3.E, we give a geometric interpretation of the construction of zeros for the reduced dynamics on the SSM.

In summary, Theorem 3.4 gives explicit formulas that enable the calculation of the exact dynamics up to any required order of accuracy for the SSMs associated with the normal modes of the original mechanical system (3.1). Once the reduced dynamics is calculated, finding the nonlinear periodic responses of the system, including isolas, simply amounts to finding the zeros of the right-hand side of Eqs. (3.40)-(3.41). No other numerical simulation or iteration is involved in constructing the forced response from SSM-based, exact model reduction.

3.6 Example: A discretized, forced Bernoulli beam with a nonlinear spring

As an application of our main result on non-autonomous, SSM-based model reduction and forced response, we now consider a discretized, cantilevered Bernoulli beam with a cubic spring attached to the free end of the beam. We extract the forced-response curve around the first eigenfrequency of the beam using SSMtool[2], the HB method (NLvib tool [61]) and the `po` toolbox of COCO, a numerical continuation package discussed in [31]. We apply all three methods on the same discretized beam for an increasing number of elements in the discretization, ranging from 10 degrees of freedom to 10,000 degrees of freedom. We note that NLvib tool and COCO only run in series. Indeed, neither approach would benefit from parallelization over different forcing cases, as steady-state responses forced for one parameter configuration are heavily used to initialize the search for steady states for the next parameter configuration. In contrast, finding steady states from SSMtool involves no numerical simulations or iterations and hence can be done in parallel for all forcing parameter values of interest. We will nevertheless include results from SSMtool run in series, in addition to a parallelized run over 20 processors.

3.6.1 Equations of motion for the Bernoulli beam

The beam is of length L, with the square cross-section A, situated in a Cartesian coordinate system of (x, y, z) and basis $(\mathbf{e}_x, \mathbf{e}_y, \mathbf{e}_z)$. The relevant beam parameters are listed in Table 3.1. The line of points coinciding with the x-axis is called the beam's neutral axis. The Bernoulli hypothesis states that initially straight material lines, normal to the neutral axis, remain (a) straight and (b) inextensible, and (c) rotate as rigid lines to remain perpendicular to the beam's neutral axis after

[2] SSMtool is available at: `www.georgehaller.com`.

Table 3.1: Notation used in the discretized beam example.

Symbol	Meaning (unit)
L	Length of beam (mm)
h	Height of beam (mm)
b	Width of beam (mm)
ρ	Density (kg/mm^3)
E	Young's Modulus (kPa)
I	Area moment of inertia (mm^4)
κ	Coefficient cubic spring (mN/mm^3)
A	Cross-section of beam (mm^2)
P	External forcing amplitude (mN)

deformation. These kinematic assumptions are satisfied the displacement field,

$$u_x(x,y,z,t) = -z\frac{\partial w(x,t)}{\partial x}, \tag{3.49}$$

$$u_y(x,y,z,t) = 0, \tag{3.50}$$

$$u_z(x,y,z,t) = w(x,t), \tag{3.51}$$

where (u_x, u_y, u_z) are the components of the displacement field $\mathbf{u}(x,y,z,t)$ of a material point located at (x,y,z). The transverse displacement of a material point with initial coordinates on the beam's neutral axis at $z = 0$ is denoted by $w(x)$. The rotation angle of a transverse normal line about the y-axis is given by $-\partial_x w(x)$.

Using the Green-Lagrange strain tensor, we can express the relevant strains as

$$\varepsilon_{xx} = -z\frac{\partial^2 w(x,t)}{\partial x^2}, \quad \gamma_{xz} = 2\varepsilon_{xz} = 0. \tag{3.52}$$

We assume an isotropic, linearly elastic constitutive relation between the stresses and strains, i.e.

$$\sigma_{xx} = E\varepsilon_{xx}, \tag{3.53}$$

which finally leads to the equation of motion of the beam

$$\rho A\frac{\partial^2 w(x,t)}{\partial t^2} - \rho I\frac{\partial^4 w(x,t)}{\partial x^2 \partial t^2} + EI\frac{\partial^4 w(x,t)}{\partial x^4} = 0. \tag{3.54}$$

We assume that the thickness of the beam is small compared to its length, i.e., $h \ll L$, and hence we can neglect the mixed partial derivative term in Eq. (3.54) (cf. Reddy and Mahaffey [33]).

After discretization of (3.54), we obtain the set of ordinary differential equations

$$\mathbf{M}\ddot{\mathbf{x}} + \mathbf{K}\mathbf{x} = \mathbf{0}, \tag{3.55}$$

where $\mathbf{x} \in \mathbb{R}^{2m}$, and m is the number of elements used in the discretization. Each node of the beam has two coordinates related to the transverse displacement $w(x)$ and the rotation angle $-\partial_x w(x)$ of the cross section. We assume structural damping by considering the damping matrix

$$\mathbf{C} = \alpha\mathbf{M} + \beta\mathbf{K}, \tag{3.56}$$

with parameters α and β. We apply cosinusoidal external forcing on the transverse displacement coordinate at the free end of the beam with forcing frequency Ω and forcing amplitude εP. Additionally, we add a cubic spring along this coordinate with coefficient κ. As a result, the equations of motion of the beam can be written as

$$\mathbf{M}\ddot{\mathbf{x}} + \mathbf{C}\dot{\mathbf{x}} + \mathbf{K}\mathbf{x} + \mathbf{g}(\mathbf{x}, \dot{\mathbf{x}}) = \varepsilon\mathbf{f}(\Omega t). \tag{3.57}$$

We illustrate the kinematics, the forcing and the cubic spring in Fig. 3.2.

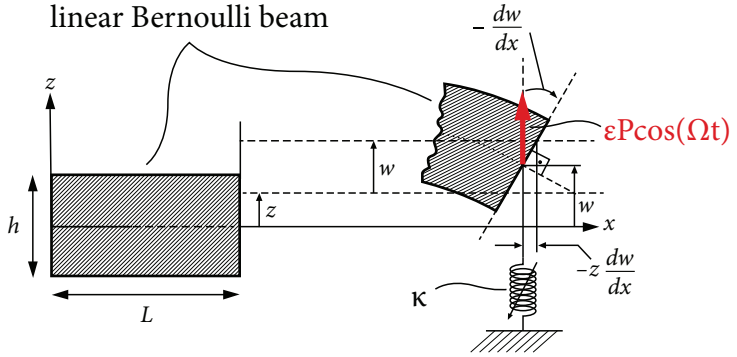

Figure 3.2: Forced Bernoulli beam with a cubic spring.

We transform Eq. (3.57) to first-order form by setting $\mathbf{x} = [\mathbf{x}_1, \mathbf{x}_2]^\top = [\mathbf{y}, \dot{\mathbf{y}}]^\top$ and apply a change of coordinates $\mathbf{x} = \mathbf{T}\mathbf{q}$, resulting in

$$\begin{aligned}
\dot{\mathbf{q}} &= \mathbf{T}^{-1}\begin{pmatrix} \mathbf{0} & \mathbf{I} \\ -\mathbf{M}^{-1}\mathbf{K} & -\mathbf{M}^{-1}\mathbf{C} \end{pmatrix}\mathbf{T}\mathbf{q} + \mathbf{T}^{-1}\begin{pmatrix} \mathbf{0} \\ -\mathbf{M}^{-1}\mathbf{g}(\mathbf{T}\mathbf{q}) \end{pmatrix} \\
&\quad + \varepsilon\mathbf{T}^{-1}\begin{pmatrix} \mathbf{0} \\ \mathbf{M}^{-1}\mathbf{f}(\Omega t) \end{pmatrix} \\
&= \mathbf{\Lambda}\mathbf{q} + \mathbf{T}^{-1}\begin{pmatrix} \mathbf{0} & \mathbf{0} \\ \mathbf{0} & \mathbf{M}^{-1} \end{pmatrix}\begin{pmatrix} 0 \\ \vdots \\ -\kappa\left(\sum_{i=1}^{2n}[\mathbf{T}]_{n-1,i}q_i\right)^3 \\ 0 \end{pmatrix} \\
&\quad + \varepsilon\mathbf{F}_{\mathrm{m}}(\Omega t) \\
&= \mathbf{\Lambda}\mathbf{q} + \mathbf{G}_{\mathrm{m}}(\mathbf{q}) + \varepsilon\mathbf{F}_{\mathrm{m}}(\Omega t).
\end{aligned} \tag{3.58}$$

3.6.2 Constructing the SSM-reduced system

Using SSMtool, we compute a third-order SSM reduced model of system (3.58), which will take the following form

$$\dot{\rho} = a(\rho) + \varepsilon \left(f_1(\rho, \Omega) \cos(\psi) + f_2(\rho, \Omega) \sin(\psi) \right), \tag{3.59}$$

$$\dot{\psi} = (b(\rho) - \Omega) + \frac{\varepsilon}{\rho} \left(g_1(\rho, \Omega) \cos(\psi) - g_2(\rho, \Omega) \sin(\psi) \right), \tag{3.60}$$

where

$$\begin{aligned}
a(\rho) &= \mathrm{Re}(\lambda_1)\rho + \mathrm{Re}(\gamma_1)\rho^3, \\
b(\rho) &= \mathrm{Im}(\lambda_1) + \mathrm{Im}(\gamma_1)\rho^2, \\
f_1(\rho, \Omega) &= \mathrm{Re}(c_{1,(0,0)}) + \left(\mathrm{Re}(c_{1,(1,1)}(\Omega)) + \mathrm{Re}(d_{1,(2,0)}(\Omega)) \right) \rho^2, \\
f_2(\rho, \Omega) &= \mathrm{Im}(c_{1,(0,0)}) + \left(\mathrm{Im}(c_{1,(1,1)}(\Omega)) - \mathrm{Im}(d_{1,(2,0)}(\Omega)) \right) \rho^2, \\
g_1(\rho, \Omega) &= \mathrm{Im}(c_{1,(0,0)}) + \left(\mathrm{Im}(c_{1,(1,1)}(\Omega)) + \mathrm{Im}(d_{1,(2,0)}(\Omega)) \right) \rho^2, \\
g_2(\rho, \Omega) &= \mathrm{Re}(c_{1,(0,0)}) + \left(\mathrm{Re}(c_{1,(1,1)}(\Omega)) - \mathrm{Re}(d_{1,(2,0)}(\Omega)) \right) \rho^2.
\end{aligned}$$

We can explicitly compute the autonomous and non-autonomous SSM coefficients, which are used to verify the output given by SSMtool,

$$\gamma_1 = -3\kappa [\tilde{\mathbf{B}}]_{1,2n-1} [\mathbf{T}]^2_{n-1,1} [\mathbf{T}]_{n-1,2}, \tag{3.61}$$

$$c_{1,(0,0)} = \frac{[\tilde{\mathbf{B}}]_{1,2n-1} P}{2}, \tag{3.62}$$

$$c_{1,(1,1)} = 6\kappa [\tilde{\mathbf{B}}]_{1,2n-1} [\mathbf{T}]_{n-1,1} [\mathbf{T}]_{n-1,2} \sum_{j=2}^{2n} \frac{[\mathbf{T}]_{n-1,j} [\tilde{\mathbf{B}}]_{j,2n-1} P}{2(\lambda_j - \mathrm{i}\Omega)}, \tag{3.63}$$

$$d_{1,(2,0)} = 3\kappa [\tilde{\mathbf{B}}]_{1,2n-1} [\mathbf{T}]^2_{n-1,1} \sum_{\substack{j=1 \\ j \neq 2}}^{2n} \frac{[\mathbf{T}]_{n-1,j} [\tilde{\mathbf{B}}]_{j,2n-1} P}{2(\lambda_j + \mathrm{i}\Omega)}, \tag{3.64}$$

where the matrix $\tilde{\mathbf{B}}$ is defined as

$$\tilde{\mathbf{B}} = \mathbf{T}^{-1} \begin{pmatrix} \mathbf{0} & \mathbf{0} \\ \mathbf{0} & \mathbf{M}^{-1} \end{pmatrix}. \tag{3.65}$$

3.6.3 Numerical results

In our upcoming comparison, the collocation computations were performed on a remote Intel Xeon E5-2680v3 processor (3.3 GHz) on the ETH cluster due to large computational times. The SSM and HB computations were performed on an Intel Xeon X5675 processor (3.07 GHz) on a local workstation. We now compute

the forced-response curves around the first vibration mode of the discretized beam model described above. The FRCs will be obtained independently from SSM theory, the harmonic balance method and a collocation method. We list the chosen geometric and material parameter values in Table 3.2.

Table 3.2: Geometric and material parameters for the Bernoulli beam.

Symbol	Value
L	$2700\,\mathrm{mm}$
h	$10\,\mathrm{mm}$
b	$10\,\mathrm{mm}$
ρ	$1780 \cdot 10^{-9}\,\mathrm{kg/mm^3}$
E	$45 \cdot 10^{6}\,\mathrm{kPa}$
κ	$4\,\mathrm{mN/mm^3}$
α	$1.25 \cdot 10^{-4}\,\mathrm{s^{-1}}$
β	$2.5 \cdot 10^{-4}\,\mathrm{s}$
P	$0.1\,\mathrm{mN}$

As system (3.58) is a discretized version of Eq. (3.54), the first natural frequency of the conservative, unforced, fixed-free beam, consisting of m elements, will approximate

$$\omega_1 = (\beta_1 l)^2 \sqrt{\frac{EI}{\rho A l^4}} \approx 7\,\mathrm{rad/s}, \quad \beta_1 l = 1.875104, \tag{3.66}$$

for an increasing value of m (see Rao [62]). If the damping is small, the imaginary part of λ_1 will approximately be equal to ω_1 (cf. Géradin and Rixen [29]).

We used the `ode_isol2po` toolbox constructor in coco [31] for continuation along a family of single-segment periodic orbits from an initial solution guess. The single-segment collocation zero problem is initially constructed on a default mesh with 10 intervals, 5 base points and 4 collocation nodes in each interval. The continuation algorithm is then instructed to make adaptive changes to the problem discretization after each step of continuation.

We also used the nlvib tool [61], which implements the HB method coupled to a path-continuation procedure. In the HB method, it is assumed that the system has a steady-state solution represented by a Fourier series

$$\mathbf{y} = \mathrm{Re}\Big(\sum_{k=0}^{\infty} \mathbf{c}_k \mathrm{e}^{\mathrm{i}k\Omega t}\Big), \tag{3.67}$$

where $\mathbf{c}_k \in \mathbb{C}^n$ is a vector containing the complex Fourier coefficients corresponding to the k^{th} harmonic. Furthermore, it is assumed that the nonlinear force vector $\mathbf{g}(\mathbf{y}, \dot{\mathbf{y}})$ can be approximated by a Fourier series as well.

By substituting the assumed solution (3.67) into the original ordinary differential equations (3.57) and restricting the result to finitely many harmonics H (we will use $H = 10$), the original equations are transformed into a set of nonlinear algebraic equations

$$\left(-(k\Omega)^2\mathbf{M} + \mathrm{i}k\Omega\mathbf{C} + \mathbf{K}\right)\mathbf{c}_k + \mathbf{f}_{\text{nl},k}(\mathbf{c}_0, \ldots, \mathbf{c}_H) - \mathbf{f}_{\text{ext},k} = \mathbf{0}, \quad k = 0, \ldots, H, \tag{3.68}$$

to be solved simultaneously for all $\mathbf{c}_k$, with $k = 0, \ldots, H$. This is typically done using a Newton-Raphson iteration scheme.

To evaluate the nonlinear force vector $\mathbf{f}_{\text{nl},k}(\mathbf{c}_0, \ldots, \mathbf{c}_H)$ in (3.68), NLvib tool uses the Alternating-Frequency-Time (AFT) method, proposed first by Cameron et al. [63], which uses the inverse Fourier transform of the positions and velocities in the frequency domain, creating a sampled time signal over one period of oscillation. The time signal is then substituted into the nonlinear force vector $\mathbf{g}(\mathbf{y}, \dot{\mathbf{y}})$ and the resulting output signal is in turn transformed back to the frequency domain using a Fourier transformation. For several implementations of the AFT method we refer to [64, 65, 66, 67].

A shortcoming of the HB method, as compared to SSM theory and the collocation method used by COCO, is that it does not provide any information about the stability of the solutions, which has to be analyzed in a separate effort. As described in Detroux et al. [64], a variant of Floquet theory can be used in order to identify the stability of the solutions, which is applicable in the frequency domain and is known as Hill's method [68]. This separate method has not been implemented in the current work.

We now compute the forced-response curve, around ω_1 (3.66), over the interval $S_\Omega = [6.88, 7.12]$ for an increasing number of elements m and $\varepsilon = 0.002$. We verify our results and compare the recorded computational times using SSMtool with the numerical continuation package COCO and the harmonic balance method. The corresponding computational times are listed in Fig. 3.3.

As can be seen in Fig. 3.3, the collocation based method with COCO takes 12 full days to compute the forced-response curve, over the interval S_Ω, for a 50-degrees-of-freedom system and due to this reason has not been used for higher-degrees-of-freedom simulations. For the discretized beam with 500-degrees-of-freedom, the HB method with 10 harmonics takes around 1 day to compute the forced response curve, where the number of nonlinear algebraic equations and unknowns is given by

$$p = n(2H + 1).$$

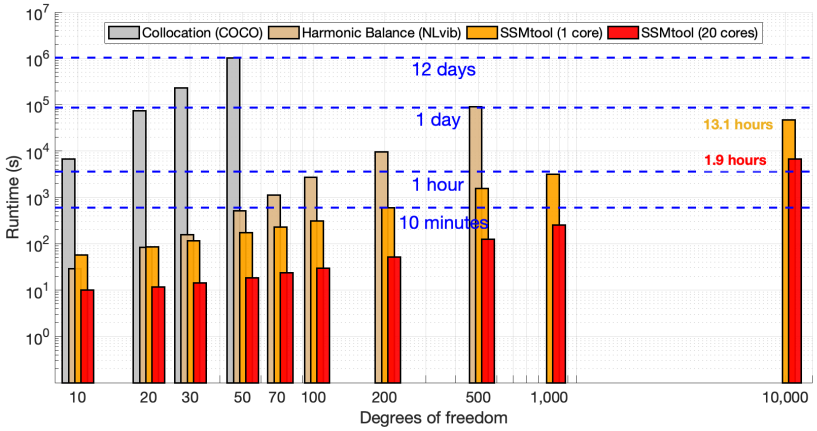

Figure 3.3: Computational times to extract the forced-response curve around the first vibration mode of a cantilevered Bernoulli beam with a cubic spring over the interval $S_\Omega = [6.88, 7.12]$, using collocation, harmonic balance and SSMtool.

For the 1000 degrees-of-freedom system, the total number of nonlinear algebraic equations is $p = 21000$, which has to be solved for the 21000 unknown Fourier coefficients. This becomes unfeasible using the available MATLAB implementation of the HB method.

For the SSMtool calculation, the 10,000 degrees of freedom example takes a total of 13 hours when computed on a single core. Here we sampled the frequency interval S_Ω for 60 frequency values Ω_i and computed the third-order approximation for the non-autonomous SSM. As the autonomous part does not depend on the forcing frequency Ω, we only have to compute this part once. The non-autonomous part is recalculated for different samples Ω_i, which makes it possible to parallelize the non-autonomous computations by dividing the frequency samples over different cores. Running the non-autonomous part of the SSM computation on 20 cores reduces the total computational time from 13 hours to 2 hours.

The resulting FRCs corresponding to the absolute maximum displacement during one period of oscillation of the transverse component at the free end of the beam, for $n = \{10, 50, 500, 10000\}$ over the interval S_Ω, are listed in Figs. 3.4. In Fig. 3.5 we illustrate the phase plane of the two-dimensional SSM-reduced system extracted from the 100 degrees-of-freedom beam example, showing how the domain of attraction of the higher amplitude stable fixed point reduces up to the point where a saddle-node bifurcation occurs, which is where the stable and saddle-type fixed points collide and annihilate each other.

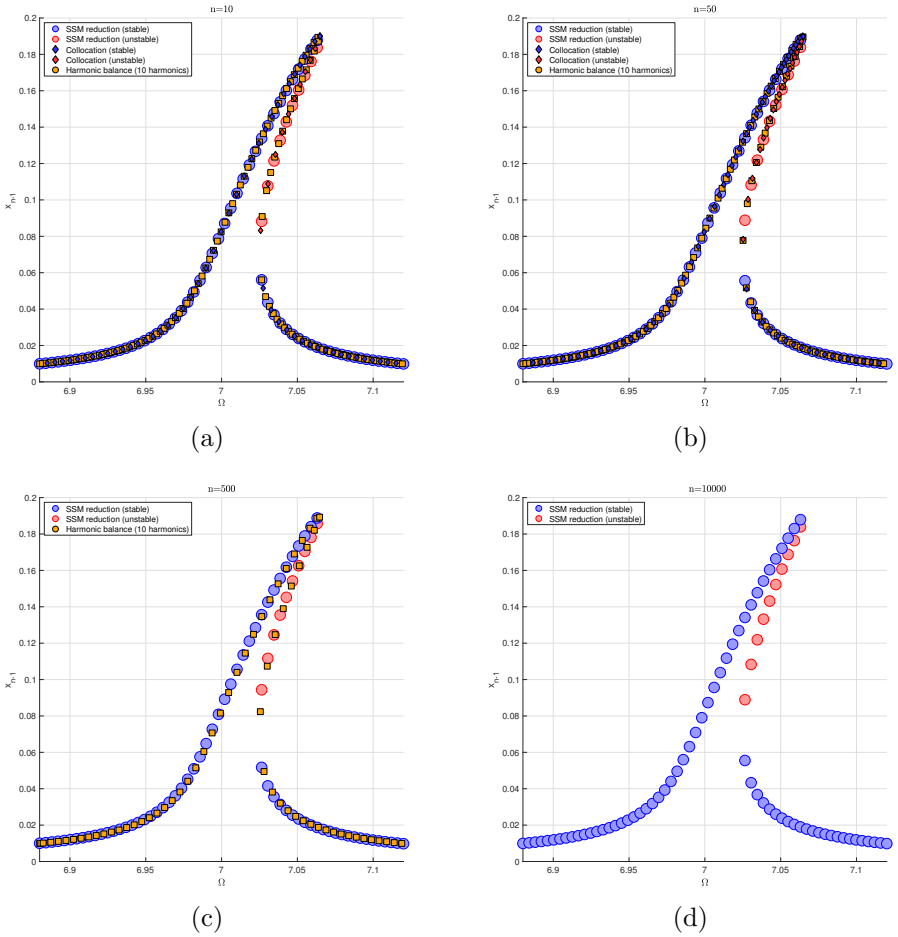

(a) (b) (c) (d)

Figure 3.4: Extracted forced response curves for x_{n-1}, using a third-order SSM reduced model, collocation and the harmonic balance method, for an increasing number of degrees of freedom n, where $n = \{10, 50, 500, 10000\}$ in Figs (a), (b), (c) and (d), respectively.

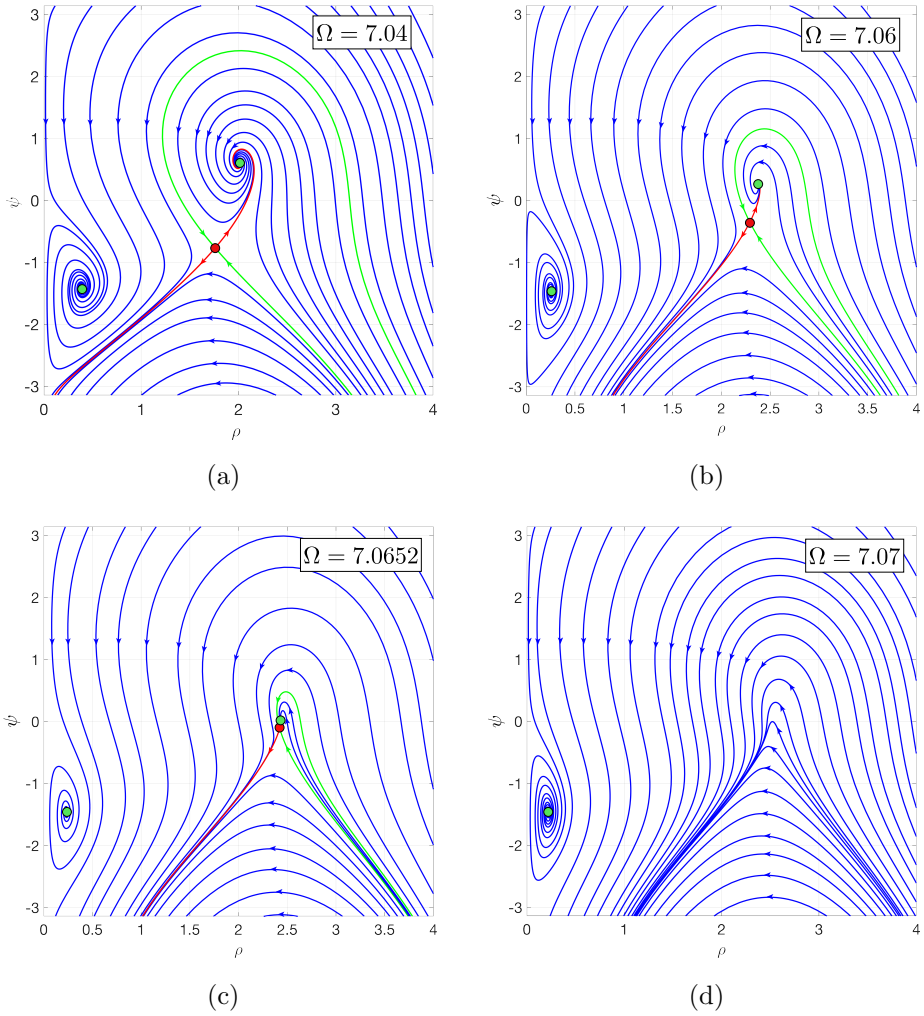

Figure 3.5: Phase plane of the two-dimensional SSM-reduced system extracted from the 100 degrees-of-freedom beam example for different forcing frequencies Ω and fixed forcing amplitude $\varepsilon = 0.002$. The Figures (a), (b) and (c), the reduced system has a total of three fixed points, of which two are stable spirals and one is a saddle. As the forcing frequency is increased (cf. Fig. (d)), a saddle-node bifurcation occurs where the two higher-amplitude fixed points collide and annihilate each other. The stable and unstable manifolds of the saddle-type fixed point are shown in green and red. Notice how the domain of attraction of the higher amplitude stable fixed point reduces significantly in area as the forcing frequency is increased, making it harder to end up in this particular fixed point.

3.7 Conclusions

In this work, we have used the reduced dynamics on two-dimensional time-periodic spectral submanifolds (SSMs) to extract forced-response curves (FRCs) around the vibration modes of nonlinear non-conservative mechanical systems. We compared the computational times needed to extract such FRCs from systems with an increasing number of degrees of freedom, using SSM theory, the harmonic balance (HB) method and a collocation method implemented in the `po` toolbox of COCO.

Varying the number of degrees of freedom, from 10 to a 10,000, we have found that extracting the FRC using the HB method and the collocation method becomes rapidly intractable. However, using SSMtool, a 10,000-degree-of-freedom system takes approximately 13 hours to obtain the FRC over a predefined set of frequency values.

An additional advantage of the present approach is that SSM computations can be parallelized. The frequency domain of interest can be divided into subsets and each computation over such a subset can be sent to a different core. For the 10,000 degrees-of-freedom system, running the SSMtool computation in parallel on 20 cores reduces the computational time from 13 hours to approximately 2 hours. These speeds and corresponding degrees of freedom appear certainly out of reach for any other approach that we are aware of for steady-state calculations in periodically forced nonlinear mechanical systems.

We have visualized the phase space of the two-dimensional SSM-reduced systems. Doing so we have reproduced the behavior commonly observed in experiments: during a frequency sweep of the system, following the higher-amplitude stable periodic solution branch becomes harder near folding points. Indeed, as our analysis reveals, small perturbations can cause the response of the system to escape the domain of attraction of the higher-amplitude stable periodic orbit, ending up in the domain of attraction of the lower-amplitude stable periodic solution. Specifically, the domain of attraction of the higher-amplitude fixed point, for the SSM-reduced system, shrinks in area up to the point where it completely vanishes during a saddle-node bifurcation.

When the forcing frequency, Ω, and the forcing amplitude, ε, are fixed, we showed that the zeros of the reduced dynamics lie on an ellipse-shaped curve, which gives a new geometric interpretation of the family of periodic orbits of the full system. Additionally, if we reduced our analysis to the setting of Breunung and Haller [8] and computed the non-autonomous part of the SSM only up to zeroth order in the parameterization coordinates, the ellipse would reduce to a circle.

In summary, we find that spectral submanifolds provide a mathematically exact model reduction tool for high-degree-of-freedom nonlinear mechanical systems at previously unthinkable speeds. The reduction method does not require the numer-

ical solution of differential equations: all effort goes into constructing appropriate matrices corresponding to a linear system of equations from which the solution describes the SSM and its reduced dynamics. Locating steady states then requires solving a two-dimensional algebraic system of equations, which is practically instantaneous.

The main performance limitation for SSM-based model reduction is not processor speed but memory needs, which depends on the structure of the nonlinearities of the mechanical system. On the positive side, the storage requirements for SSM coefficients can be significantly optimized relative to the proof-of-concept approach presented here. This optimization is an improvement of SSMtool and is currently ongoing work that will be published in the future.

Appendix

3.A Proof of Theorem 3.2

For row i, the $\mathbf{k}^{\text{th}}$-power terms on the right-hand side of Eq. (3.16) can be expressed as

$$[D_{\mathbf{s}}\mathbf{W}_0(\mathbf{s})\mathbf{R}_0(\mathbf{s})]_i^{\mathbf{k}} = \sum_{j=1}^{2} \sum_{\substack{\mathbf{m}\leq\tilde{\mathbf{k}}_j \\ m_j>0}} m_j W_{i,\mathbf{m}}^0 R_{j,\tilde{\mathbf{k}}_j-\mathbf{m}}^0 \tag{3.69}$$

The $\mathbf{k}^{\text{th}}$-power terms on the left-hand side of the i^{th} row of Eq. (3.16) can be written as

$$[\mathbf{\Lambda}\mathbf{W}_0(\mathbf{s})]_i^{\mathbf{k}} = \lambda_i W_{i,\mathbf{k}}^0, \tag{3.70}$$

$$[\mathbf{G}_{\text{m}}(\mathbf{W}_0(\mathbf{s}))]_i^{\mathbf{k}} = [g_i(\mathbf{W}_0(\mathbf{s}))]_{\mathbf{k}}\,. \tag{3.71}$$

where we have made use of the multi-index notation

$$\mathbf{m} \in \mathbb{N}_0^2, \quad \mathbf{k} \in \mathbb{N}_0^2, \quad \tilde{\mathbf{k}}_j = \mathbf{k} + \mathbf{e}_j, \tag{3.72}$$

with $\mathbf{e}_j$ denoting a unit vector.

The coefficient equation related to the $\mathbf{k}^{\text{th}}$-power term of the i^{th} row of the autonomous invariance Eq. (3.16) can now be rewritten as

$$\left(\lambda_i - \sum_{j=1}^{2} k_j \lambda_j\right) W_{i,\mathbf{k}}^0 = \sum_{j=1}^{2} \delta_{ij} R_{j,\mathbf{k}}^0 + Q_{i,\mathbf{k}}, \tag{3.73}$$

where $Q_{i,\mathbf{k}}$ is defined as

$$Q_{i,\mathbf{k}} = \sum_{j=1}^{2} \sum_{\substack{\mathbf{m}\leq\tilde{\mathbf{k}}_j \\ \mathbf{m}\neq\mathbf{e}_j \\ \mathbf{m}\neq\mathbf{k} \\ m_j>0}} m_j W_{i,\mathbf{m}}^0 R_{j,\tilde{\mathbf{k}}_j-\mathbf{m}}^0 - [g_i(\mathbf{W}_0(\mathbf{s}))]_{\mathbf{k}}\,,$$

which proves the result stated in Theorem 3.2.

3.B Proof of Theorem 3.3

Assuming that $\phi \in S^1$, we obtain that for the i^{th} row, the $\mathbf{k}^{\text{th}}$-power terms on the right-hand side of Eq. (3.27) can be expressed as

$$[D_{\mathbf{s}}\mathbf{W}_0(\mathbf{s})\mathbf{R}_1(\mathbf{s},\phi)]_i^{\mathbf{k}} = \sum_{j=1}^{2} \sum_{\substack{\mathbf{m}\leq\tilde{\mathbf{k}}_j \\ m_j>0}} m_j W_{i,\mathbf{m}}^0 R_{j,\tilde{\mathbf{k}}_j-\mathbf{m}}^1(\phi), \tag{3.74}$$

$$[D_{\mathbf{s}}\mathbf{W}_1(\mathbf{s},\phi)\mathbf{R}_0(\mathbf{s})]_i^{\mathbf{k}} = \sum_{j=1}^{2} \sum_{\substack{\mathbf{m}\leq\tilde{\mathbf{k}}_j \\ m_j>0}} m_j W_{i,\mathbf{m}}^1(\phi) R_{j,\tilde{\mathbf{k}}_j-\mathbf{m}}^0, \tag{3.75}$$

$$[D_\phi \mathbf{W}_1(\mathbf{s},\phi)\Omega]_i^{\mathbf{k}} = D_\phi W_{i,\mathbf{k}}^1(\phi)\Omega. \tag{3.76}$$

The $\mathbf{k}^{\text{th}}$-power terms on the left-hand side of the i^{th} row of Eq. (3.27) can be written as

$$[\mathbf{\Lambda}\mathbf{W}_1(\mathbf{s},\phi)]_i^{\mathbf{k}} = \lambda_i W_{i,\mathbf{k}}^1(\phi), \tag{3.77}$$

$$[D_{\mathbf{q}}\mathbf{G}_{\text{m}}(\mathbf{W}_0(\mathbf{s}))\mathbf{W}_1(\mathbf{s},\phi)]_i^{\mathbf{k}} = \left[\sum_{j=1}^{2n} D_{q_j} g_i(\mathbf{W}_0(\mathbf{s})) w_j^1(\mathbf{s},\phi)\right]_{\mathbf{k}}, \tag{3.78}$$

$$[\mathbf{F}_{\text{m}}(\phi)]_i^{\mathbf{k}} = F_{i,\mathbf{k}}(\phi). \tag{3.79}$$

Therefore, the coefficient equation related to the $\mathbf{k}^{\text{th}}$-power term of the i^{th} row of the non-autonomous invariance Eq. (3.27) is

$$\left(\lambda_i - \sum_{j=1}^{2} k_j\lambda_j\right) W_{i,\mathbf{k}}^1(\phi) - D_\phi W_{i,\mathbf{k}}^1(\phi)\Omega = \sum_{j=1}^{2} \delta_{ij} R_{j,\mathbf{k}}^1(\phi) + P_{i,\mathbf{k}}(\phi), \tag{3.80}$$

where

$$\begin{aligned} P_{i,\mathbf{k}}(\phi) = &\sum_{j=1}^{2} \sum_{\substack{\mathbf{m}\leq\tilde{\mathbf{k}}_j \\ \mathbf{m}\neq\mathbf{e}_j \\ m_j>0}} m_j W_{i,\mathbf{m}}^0 R_{j,\tilde{\mathbf{k}}_j-\mathbf{m}}^1(\phi) + \sum_{j=1}^{2} \sum_{\substack{\mathbf{m}\leq\tilde{\mathbf{k}}_j \\ \mathbf{m}\neq\mathbf{k} \\ m_j>0}} m_j W_{i,\mathbf{m}}^1(\phi) R_{j,\tilde{\mathbf{k}}_j-\mathbf{m}}^0 \\ &- F_{i,\mathbf{k}}(\phi) - \left[\sum_{j=1}^{2n} D_{q_j} g_i(\mathbf{W}_0(\mathbf{s})) w_j^1(\mathbf{s},\phi)\right]_{\mathbf{k}}, \end{aligned} \tag{3.81}$$

which concludes the proof of Theorem 3.3.

3.C Proof of Theorem 3.4

The $\mathcal{O}(\varepsilon)$ approximation of the reduced dynamics for $\mathbf{s}$ can be written as

$$\dot{\mathbf{s}} = \mathbf{R}(\mathbf{s}, \phi) = \mathbf{R}_0(\mathbf{s}) + \varepsilon \mathbf{R}_1(\mathbf{s}, \phi), \tag{3.82}$$

where the first row of Eq. (3.82) takes the form

$$\begin{aligned} \dot{s}_1 &= \lambda_1 s_1 + \sum_{i=1}^{M} \gamma_i s_1^{i+1} \bar{s}_1^i \\ &+ \varepsilon \left(c_{1,\mathbf{0}} \mathrm{e}^{\mathrm{i}\phi} + \sum_{i=1}^{M} \left(c_{1,(i,i)}(\Omega) s_1^i \bar{s}_1^i \mathrm{e}^{\mathrm{i}\phi} + d_{1,(i+1,i-1)}(\Omega) s_1^{i+1} \bar{s}_1^{i-1} \mathrm{e}^{-\mathrm{i}\phi} \right) \right), \end{aligned} \tag{3.83}$$

Introducing a change to polar coordinates, $s_1 = \rho \mathrm{e}^{\mathrm{i}\theta}$, $\bar{s}_1 = \rho \mathrm{e}^{-\mathrm{i}\theta}$, dividing by $\mathrm{e}^{\mathrm{i}\theta}$ and introducing the new phase coordinate $\psi = \theta - \phi$, we obtain

$$\begin{aligned} \dot{\rho} + \mathrm{i}\rho(\dot{\psi} + \Omega) &= \lambda_1 \rho + \sum_{i=1}^{M} \gamma_i \rho^{2i+1} \\ &+ \varepsilon \left(c_{1,\mathbf{0}} \mathrm{e}^{-\mathrm{i}\psi} + \sum_{i=1}^{M} \left(c_{1,(i,i)}(\Omega) \rho^{2i} \mathrm{e}^{-\mathrm{i}\psi} + d_{1,(i+1,i-1)}(\Omega) \rho^{2i} \mathrm{e}^{\mathrm{i}\psi} \right) \right). \end{aligned} \tag{3.84}$$

We obtain the result listed in Theorem 3.4 by splitting Eq. (3.84) into its real and imaginary part.

3.D Multivariate recurrence relations

3.D.1 Products

The ith row on the right hand side of the $\mathcal{O}(1)$ coefficient equation can be written as

$$\sum_{j=1}^{2} \partial_{s_j} w_i^0(\mathbf{s}) r_j^0(\mathbf{s}) = \sum_{j=1}^{2} \left(\sum_{\substack{\mathbf{m} \\ m_j > 0}} m_j W_{i,\mathbf{m}}^0 \mathbf{s}^{\mathbf{m}-\mathbf{e}_j} \sum_{\mathbf{n}} R_{j,\mathbf{n}}^0 \mathbf{s}^{\mathbf{n}} \right). \tag{3.85}$$

The $\mathbf{k}$th power coefficient of this resulting product is recursively defined as

$$\left[\sum_{j=1}^{2} \partial_{s_j} w_i^0(\mathbf{s}) r_j^0(\mathbf{s}) \right]_{\mathbf{k}} = \sum_{j=1}^{2} \sum_{\substack{\mathbf{m} \leq \tilde{\mathbf{k}}_j \\ m_j > 0}} m_j W_{i,\mathbf{m}}^0 R_{j,\tilde{\mathbf{k}}_j - \mathbf{m}}^0. \tag{3.86}$$

Example 3.5 To demonstrate how the product in Eq. (3.86) is carried out in SSMtool, we assume that we have the following *arbitrary* polynomial functions for the autonomous SSM and autonomous reduced dynamics, which already has been computed up to order $|\mathbf{k}| = 3$, where $i = 1$,

$$w_1^0(\mathbf{s}) = \alpha s_1^3 + \beta s_1^2 s_2, \quad r_1^0(\mathbf{s}) = \gamma s_2^2 + \delta s_1 s_2, \quad r_2^0(\mathbf{s}) = \varepsilon s_2^2, \tag{3.87}$$

We want to compute the coefficient related to the monomial term $\mathbf{k} = (2, 2)$, which corresponds to order $|\mathbf{k}| = 4$. Using Eq. (3.86), we write

$$\begin{aligned}\left[\sum_{j=1}^{2} \partial_{s_j} w_1^0(\mathbf{s}) r_j^0(\mathbf{s})\right]_{(2,2)} &= \sum_{\substack{\mathbf{m}\leq(3,2)\\ m_1>0}} m_1 W_{1,\mathbf{m}}^0 R_{1,(3,2)-\mathbf{m}}^0 \\ &+ \sum_{\substack{\mathbf{m}\leq(2,3)\\ m_2>0}} m_2 W_{1,\mathbf{m}}^0 R_{2,(2,3)-\mathbf{m}}^0.\end{aligned} \tag{3.88}$$

To increase the efficiency and reduce the total computational time and memory usage, the updated version of SSMtool keeps track of all the non-zero coefficients in $w_1^0(\mathbf{s})$, $r_1^0(\mathbf{s})$ and $r_2^0(\mathbf{s})$. This way, instead of carrying out the full summations in Eq. (3.86), we can selectively carry out the products from which we know in advance that these terms will give a contribution to the current coefficient of interest. The entries of the non-zero coefficients for each polynomial function are listed in an individual vector and stored in MATLAB,

$$W_{1,\text{index}}^0 = \begin{bmatrix}(3,0)\\(2,1)\end{bmatrix}, \quad R_{1,\text{index}}^0 = \begin{bmatrix}(0,2)\\(1,1)\end{bmatrix}, \quad R_{2,\text{index}}^0 = \begin{bmatrix}(0,2)\end{bmatrix}. \tag{3.89}$$

From this we conclude that for the first summation term on the right hand side of Eq. (3.88), the absolute maximum number of iterations that we possibly have to perform are two, related to the terms $\mathbf{m} = (3, 0)$ and $\mathbf{m} = (2, 1)$, as these are the only currently non-zero terms in $w_1^0(\mathbf{s})$. Depending on the non-zero coefficients of the reduced dynamics, the number of iterations needed either remains the same or decreases. The coefficients, related to $r_1^0(\mathbf{s})$, that are needed in the summation are

$$R_{1,(3,2)-(3,0)}^0 = R_{1,(0,2)}^0, \quad R_{1,(3,2)-(2,1)}^0 = R_{1,(1,1)}^0, \tag{3.90}$$

which both are non-zero in this particular example. Therefore, we can write

$$\begin{aligned}\sum_{\substack{\mathbf{m}\leq(3,2)\\ m_1>0}} m_1 W_{1,\mathbf{m}}^0 R_{1,(3,2)-\mathbf{m}}^0 &= 3W_{1,(3,0)}^0 R_{1,(0,2)}^0 + 2W_{1,(2,1)}^0 R_{1,(1,1)}^0 \\ &= 3\alpha\gamma + 2\beta\delta.\end{aligned} \tag{3.91}$$

For the second summation term on the right hand side of Eq. (3.88), the maximum number of iterations that we possibly have to perform is one, corresponding to $\mathbf{m} = (2,1)$, as it is required that $m_2 > 0$, which is not the case for $\mathbf{m} = (3,0)$. Again, depending on the coefficients of the reduced dynamics, it is possible that less iterations are needed. The coefficients, related to $r_2^0(\mathbf{s})$, that are needed in the summation are

$$R^0_{2,(2,3)-(2,1)} = R^0_{2,(0,2)}, \tag{3.92}$$

which is non-zero in this particular example. We can express the second summation term on the right hand side of Eq. (3.88) as

$$\sum_{\substack{\mathbf{m}\leq(2,3)\\ m_2>0}} m_2 W^0_{1,\mathbf{m}} R^0_{2,(2,3)-\mathbf{m}} = W^0_{1,(2,1)} R^0_{2,(0,2)} = \beta\varepsilon. \tag{3.93}$$

Therefore, the coefficient related to the term $\mathbf{k} = (2,2)$ of the product $\sum_{j=1}^{2} \partial_{s_j} w_1^0(\mathbf{s}) r_j^0(\mathbf{s})$, is equal to

$$\left[\sum_{j=1}^{2} \partial_{s_j} w_1^0(\mathbf{s}) r_j^0(\mathbf{s})\right]_{(2,2)} = 3\alpha\gamma + 2\beta\delta + \beta\varepsilon. \tag{3.94}$$

For verification, we manually compute the product

$$\sum_{j=1}^{2} \partial_{s_j} w_1^0(\mathbf{s}) r_j^0(\mathbf{s}) = (3\alpha\gamma + 2\beta\delta + \beta\varepsilon)\, s_1^2 s_2^2 + \mathcal{O}(|\mathbf{s}|^4). \tag{3.95}$$

which agrees with our result.

3.D.2 Compositions

The ith row of the composition on the left hand side of Eq. (3.16) can be written as

$$h(\mathbf{s})_a = \sum_{\mathbf{k}} H_{a,\mathbf{k}} \mathbf{s}^{\mathbf{k}} = (w_i^0(\mathbf{s}))^a = \left(\sum_{\mathbf{m}} W^0_{i,\mathbf{m}} \mathbf{s}^{\mathbf{m}}\right)^a. \tag{3.96}$$

We want to obtain the coefficient related to the term $\mathbf{k} \neq 0$ of this composition. We pick an index j, such that $k_j = \min(k_l : k_l \neq 0)$ and differentiate Eq. (3.96) with respect to s_j, yielding

$$\partial_{s_j} h(\mathbf{s}) = a(w_i^0(\mathbf{s}))^{a-1} \partial_{s_j} w_i^0(\mathbf{s}) = a h(\mathbf{s})_{a-1} \partial_{s_j} w_i^0(\mathbf{s}), \tag{3.97}$$

which is equivalent to

$$\sum_{\substack{\mathbf{k}\\ k_j>0}} k_j H_{a,\mathbf{k}} \mathbf{s}^{\mathbf{k}-\mathbf{e}_j} = a \sum_{\mathbf{n}} H_{a-1,\mathbf{n}} \mathbf{s}^{\mathbf{n}} \sum_{\substack{\mathbf{m}\\ m_j>0}} m_j W^0_{i,\mathbf{m}} \mathbf{s}^{\mathbf{m}-\mathbf{e}_j}. \tag{3.98}$$

Collecting the coefficient corresponding to the monomial term $\mathbf{s}^{\mathbf{k}-\mathbf{e}_j}$ on each side of Eq. (3.98) yields the coefficient related to the $\mathbf{k} \neq 0$ term of Eq. (3.96),

$$H_{a,\mathbf{k}} = \frac{a}{k_j} \sum_{\substack{\mathbf{m} \leq \mathbf{k} \\ m_j > 0}} m_j W^0_{i,\mathbf{m}} H_{a-1,\mathbf{k}-\mathbf{m}}. \tag{3.99}$$

Example 3.6 We give an demonstration of Eq (3.99), where we will use the same polynomial function $w_1^0(\mathbf{s})$ as in Example 3.5,

$$w_1^0(\mathbf{s}) = \alpha s_1^3 + \beta s_1^2 s_2. \tag{3.100}$$

Assume we are interested in the coefficient related to the monomial term $\mathbf{k} = (5, 1)$ of the square of $w_1^0(\mathbf{s})$, i.e. where $a = 2$. We choose $j = 2$ such that we minimize the number of iterations needed. Then using Eq. (3.99) we can write

$$H_{2,(5,1)} = \frac{2}{1} \sum_{\substack{\mathbf{m} \leq (5,1) \\ m_2 > 0}} m_2 W^0_{1,\mathbf{m}} H_{1,(5,1)-\mathbf{m}}, \tag{3.101}$$

where we note that $H_{1,\mathbf{m}}$ is equal to $W^0_{1,\mathbf{m}}$. The entries of the non-zero coefficients for $w_1^0(\mathbf{s})$ are listed in an individual vector,

$$W^0_{1,\text{index}} = \begin{bmatrix} (3,0) \\ (2,1) \end{bmatrix}. \tag{3.102}$$

From this we conclude that the absolute maximum number of iterations that we possibly have to perform are two, related to the terms $\mathbf{m} = (3, 0)$ and $\mathbf{m} = (2, 1)$, as these are the only currently non-zero terms in $w_1^0(\mathbf{s})$. However, taking a closer look, we obverse that for $\mathbf{m} = (3, 0)$, $m_2 = 0$, and therefore this index is excluded from the summation. Summing over the remaining index $\mathbf{m} = (2, 1)$, we obtain

$$H_{2,(5,1)} = \frac{2}{1} \sum_{\substack{\mathbf{m} \leq (5,1) \\ m_2 > 0}} m_2 W^0_{1,\mathbf{m}} W^0_{1,(5,1)-\mathbf{m}} = 2\alpha\beta. \tag{3.103}$$

To verify this result, we manually compute the square of $w_1^0(\mathbf{s})$,

$$(w_1^0(\mathbf{s}))^2 = 2\alpha\beta s_1^5 s_2 + \mathcal{O}(|\mathbf{s}|^6). \tag{3.104}$$

3.E A geometric interpretation of the fixed points of the reduced dynamics

We can interpret the zero problem (3.48) in a geometrical way by multiplying $F_1(\mathbf{u})$ and $F_2(\mathbf{u})$ with $g_1 \neq 0$ and $f_2 \neq 0$, respectively, and rewriting the result as

$$\begin{aligned}\mathbf{s}(\rho,\Omega,\psi) &= \underbrace{\begin{bmatrix}\cos(\psi) & \sin(\psi)\\ -\sin(\psi) & \cos(\psi)\end{bmatrix}}_{\mathbf{R}(\psi)}\underbrace{\begin{bmatrix}f_2 g_2\\ f_2 g_1\end{bmatrix}}_{\mathbf{v}_1} + \underbrace{\begin{bmatrix}f_1 g_1 - f_2 g_2\\ 0\end{bmatrix}}_{\mathbf{v}_2}\cos(\psi) \\ &= \underbrace{-\frac{1}{\varepsilon}\begin{bmatrix}g_1 a\\ f_2(b-\Omega)\rho\end{bmatrix}}_{\mathbf{v}_3},\end{aligned} \tag{3.105}$$

where we introduced the rotation matrix $\mathbf{R}(\psi) \in \mathrm{SO}(2)$. For a fixed value of ρ_0, Ω_0 and $0 \leq \psi < 2\pi$, $\mathbf{s}(\rho_0,\Omega_0,\psi)$ represents an ellipse with semi-major and semi-minor axes, $\|\mathbf{s}(\rho_0,\Omega_0,\psi_1)\|$ and $\|\mathbf{s}(\rho_0,\Omega_0,\psi_2)\|$, respectively, where

$$\psi_1 = \arg\max_{0\leq\psi\leq\pi} \|\mathbf{s}(\rho_0,\Omega_0,\psi)\|, \quad \psi_2 = \arg\min_{0\leq\psi\leq\pi} \|\mathbf{s}(\rho_0,\Omega_0,\psi)\|.$$

We can always solve Eq. (3.105) by scaling the length of $\mathbf{v}_3$ (varying ε) such that $\mathbf{v}_3$ points to a point on the ellipse $\mathbf{s}(\rho_0,\Omega_0,\psi)$. This intersection point then defines a ψ value for which Eq. (3.105) is satisfied. Each point where $\mathbf{s}$ and $\mathbf{v}_3$ coincide for different values of ρ gives a point on the forced-response curve. An illustration of this concept is shown in Fig. 3.E.1, where $\mathbf{v}_3$ intersects $\mathbf{s}$ a total of three times for increasing ρ. These three intersections correspond to three points on the forced-response curve for a fixed forcing frequency Ω and fixed forcing amplitude ε.

We will show that for a mechanical system with symmetric system matrices and with structural damping, we can always pick a modal transformation matrix $\mathbf{T}$, such that g_1 and f_2 will have a non-zero constant part.

As seen in Eq. (3.36), the zeroth-order constant, $c_{1,\mathbf{0}}$, is equal to the first element of the vector $\tilde{\mathbf{F}}_{\mathbf{0}}/2$, which is extracted from the modal force vector

$$\mathbf{F}_{\mathrm{m}}(\phi) = \tilde{\mathbf{T}}^{-1}\begin{bmatrix}\mathbf{0}\\ \mathbf{M}^{-1}\mathbf{f}(\phi)\end{bmatrix} = \frac{\tilde{\mathbf{F}}_{\mathbf{0}}}{2}\left(\mathrm{e}^{\mathrm{i}\phi} + \mathrm{e}^{-\mathrm{i}\phi}\right). \tag{3.106}$$

For a mechanical system with symmetric system matrices and with structural damping, following [8], we introduce a mass normalized real modal transformation matrix $\mathbf{E}$, defined in terms of the quantities in the second-order system (3.1) as follows:

$$\begin{gathered}(\mathbf{M}^{-1}\mathbf{K})\mathbf{E} = \mathbf{E}\ \mathrm{diag}(\omega_1^2,\ldots,\omega_n^2),\\ \mathbf{E}^{\top}\mathbf{M}\mathbf{E} = \mathbf{I}, \quad \mathbf{E}^{\top}\mathbf{C}\mathbf{E} = \mathrm{diag}(\beta_1,\ldots,\beta_n), \quad \mathbf{E}^{\top}\mathbf{K}\mathbf{E} = \mathrm{diag}(\omega_1^2,\ldots,\omega_n^2),\end{gathered}$$

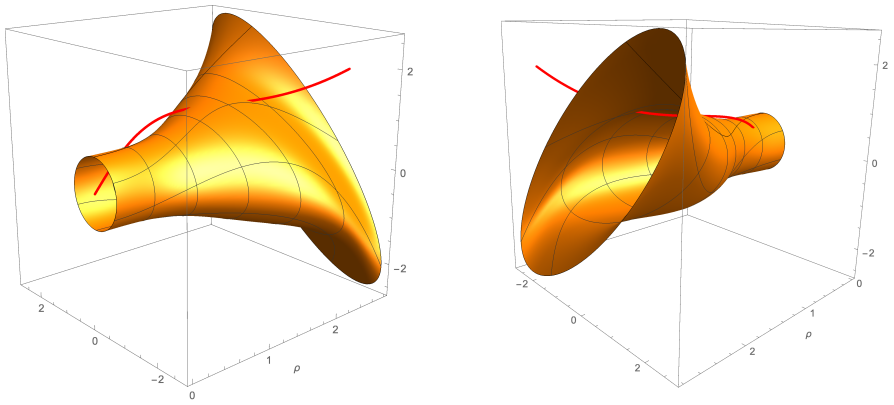

Figure 3.E.1: Illustration of $\mathbf{s}(\rho, \Omega, \psi)$ and $\mathbf{v}_3$ for a fixed forcing frequency Ω, $\psi \in [0, 2\pi)$, while varying ρ. The points where $\mathbf{s}(\rho, \Omega, \psi)$ and $\mathbf{v}_3$ coincide for different values of ρ will each correspond to a point on the forced-response curve.

Here the eigenvalues of the linearized part of system (3.2) are given by

$$\lambda_{2i-1} = -\frac{\beta_i}{2} + \sqrt{\left(\frac{\beta_i}{2}\right)^2 - \omega_i^2}, \quad \lambda_{2i} = -\frac{\beta_i}{2} - \sqrt{\left(\frac{\beta_i}{2}\right)^2 - \omega_i^2}, \quad i = 1, \ldots, n. \tag{3.107}$$

We now introduce the modal transformation matrix $\hat{\mathbf{T}}$ that will diagonalize the linear matrix $\mathbf{A}$ in (3.2), i.e., we let

$$\hat{\mathbf{T}} = \begin{bmatrix} \mathbf{E} & \mathbf{E} \\ \mathbf{E}\boldsymbol{\Lambda}_1 & \mathbf{E}\boldsymbol{\Lambda}_2 \end{bmatrix}, \quad \hat{\boldsymbol{\Lambda}} = \hat{\mathbf{T}}^{-1}\mathbf{A}\hat{\mathbf{T}} = \begin{bmatrix} \boldsymbol{\Lambda}_1 & \mathbf{0} \\ \mathbf{0} & \boldsymbol{\Lambda}_2 \end{bmatrix} \tag{3.108}$$
$$\boldsymbol{\Lambda}_1 = \operatorname{diag}(\lambda_1, \lambda_3, \ldots, \lambda_{2n-1}), \quad \boldsymbol{\Lambda}_2 = \operatorname{diag}(\lambda_2, \lambda_4, \ldots, \lambda_{2n}) = \bar{\boldsymbol{\Lambda}}_1.$$

The inverse of the modal transformation matrix $\hat{\mathbf{T}}$ is given by

$$\hat{\mathbf{T}}^{-1} = \begin{bmatrix} \mathbf{E}^{-1} + (\boldsymbol{\Lambda}_2 - \boldsymbol{\Lambda}_1)^{-1}\mathbf{E}^{-1}\boldsymbol{\Lambda}_1\mathbf{E}^{-1} & -(\boldsymbol{\Lambda}_2 - \boldsymbol{\Lambda}_1)^{-1}\mathbf{E}^{-1} \\ (\boldsymbol{\Lambda}_2 - \boldsymbol{\Lambda}_1)^{-1}\mathbf{E}^{-1}\boldsymbol{\Lambda}_1\mathbf{E}^{-1} & (\boldsymbol{\Lambda}_2 - \boldsymbol{\Lambda}_1)^{-1}\mathbf{E}^{-1} \end{bmatrix}. \tag{3.109}$$

We observe that the last n columns of $\hat{\mathbf{T}}^{-1}$ are purely imaginary. Note that the current ordering of the columns of $\hat{\mathbf{T}}$, will result in a diagonalized matrix $\hat{\boldsymbol{\Lambda}}$ with a different column ordering as compared to $\boldsymbol{\Lambda}$ in (3.5). However, we can always reorder the columns of $\hat{\mathbf{T}}$ to $\tilde{\mathbf{T}}$ such that we obtain the original diagonalized matrix $\boldsymbol{\Lambda}$, without altering the fact that the last n columns of $\tilde{\mathbf{T}}^{-1}$ will be imaginary. This is due to the fact that a reordering of the columns of a full rank matrix $\mathbf{P}$, will result in a reordering of the rows of $\mathbf{P}^{-1}$, but not the columns of $\mathbf{P}^{-1}$.

As a result, the vector $\tilde{\mathbf{F}}_{\mathbf{0}}$ will be purely imaginary as can be seen from Eq. (3.106), and, consequently, the zeroth order constant $c_{1,\mathbf{0}}$ in (3.36) will be purely imaginary. Additionally, the first n rows of $\tilde{\mathbf{T}}$ are real (as $\tilde{\mathbf{T}}$ is only a column shifted version of $\hat{\mathbf{T}}$), meaning that the if we map a fixed point for the reduced system back to the full phase space, we observe that the leading order linear term in ρ, corresponding to a positional coordinate y_i of the full system, will have a phase shift of ψ with respect to the forcing, i.e.

$$\begin{aligned} y_i &= [\tilde{\mathbf{T}}]_{i,1}\rho \mathrm{e}^{\mathrm{i}(\phi+\psi)} + [\tilde{\mathbf{T}}]_{i,2}\rho \mathrm{e}^{-\mathrm{i}(\phi+\psi)} + \mathcal{O}(|\rho|^2,\varepsilon) \\ &= [\tilde{\mathbf{T}}]_{i,1}\rho \left(\mathrm{e}^{\mathrm{i}(\phi+\psi)} + \mathrm{e}^{-\mathrm{i}(\phi+\psi)}\right) + \mathcal{O}(|\rho|^2,\varepsilon), \quad i = 1,\ldots,n, \end{aligned}$$

provided that $[\tilde{\mathbf{T}}]_{i,1} = [\tilde{\mathbf{T}}]_{i,2} \neq 0$. No additional phase is introduced by the coefficients of the modal transformation matrix for the positional coordinates y_i, as all the coefficients are real.

In the setting of Breunung and Haller [8], where the parameterization $\mathbf{W}(\mathbf{s},\phi)$ and the reduced dynamics $\mathbf{R}(\mathbf{s},\phi)$ are truncated at $\mathcal{O}(\varepsilon|\mathbf{s}|,\varepsilon^2)$, which is justified when $\mathbf{s} = \mathcal{O}(\varepsilon^{\frac{1}{2M+2}})$, the zero problem (3.48) can be written as

$$\begin{aligned} \tilde{\mathbf{F}}(\mathbf{u}) &= \begin{bmatrix} \tilde{F}_1(\mathbf{u}) \\ \tilde{F}_2(\mathbf{u}) \end{bmatrix} \\ &= \begin{bmatrix} a(\rho) + \varepsilon\left(\mathrm{Re}(c_{1,\mathbf{0}})\cos(\psi) + \mathrm{Im}(c_{1,\mathbf{0}})\sin(\psi)\right) \\ (b(\rho)-\Omega)\rho + \varepsilon\left(\mathrm{Im}(c_{1,\mathbf{0}})\cos(\psi) - \mathrm{Re}(c_{1,\mathbf{0}})\sin(\psi)\right) \end{bmatrix} = \mathbf{0}. \end{aligned} \tag{3.110}$$

The ellipse $\mathbf{s}$ reduces to a circle

$$\underbrace{\begin{bmatrix} \cos(\psi) & \sin(\psi) \\ -\sin(\psi) & \cos(\psi) \end{bmatrix}}_{\mathbf{R}(\psi)} \underbrace{\begin{bmatrix} \mathrm{Re}(c_{1,\mathbf{0}}) \\ \mathrm{Im}(c_{1,\mathbf{0}}) \end{bmatrix}}_{\mathbf{v}_1} = \underbrace{-\frac{1}{\varepsilon}\begin{bmatrix} a(\rho) \\ (b(\rho)-\Omega)\rho \end{bmatrix}}_{\mathbf{v}_2}. \tag{3.111}$$

In their setting, at the intersection of the FRC with the autonomous backbone curve, i.e., where $b(\rho)-\Omega = 0$, the vectors $\mathbf{v}_1$ and $\mathbf{v}_2$ are orthogonal with respect to each other, due to the fact the real part of $c_{1,\mathbf{0}}$ is zero. Therefore, the phase shift ψ will be equal to $\pi/2$.

Chapter 4

Analytic Prediction of Isolated FRCs from SSMs

Introduction

We show how spectral submanifold (SSM) theory can be used to provide analytic predictions for the response of periodically forced multi-degree-of-freedom mechanical systems. These predictions include an explicit criterion for the existence of isolated forced responses that will generally be missed by numerical continuation techniques. Our analytic predictions can be refined to arbitrary precision via an algorithm that does not require the numerical solutions of the mechanical system. We illustrate all these results on low- and high-dimensional nonlinear vibration problems. We find that our SSM-based forced-response predictions remain accurate in high-dimensional systems, in which numerical continuation of the periodic response is becoming computationally expensive.

4.1 Introduction

For an n-degree-of-freedom, periodically forced, nonlinear mechanical system, the forced response curve (FRC) gives the amplitude of the periodic response of the system as a function of the frequency of the periodic forcing. The FRC may contain isolated branches of periodic solutions, also known as *isolas*, that are detached from the main FRC. A small change in the forcing amplitude might result in the merger of the isola with the main branch of the FRC (cf. Detroux et al. [69] and Noël et al. [70]), which can lead to an unexpected and significant increase in the response amplitude.

The existence of isolated branches of periodic solutions in the frequency response of nonlinear oscillatory systems has been known since the 1950s [71]. For an extensive review of the subject, we refer the reader to Habib et al. [72]. It is broadly agreed that the identification of isolas is difficult, because numerical continuation techniques are generally initiated on a non-isolated solution branch and will there-

fore miss any isolated branch. Similarly, a frequency sweep of the full system will generally not capture an isolated response unless the sweep is initialized on one.

The detection of isolas and the prediction of their behavior under changing system parameters can be critical in practice because, their merger with the main FRC may lead to a dramatic shift in the resonance frequency and response amplitude. Habib et al. [72] use singularity theory in combination with averaging for the prediction and identification of isolas in a specific single-degree-of-freedom mechanical system with nonlinear damping. The averaging method they use (cf. Sanders et al. [73]), however, requires both the forcing amplitude and the nonlinear damping coefficients to be small. Hill et al. [74] use a second-order normal form technique to obtain analytical expressions for the autonomous conservative backbone curves (i.e. amplitude-frequency plots of nonlinear periodic orbits) of a specific two-degree-of-freedom mechanical system. They give leading-order criteria for the intersection of this backbone curve with the forced response curve and postulate this location to be a potential starting point for an isola, which is to be constructed numerically in a separate effort. This procedure also relies on the smallness of the nonlinear and damping coefficients, as well as on the absence of quadratic nonlinearities.

In summary, while the significance of isolas is broadly recognized, their existence has only been studied in specific, low-dimensional examples under restrictions on the nonlinearities. A conclusive analytical criterion for predicting isolas in multi-degree of freedom systems without costly numerical simulations, therefore, has been unavailable.

In this work, we seek to fill this gap by developing a generally applicable methodology for the prediction of isolas in multi-degree-of-freedom, forced mechanical systems. Our approach is based on the mathematically rigorous theory of spectral submanifolds (SSMs) that are the unique, smoothest, nonlinear continuations of spectral subspaces of the linearized, unforced limit of a mechanical system (cf. Haller and Ponsioen [4]). The reduced dynamics on a two-dimensional SSM serves as an exact, single-degree-of-freedom reduced-order model that can be constructed for each vibration mode of the full nonlinear system (cf. [6, 8, 16, 52, 51]).

By construction, these rigorously, simplified two-dimensional reduced models will capture all isolas that are remnants of periodic orbit families of the conservative limit of the system. As we show for a cubic-order approximation, the reduced SSM dynamics gives a closed form first-order prediction for isolas that can even be calculated by hand in simple examples. Higher-order refinements to this analytic formula can be recursively constructed and have been implemented in the publicly available MATLAB script SSMtool[1]. We show the use of the analytic formula as well as its numerical refinements on simple and more complicated examples.

[1] SSMtool is available at: www.georgehaller.com

4.2 System set-up

We consider the same system set-up as introduced in section 3.2, which we restate for the sake of readability. Where we have n-degree-of-freedom, periodically forced mechanical systems of the form

$$\begin{aligned} \mathbf{M}\ddot{\mathbf{y}} + \mathbf{C}\dot{\mathbf{y}} + \mathbf{K}\mathbf{y} + \mathbf{g}(\mathbf{y}, \dot{\mathbf{y}}) = \varepsilon \mathbf{f}(\Omega t), \quad 0 \leq \varepsilon \ll 1, \\ \mathbf{g}(\mathbf{y}, \dot{\mathbf{y}}) = \mathcal{O}\left(|\mathbf{y}|^2, |\mathbf{y}|\,|\dot{\mathbf{y}}|, |\dot{\mathbf{y}}|^2 \right), \end{aligned} \tag{4.1}$$

where $\mathbf{y} \in \mathbb{R}^n$ is the generalized position vector; $\mathbf{M} = \mathbf{M}^T \in \mathbb{R}^{n\times n}$ is the positive definite mass matrix; $\mathbf{C} = \mathbf{C}^T \in \mathbb{R}^{n\times n}$ is the damping matrix; $\mathbf{K} = \mathbf{K}^T \in \mathbb{R}^{n\times n}$ is the stiffness matrix and $\mathbf{g}(\mathbf{y}, \dot{\mathbf{y}})$ denotes all the nonlinear terms in the system. These nonlinearities are assumed to be analytic for simplicity. The external forcing $\varepsilon\mathbf{f}(\Omega t)$ does not depend on the positions and velocities.

System (4.1) can be transformed into a set of $2n$ first-order ordinary differential equations by introducing the change of variables $\mathbf{x}_1 = \mathbf{y}$, $\mathbf{x}_2 = \dot{\mathbf{y}}$, with $\mathbf{x} = (\mathbf{x}_1, \mathbf{x}_2) \in \mathbb{R}^{2n}$, which gives

$$\begin{aligned} \dot{\mathbf{x}} &= \begin{pmatrix} \mathbf{0} & \mathbf{I} \\ -\mathbf{M}^{-1}\mathbf{K} & -\mathbf{M}^{-1}\mathbf{C} \end{pmatrix} \mathbf{x} + \begin{pmatrix} \mathbf{0} \\ -\mathbf{M}^{-1}\mathbf{g}(\mathbf{x}_1, \mathbf{x}_2) \end{pmatrix} + \varepsilon \begin{pmatrix} \mathbf{0} \\ \mathbf{M}^{-1}\mathbf{f}(\Omega t) \end{pmatrix} \\ &= \mathbf{A}\mathbf{x} + \mathbf{G}_{\mathrm{p}}(\mathbf{x}) + \varepsilon \mathbf{F}_{\mathrm{p}}(\Omega t). \end{aligned} \tag{4.2}$$

The transformed first-order system (4.2) has a fixed point at $\mathbf{x} = \mathbf{0}$ when the system is unforced ($\varepsilon = 0$); $\mathbf{A} \in \mathbb{R}^{2n\times 2n}$ is a constant matrix and $\mathbf{G}_{\mathrm{p}}(\mathbf{x})$ is an analytic function containing all the nonlinearities.

The linearized part of system (4.2) is

$$\dot{\mathbf{x}} = \mathbf{A}\mathbf{x}, \tag{4.3}$$

where the matrix $\mathbf{A}$ has $2n$ eigenvalues $\lambda_k \in \mathbb{C}$ for $k = 1, \ldots, 2n$. Counting multiplicities, we again sort these eigenvalues based on their real parts in the decreasing order

$$\mathrm{Re}(\lambda_{2n}) \leq \mathrm{Re}(\lambda_{2n-1}) \leq \ldots \leq \mathrm{Re}(\lambda_1) < 0, \tag{4.4}$$

assuming that the real part of each eigenvalue is less than zero and hence the fixed point of Eq. (4.3) is asymptotically stable. We further assume that the constant matrix $\mathbf{A}$ is semisimple.

4.3 Extracting the forced-response curve

Because $\mathbf{A}$ is semisimple, the linear part of system (4.2) is diagonalized by a linear change of coordinates $\mathbf{x} = \mathbf{T}\mathbf{q}$, with $\mathbf{T} = [\mathbf{v}_1, \mathbf{v}_2, \ldots, \mathbf{v}_{2n}] \in \mathbb{C}^{2n\times 2n}$ and $\mathbf{q} \in \mathbb{C}^{2n}$, yielding

$$\dot{\mathbf{q}} = \underbrace{\operatorname{diag}(\lambda_1, \lambda_2 \ldots, \lambda_{2n})}_{\mathbf{\Lambda}} \mathbf{q} + \mathbf{G}_{\mathrm{m}}(\mathbf{q}) + \varepsilon \mathbf{F}_{\mathrm{m}}(\boldsymbol{\phi}). \tag{4.5}$$

We now consider the two-dimensional modal subspace $\mathcal{E} = \operatorname{span}\{\mathbf{v}_1, \mathbf{v}_2\} \subset \mathbb{C}^{2n}$ with $\mathbf{v}_2 = \bar{\mathbf{v}}_1$. The remaining linearly independent eigenvectors $\mathbf{v}_3, \ldots, \mathbf{v}_{2n}$ span a complex subspace $\mathcal{C} \subset \mathbb{C}^{2n}$ such that the full phase space of (4.5) can be expressed as the direct sum

$$\mathbb{C}^{2n} = \mathcal{E} \oplus \mathcal{C}. \tag{4.6}$$

We write the diagonal matrix $\mathbf{\Lambda}$ as

$$\mathbf{\Lambda} = \begin{bmatrix} \mathbf{\Lambda}_{\mathcal{E}} & 0 \\ 0 & \mathbf{\Lambda}_{\mathcal{C}} \end{bmatrix}, \tag{4.7}$$
$$\operatorname{Spect}(\mathbf{\Lambda}_{\mathcal{E}}) = \{\lambda_1, \lambda_2\}, \quad \operatorname{Spect}(\mathbf{\Lambda}_{\mathcal{C}}) = \{\lambda_3, \ldots, \lambda_{2n}\},$$

with $\mathbf{\Lambda}_{\mathcal{E}} = \operatorname{diag}(\lambda_1, \lambda_2)$ and $\mathbf{\Lambda}_{\mathcal{C}} = \operatorname{diag}(\lambda_3, \ldots, \lambda_{2n})$.

Under the non-resonance conditions stated in (3.9), there exists a unique two-dimensional, time-periodic, analytic SSM $\mathcal{W}(\mathcal{E})$, which perturbs smoothly from $\mathcal{E}$ at the trivial fixed point $\mathbf{q} = 0$, under the addition of the $\mathcal{O}(\varepsilon)$ terms in Eq. (4.5). Additionally, $\mathcal{W}(\mathcal{E})$ is strictly smoother than any other invariant manifold with the same properties.

We give an illustration of a time-periodic SSM in Fig. 4.1. We have assumed a case in which the SSM has three limit cycles for a given forcing frequency, with two of these limit cycles contained in an isola. The SSM approach can be viewed as a refinement and extension of the seminal work of Shaw and Pierre [2], who envision nonlinear normal modes as invariant manifolds that are locally graphs over two-dimensional modal subspaces of the linearized system.

We recall that the dynamics on the SSM described in Theorem 3.1 can approximately be written in polar coordinates (ρ, ψ) as

$$\dot{\rho} = a(\rho) + \varepsilon \left(f_1(\rho, \Omega) \cos(\psi) + f_2(\rho, \Omega) \sin(\psi) \right), \tag{4.8}$$
$$\dot{\psi} = (b(\rho) - \Omega) + \frac{\varepsilon}{\rho} \left(g_1(\rho, \Omega) \cos(\psi) - g_2(\rho, \Omega) \sin(\psi) \right), \tag{4.9}$$

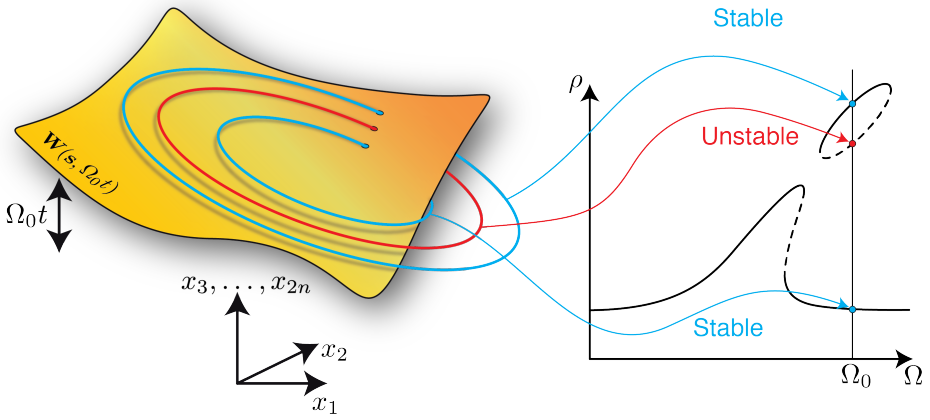

Figure 4.1: Illustration of a time-periodic SSM. For a given forcing frequency Ω, we illustrate how the SSM may contain three limit cycles, of which two fall in an isola.

where

$$a(\rho) = \mathrm{Re}(\lambda_1)\rho + \sum_{i=1}^{M} \mathrm{Re}(\gamma_i)\rho^{2i+1}, \tag{4.10}$$

$$b(\rho) = \mathrm{Im}(\lambda_1) + \sum_{i=1}^{M} \mathrm{Im}(\gamma_i)\rho^{2i}, \tag{4.11}$$

and

$$f_1(\rho,\Omega) = \mathrm{Re}(c_{1,\mathbf{0}}) + \sum_{i=1}^{M} \left(\mathrm{Re}(c_{1,(i,i)}(\Omega)) + \mathrm{Re}(d_{1,(i+1,i-1)}(\Omega))\right)\rho^{2i}, \tag{4.12}$$

$$f_2(\rho,\Omega) = \mathrm{Im}(c_{1,\mathbf{0}}) + \sum_{i=1}^{M} \left(\mathrm{Im}(c_{1,(i,i)}(\Omega)) - \mathrm{Im}(d_{1,(i+1,i-1)}(\Omega))\right)\rho^{2i}, \tag{4.13}$$

$$g_1(\rho,\Omega) = \mathrm{Im}(c_{1,\mathbf{0}}) + \sum_{i=1}^{M} \left(\mathrm{Im}(c_{1,(i,i)}(\Omega)) + \mathrm{Im}(d_{1,(i+1,i-1)}(\Omega))\right)\rho^{2i}, \tag{4.14}$$

$$g_2(\rho,\Omega) = \mathrm{Re}(c_{1,\mathbf{0}}) + \sum_{i=1}^{M} \left(\mathrm{Re}(c_{1,(i,i)}(\Omega)) - \mathrm{Re}(d_{1,(i+1,i-1)}(\Omega))\right)\rho^{2i}, \tag{4.15}$$

with $2M+1$ denoting the order of the expansion.

In the unforced limit ($\varepsilon = 0$), the reduced system (4.8)-(4.9) can have fixed points but no nontrivial periodic orbits. This is because (4.8) decouples from (4.9), rep-

resenting a one-dimensional ordinary differential equation that cannot have non-constant periodic solutions. By construction, the trivial fixed point of (4.8)-(4.9) is asymptotically stable and will persist for $\varepsilon > 0$. These persisting fixed points satisfy the system of equations

$$\mathbf{F}(\mathbf{u}) = \begin{bmatrix} F_1(\mathbf{u}) \\ F_2(\mathbf{u}) \end{bmatrix} = \begin{bmatrix} a(\rho) + \varepsilon \left(f_1(\rho, \Omega)\cos(\psi) + f_2(\rho, \Omega)\sin(\psi) \right) \\ (b(\rho) - \Omega)\rho + \varepsilon \left(g_1(\rho, \Omega)\cos(\psi) - g_2(\rho, \Omega)\sin(\psi) \right) \end{bmatrix} = \mathbf{0}, \tag{4.16}$$

where

$$\mathbf{F}(\mathbf{u}) : \mathbb{R}^3 \to \mathbb{R}^2, \quad \mathbf{u} = \begin{bmatrix} \rho \\ \Omega \\ \psi \end{bmatrix}.$$

As we show in Appendix 4.A, under appropriate non-degeneracy conditions, the zeros of (4.16) form a one-dimensional manifold, which, after a projection onto the amplitude-frequency space, will represent the FRC. The stability of these fixed points (which correspond to periodic solutions of the full mechanical system) is determined by the real parts of the eigenvalues of the Jacobian of $\mathbf{F}(\mathbf{u})$.

Theorem 4.1 *The amplitude ρ of the T-periodic orbits of the reduced dynamics (4.8)-(4.9) are given by the zeros of the function*

$$\begin{aligned} G(\rho; \Omega) = {} & (b(\rho) - \Omega)\rho \\ & + \varepsilon \left(g_1(\rho, \Omega) \frac{1 - K^{\pm}(\rho; \Omega)^2}{1 + K^{\pm}(\rho; \Omega)^2} - g_2(\rho, \Omega) \frac{2K^{\pm}(\rho; \Omega)}{1 + K^{\pm}(\rho; \Omega)^2} \right) = 0, \end{aligned} \tag{4.17}$$

where

$$K^{\pm}(\rho; \Omega) = \frac{-\varepsilon f_2(\rho, \Omega) \pm \sqrt{\varepsilon^2 \left(f_1(\rho, \Omega)^2 + f_2(\rho, \Omega)^2 \right) - a(\rho)^2}}{a(\rho) - \varepsilon f_1(\rho, \Omega)}. \tag{4.18}$$

Proof We derive this result in Appendix 4.B.

The zero-level set of Eq. (4.17) yields the forced-response curve in the (Ω, ρ)-space. This curve will consist of two segments obtained from K^+ and K^- in Eq. (4.18). The two segments meet exactly at the point where the square root term in the definition of $K^{\pm}(\rho; \Omega)$ is equal to zero. We sketch this for a damped, nonlinear, periodically forced mechanical system in Fig. 4.2.

Because the isolated branches of periodic solutions are also a part of the FRC, the zero-level set of $G(\rho; \Omega)$ can predict isolas as well. In contrast, detecting isolas by numerical continuation requires one to start on the isola and hence assumes a priori knowledge of an isolated branch of periodic solutions. We will discuss this in section 4.4.

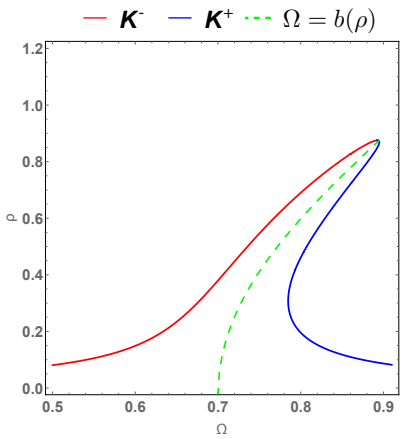

Figure 4.2: Example of the zero-level set of Eq. (4.17) for a damped, non-linear, periodically forced mechanical system with a hardening nonlinearity. The blue and red curves correspond to K^+ and K^-. These two segments come together exactly at the point where the discriminant of the quadratic Eq. (4.47) is equal to zero.

4.4 Analytic criterion for isolas

We will now give an analytic criterion for the emergence of isolas in terms of the function $a(\rho)$ defined in equation (4.10). An essential question is how approximate zeros obtained from finite-order Taylor series expansions persist as $M \to \infty$. Jentzsch [75] proved that in the limit of the order of the Taylor series expansion going to infinity, the non-persistent spurious zeros come arbitrarily close to the boundary of the domain of convergence. Hurwitz [76] showed that in the same limit, the uniform convergence of the Taylor series polynomial leads to a good approximation of the genuine zeros inside the circle of convergence. Christiansen and Madsen[77] numerically verified this behavior on several examples. We will call such a zero ρ_0 of $a(\rho)$, non-spurious if it converges to a genuine zero of $a(\rho)$ in the limit of $M \to \infty$.

Theorem 4.2 *Assume that $\rho_0 \neq 0$ is a non-spurious transverse zero of $a(\rho)$, i.e.,*

$$a(\rho_0) = 0, \quad \partial_\rho a(\rho_0) \neq 0. \tag{4.19}$$

Then, for $\varepsilon > 0$ small enough, system (4.16) has an isola that perturbs from the unforced damped backbone curve $\Omega = b(\rho)$ near the amplitude value ρ_0.

Proof We derive this result in Appendix 4.C.

In order to verify if a non-trivial zero of the Taylor series expansion of $a(\rho)$ is also non-spurious, we compute the (generally complex) zeros of the function $a(\rho)$ for increasing order of approximation M. As we discussed before Theorem 4.2,

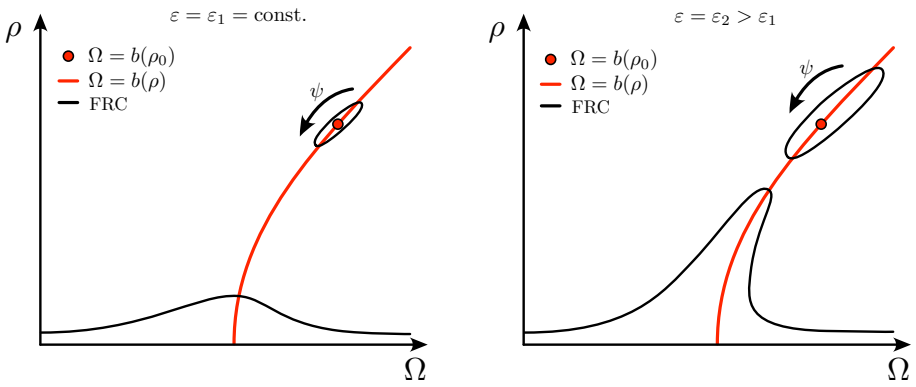

Figure 4.3: An isola of periodic solutions near the damped backbone curve, emerging from a non-trivial transverse zero ρ_0 of $a(\rho)$. The isola curve can be parameterized by the variable ψ.

spurious zeros will converge to the circle defining the radius of convergence of $a(\rho)$, whereas non-spurious zeros stay bounded away from that circle and hence converge to the genuine zeros of $a(\rho)$.

In Fig. 4.3, we sketch qualitatively the statement of Theorem 4.2: a non-spurious, transverse zero ρ_0 of $a(\rho)$ indicates a nearby isola.

4.4.1 Leading-order analytic formula for isolas

For higher-order approximations of $a(\rho)$, we can determine the roots of $a(\rho)$ numerically. Restricting ourselves to a 3^{rd}-order approximation of the SSM, we can, however, extract even an analytic criterion for the existence of an isola. Following the work of Breunung and Haller [8], we truncate the parameterization $\mathbf{W}(\mathbf{s}, \phi)$ and the reduced dynamics $\mathbf{R}(\mathbf{s}, \phi)$ at $\mathcal{O}(\varepsilon|\mathbf{s}|, \varepsilon^2)$, which they justify by introducing the scaling $\mathbf{s} \to \varepsilon^{\frac{1}{4}}\mathbf{s}$, such that the zero problem of the reduced system can be written as

$$\tilde{\mathbf{F}}(\mathbf{u}) = \begin{bmatrix} \underbrace{\text{Re}(\lambda_1)\rho + \text{Re}(\gamma_1)\rho^3}_{a(\rho)} + \varepsilon\left(\text{Re}(c_{1,\mathbf{0}})\cos(\psi) + \text{Im}(c_{1,\mathbf{0}})\sin(\psi)\right) \\ \underbrace{(\text{Im}(\lambda_1) + \text{Im}(\gamma_1)\rho^2}_{b(\rho)} - \Omega)\rho + \varepsilon\left(\text{Im}(c_{1,\mathbf{0}})\cos(\psi) - \text{Re}(c_{1,\mathbf{0}})\sin(\psi)\right) \end{bmatrix} = \mathbf{0}. \tag{4.20}$$

Here we have $f_1 = g_2 = \text{Re}(c_{1,\mathbf{0}})$ and $f_2 = g_1 = \text{Im}(c_{1,\mathbf{0}})$. We now show in Theorem 4.3 that this approximation gives an analytically computable condition for the existence of an isola.

Theorem 4.3 *Assume that for system (4.20),* $\mathrm{Re}(\gamma_1) > 0$ *is satisfied and the cubic-order zero* $\rho_1 = \sqrt{|\mathrm{Re}(\lambda_1)|/\mathrm{Re}(\gamma_1)}$ *of* $a(\rho)$ *is non-spurious. Then the following holds:*

(i) For $\varepsilon > 0$ *small enough, an isola of the type described in Theorem 4.2 exists near the point* $(\Omega, \rho) = (b(\rho_0), \rho_0)$ *of the damped backbone curve.*

(ii) The isola will be disconnected from the main FRC for $\varepsilon > 0$ *values satisfying*

$$\varepsilon < \frac{1}{\|c_{1,\mathbf{0}}\|}\sqrt{\frac{4|\mathrm{Re}(\lambda_1)|^3}{27\mathrm{Re}(\gamma_1)}}. \tag{4.21}$$

(iii) The isola will merge with the main FRC approximately at the ε *value*

$$\varepsilon_{\mathrm{m}} = \frac{1}{\|c_{1,\mathbf{0}}\|}\sqrt{\frac{4|\mathrm{Re}(\lambda_1)|^3}{27\mathrm{Re}(\gamma_1)}}. \tag{4.22}$$

Proof We derive this result in Appendix 4.D.

4.5 Numerical Examples

4.5.1 The modified Shaw–Pierre example

As a typical benchmark, we first consider a modified version of the example of Shaw and Pierre [30], in which an additional cubic nonlinear damper is added, as in the single degree-of-freedom example of Habib et al. [72]. The equations of motion of our two-degree-of-freedom system in first-order form are given by

$$\dot{\mathbf{x}} = \underbrace{\begin{bmatrix} 0 & 0 & 1 & 0 \\ 0 & 0 & 0 & 1 \\ -\dfrac{2k}{m} & \dfrac{k}{m} & -\dfrac{c_1+c_2}{m} & \dfrac{c_2}{m} \\ \dfrac{k}{m} & -\dfrac{2k}{m} & \dfrac{c_2}{m} & -\dfrac{c_1+c_2}{m} \end{bmatrix}}_{\mathbf{A}} \mathbf{x} + \underbrace{\begin{bmatrix} 0 \\ 0 \\ -\dfrac{\kappa}{m}x_1^3 - \dfrac{\alpha}{m}x_3^3 \\ 0 \end{bmatrix}}_{\mathbf{G}_{\mathrm{p}}(\mathbf{x})} + \varepsilon \underbrace{\begin{bmatrix} 0 \\ 0 \\ \dfrac{P}{m}\cos(\Omega t) \\ 0 \end{bmatrix}}_{\mathbf{F}_{\mathrm{p}}(\Omega t)}, \tag{4.23}$$

where $\mathbf{x} = [x_1, x_2, x_3, x_4]^\top = [y_1, y_2, \dot{y}_1, \dot{y}_2]^\top$. The matrix $\mathbf{A}$ has the eigenvalue pairs

$$\lambda_{1,2} = \left(-\zeta_1 \pm \mathrm{i}\sqrt{1-\zeta_1^2}\right)\omega_1, \quad \zeta_1 = \frac{c_1}{2m\omega_1}, \quad \omega_1 = \sqrt{\frac{k}{m}}, \tag{4.24}$$

$$\lambda_{3,4} = \left(-\zeta_2 \pm \mathrm{i}\sqrt{1-\zeta_2^2}\right)\omega_2, \quad \zeta_2 = \frac{c_1+2c_2}{2m\omega_2}, \quad \omega_2 = \sqrt{\frac{3k}{m}}, \tag{4.25}$$

assume that both modes are underdamped, i.e., $0 < \zeta_1 < 1$ and $0 < \zeta_2 < 1$. The matrix $\mathbf{T}$ that transforms our system to complex modal coordinates is composed of the eigenvectors of our system, i.e.,

$$\mathbf{T} = \begin{bmatrix} 1 & 1 & 1 & 1 \\ 1 & 1 & -1 & -1 \\ \lambda_1 & \bar{\lambda}_1 & \lambda_3 & \bar{\lambda}_3 \\ \lambda_1 & \bar{\lambda}_1 & -\lambda_3 & -\bar{\lambda}_3 \end{bmatrix}, \tag{4.26}$$

with the inverse of $\mathbf{T}$ given by

$$\mathbf{T}^{-1} = \begin{bmatrix} -\dfrac{\bar{\lambda}_1}{2(\lambda_1 - \bar{\lambda}_1)} & -\dfrac{\bar{\lambda}_1}{2(\lambda_1 - \bar{\lambda}_1)} & \dfrac{1}{2(\lambda_1 - \bar{\lambda}_1)} & \dfrac{1}{2(\lambda_1 - \bar{\lambda}_1)} \\ \dfrac{\lambda_1}{2(\lambda_1 - \bar{\lambda}_1)} & \dfrac{\lambda_1}{2(\lambda_1 - \bar{\lambda}_1)} & -\dfrac{1}{2(\lambda_1 - \bar{\lambda}_1)} & -\dfrac{1}{2(\lambda_1 - \bar{\lambda}_1)} \\ -\dfrac{\bar{\lambda}_3}{2(\lambda_3 - \bar{\lambda}_3)} & \dfrac{\bar{\lambda}_3}{2(\lambda_3 - \bar{\lambda}_3)} & \dfrac{1}{2(\lambda_3 - \bar{\lambda}_3)} & -\dfrac{1}{2(\lambda_3 - \bar{\lambda}_3)} \\ \dfrac{\lambda_3}{2(\lambda_3 - \bar{\lambda}_3)} & -\dfrac{\lambda_3}{2(\lambda_3 - \bar{\lambda}_3)} & -\dfrac{1}{2(\lambda_3 - \bar{\lambda}_3)} & \dfrac{1}{2(\lambda_3 - \bar{\lambda}_3)} \end{bmatrix}. \tag{4.27}$$

In this example, we can compute the cubic coefficient of $a(\rho)$ explicitly. Specifically, we have

$$\begin{aligned} \mathrm{Re}(\gamma_1) &= \mathrm{Re}\left(-\frac{3\alpha}{m}[\mathbf{T}^{-1}]_{1,3}[\mathbf{T}]_{3,1}^2[\mathbf{T}]_{3,2} - \frac{3\kappa}{m}[\mathbf{T}^{-1}]_{1,3}[\mathbf{T}]_{1,1}^2[\mathbf{T}]_{1,2} \right) && (4.28) \\ &= \mathrm{Re}\left(-\frac{3\left(\alpha\lambda_1^2\bar{\lambda}_1 + \kappa\right)}{2m(\lambda_1 - \bar{\lambda}_1)} \right) && (4.29) \\ &= -\frac{3\alpha k}{4m^2}. && (4.30) \end{aligned}$$

Therefore, for $\alpha < 0$, the reduced dynamics on the third-order autonomous SSM will have a nontrivial zero. If, additionally, this zero is non-spurious, then Theorem 4.3 guarantees the existence of an isola. Using Eq. (4.22), the isola will merge with the main FRC for

$$\varepsilon_{\mathrm{m}} = \frac{8m\sqrt{1-\zeta_1^2}\omega_1}{|P|}\sqrt{\frac{16m^2(\zeta_1\omega_1)^3}{81k|\alpha|}}. \tag{4.31}$$

We verify this analytic prediction numerically in Example 4.4 below.

Example 4.4 We choose the parameter values listed in Table 4.1 and compute the forced response curve for system (4.23). Note that for this choice of damping parameters, the non-resonance conditions (3.9) are satisfied.

Table 4.1: Parameter values for Example 4.4.

Symbol	Value
m	$1\,\mathrm{kg}$
c_1	$0.03\,\mathrm{N}\cdot\mathrm{s/m}$
c_2	$\sqrt{3}\cdot 0.03\,\mathrm{N}\cdot\mathrm{s/m}$
k	$3\,\mathrm{N/m}$
κ	$0.4\,\mathrm{N/m^3}$
α	$-0.6\,\mathrm{N}\cdot(\mathrm{s/m})^3$
P	$3\,\mathrm{N}$

Plugging in the parameter values of Table 4.1 into Eq. (4.30), we observe that the third-order coefficient of the autonomous part of the SSM is

$$\mathrm{Re}(\gamma_1) = -\frac{3\alpha k}{4m^2} = 1.35 > 0. \tag{4.32}$$

We now numerically verify that this transverse zero is non-spurious by computing the (complex) roots of $a(\rho)$ for an increasing order M of expansion in formula (4.10) using SSMtool. In Fig. 4.4, we show these roots, up to 50^{th} order, with lighter colors indicating higher orders of approximation. Eq. (4.32) and Fig. 4.4 allow us to conclude from statement (i) of Theorem 4.3 the existence of an isola near the amplitude value $|\rho_1^{\pm}|$, where $\rho_1^{\pm}$ are the two nontrivial, non-spurious zeros of $a(\rho)$ seen in Fig. 4.4. By Eq. (4.31), the isola will merge with the main branch of the forced response curve approximately at the parameter value

$$\varepsilon_{\mathrm{m}} = 0.0028. \tag{4.33}$$

We now verify this analytic prediction for the isola merger numerically. In Fig. 4.5, we show in red the leading-order forced response curves for $\varepsilon = 0.0027$ and $\varepsilon = 0.0029$. Also shown in black are the forced response curves of the full system obtained via the periodic-orbit toolbox of COCO [31]. We conclude that the FRC obtained from our two-dimensional, SSM-reduced system perfectly predicts the behavior of the full system.

Example 4.5 In this example, we add a quintic nonlinear damper to system (4.23),

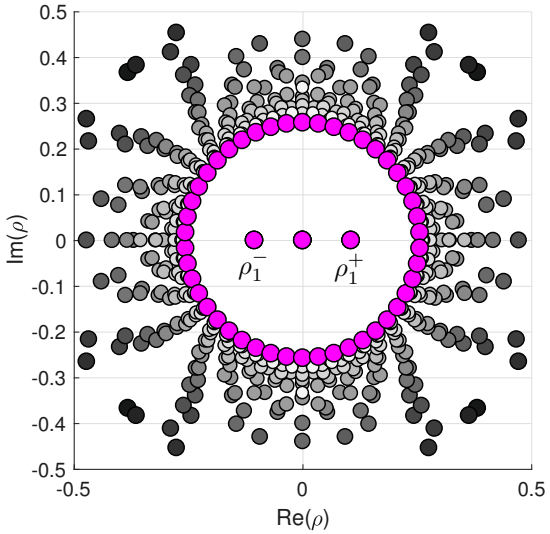

Figure 4.4: Plot of the roots of $a(\rho)$ in the complex plane for Example 4.4, with brighter colors indicating an increasing order M in the expansion of $a(\rho)$, up to 50th order (roots that are negative of each other are to be identified). The zeros from the highest approximation are highlighted in magenta. We observe that a non-trivial transverse zero $\rho_1^{\pm}$ persists for higher-order approximations and is clearly within the domain of convergence of the function $a(\rho)$.

which yields the modified equations of motion in first-order form

$$\dot{\mathbf{x}} = \underbrace{\begin{bmatrix} 0 & 0 & 1 & 0 \\ 0 & 0 & 0 & 1 \\ -\frac{2k}{m} & \frac{k}{m} & -\frac{c_1+c_2}{m} & \frac{c_2}{m} \\ \frac{k}{m} & -\frac{2k}{m} & \frac{c_2}{m} & -\frac{c_1+c_2}{m} \end{bmatrix}}_{\mathbf{A}} \mathbf{x} + \underbrace{\begin{bmatrix} 0 \\ 0 \\ -\frac{\kappa}{m}x_1^3 - \frac{\alpha}{m}x_3^3 - \frac{\beta}{m}x_3^5 \\ 0 \end{bmatrix}}_{\mathbf{G}_{\mathrm{p}}(\mathbf{x})} + \varepsilon \underbrace{\begin{bmatrix} 0 \\ 0 \\ \frac{P}{m}\cos(\Omega t) \\ 0 \end{bmatrix}}_{\mathbf{F}_{\mathrm{p}}(\Omega t)}. \tag{4.34}$$

We again use the parameter values in Table 4.1 and additionally select the quintic damping coefficient $\beta = 1.2\,\mathrm{N}\cdot(\mathrm{s/m})^5$. We use SSMtool to calculate the functions

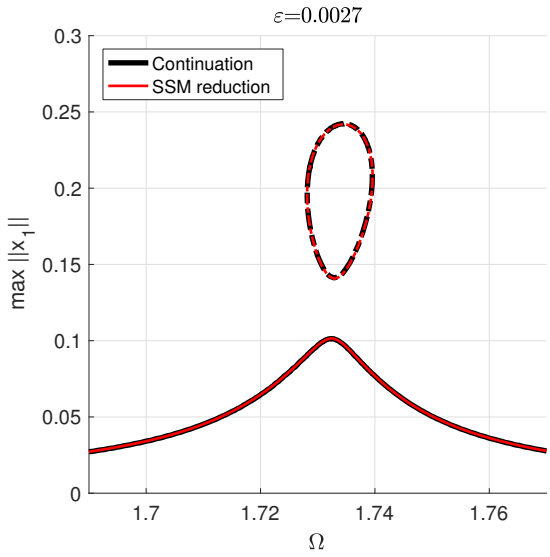

(a)

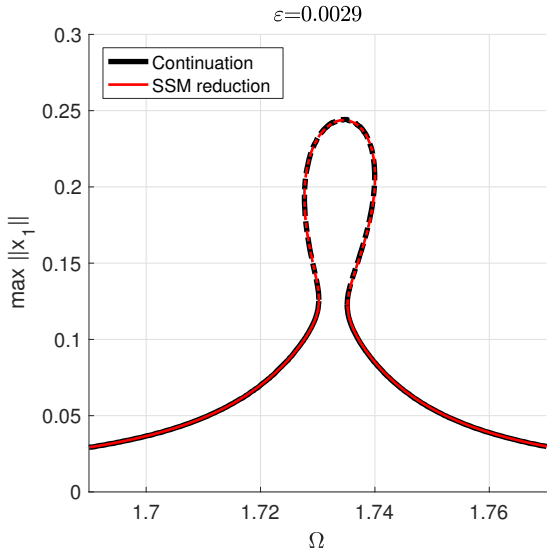

(b)

Figure 4.5: (a) Forced response curve for $\varepsilon = 0.0027$ in Example 4.4, which is slightly below the predicted value ε_{m} for the merger of the isola with the main branch of the FRC. The dashed lines indicate that the isola is unstable. (b) Forced response curve for $\varepsilon = 0.0029$, which is slightly above the predicted merging value ε_m. The unstable isola has indeed merged with the main FRC branch, as predicted analytically.

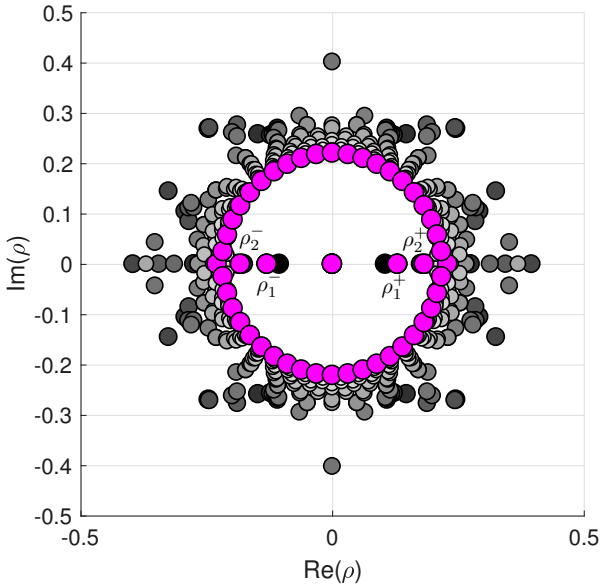

Figure 4.6: Plot of the roots of $a(\rho)$ in the complex plane for Example 4.5, with brighter colors indicating an increasing order M in the expansion of $a(\rho)$, up to 50th order (roots that are negative of each other are to be identified). The zeros from the highest approximation are highlighted in magenta. We observe that the non-trivial transverse zeros $\rho_1^{\pm}$ and $\rho_2^{\pm}$ persist for higher-order approximations and is clearly within the domain of convergence of the function $a(\rho)$.

included in the reduced dynamics (4.8)-(4.9) up to 5^{th} order in ρ. The function $a(\rho)$ now has two positive, non-spurious zeros located at $\rho_1^+ = 0.13$ and $\rho_2^+ = 0.17$. Therefore, Theorem 4.2 implies the existence of two separate isolas bifurcating from the damped backbone curve under periodic forcing.

We show the extracted forced response curves for three different values of ε in Fig. 4.7. As we have predicted above, two isolas are born out of the non-trivial transverse zeros of $a(\rho)$ along the autonomous backbone curve. The isola with lower amplitudes is unstable, whereas the isola with higher amplitudes is partially stable. If we increase the forcing amplitude ε, the two isolas merge. Increasing ε further will make the merged isolas merge with the lower FRC branch. The branches of the forced response curve, extracted using SSM theory, are again verified using the periodic-orbit toolbox of COCO [31]. In order to initialize the continuation algorithm, we integrate the full system to provide an initial solution guess that is used to start the continuation process. For higher amplitude values, our 5^{th}-order approximation slightly deviates from the numerical continuation results, as expected. For lower amplitudes, however, our SSM-based prediction perfectly matches the numerical result.

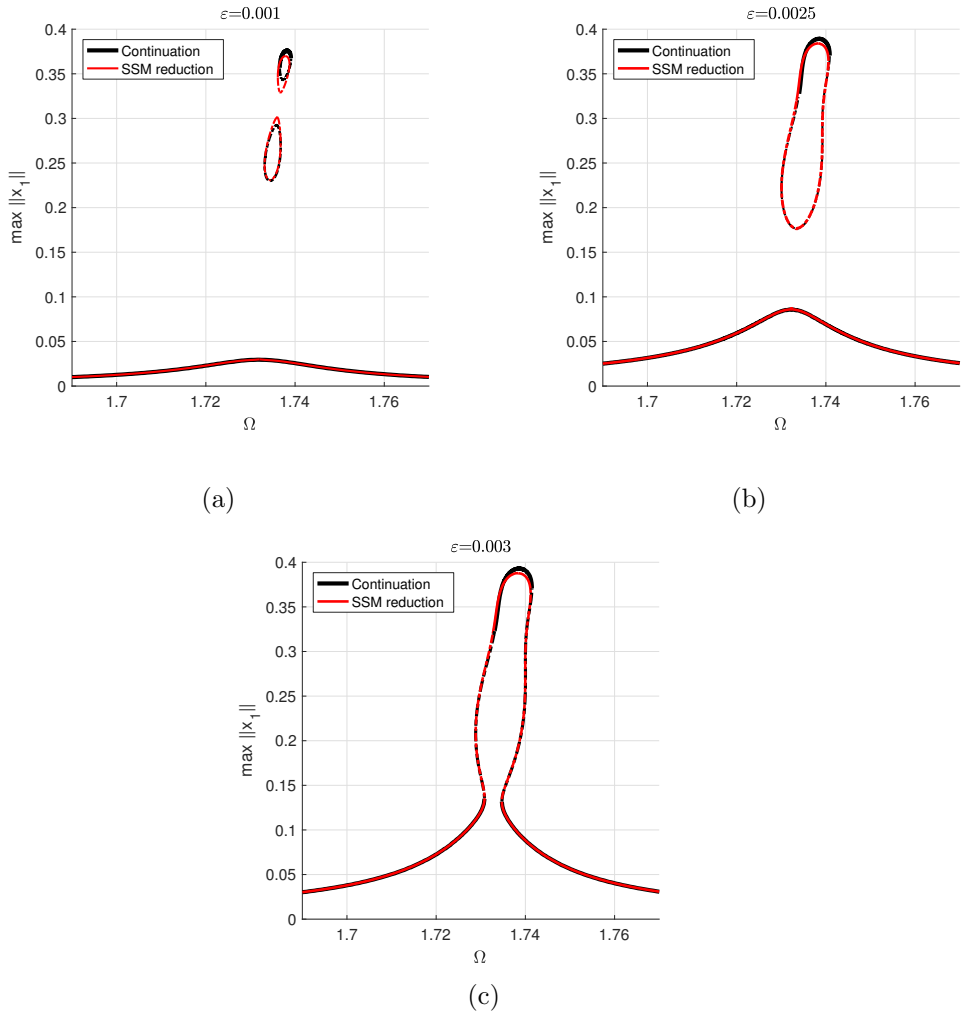

Figure 4.7: (a) Resulting forced response curve for $\varepsilon = 0.001$ in Example 4.5. Two isolas are born out of the non-trivial transverse zeros of $a(\rho)$, located at $(b(\Omega), \rho)$ on the autonomous backbone curve. The dashed lines indicate that the lower-amplitude isola is unstable in nature, whereas the higher-amplitude isola is partially stable. (b) Forced response curve for $\varepsilon = 0.0025$. Both isolas have merged into one bigger isolated region. The lower half of the merged isolas is unstable in nature, whereas the upper half is stable. (c) Forced response curve for $\varepsilon = 0.003$. The two merged isolas now have merged with the lower branch of the FRC.

4.5.2 A discretized, forced Bernoulli beam with a cubic spring and damper

Similarly to the example in section 3.6, we now construct a reduced-order model for a discretized, cantilevered Bernoulli beam with a cubic spring and, additionally, a cubic damper attached to the free end of the beam. We obtain the reduced model by computing the dynamics on the slowest, two-dimensional, time-periodic SSM of the system.

The beam is of length L, with the square cross-section A, situated in a Cartesian coordinate system of (x, y, z) and basis $(\mathbf{e}_x, \mathbf{e}_y, \mathbf{e}_z)$. The relevant beam parameters are listed in Table 4.2. The beam's neutral axis is the line of points coinciding with

Table 4.2: Notation used in the discretized beam example.

Symbol	Meaning (unit)
L	Length of beam (mm)
h	Height of beam (mm)
b	Width of beam (mm)
ρ	Density (kg/mm^3)
E	Young's Modulus (kPa)
I	Area moment of inertia (mm^4)
κ	Coefficient cubic spring (mN/mm^3)
γ	Coefficient cubic damper (mN $\cdot$ s/mm^3)
A	Cross-section of beam (mm^2)
P	External forcing amplitude (mN)

the x-axis. The Bernoulli hypothesis states that initially straight material lines, normal to the neutral axis, remain (a) straight and (b) inextensible, and (c) rotate as rigid lines to remain perpendicular to the beam's neutral axis after deformation. The transverse displacement of a material point with initial coordinates on the beam's neutral axis at $z = 0$ is denoted by $w(x)$. The rotation angle of a transverse normal line about the y-axis is given by $-\partial_x w(x)$. We assume an isotropic, linearly elastic constitutive relation between the stresses and strains. This yields the following equations of motion

$$\rho A \frac{\partial^2 w(x,t)}{\partial t^2} - \rho I \frac{\partial^4 w(x,t)}{\partial x^2 \partial t^2} + EI \frac{\partial^4 w(x,t)}{\partial x^4} = 0. \tag{4.35}$$

We can neglect the mixed partial derivative term in Eq. (3.54) by assuming that the thickness of the beam is small compared to its length, i.e., $h \ll L$ (see Reddy

and Mahaffey [33]), we therefore can write Eq. (4.35) as

$$\rho A \frac{\partial^2 w(x,t)}{\partial t^2} + EI \frac{\partial^4 w(x,t)}{\partial x^4} = 0. \tag{4.36}$$

We discretize Eq. (4.36) and obtain a set of ordinary differential equations

$$\mathbf{M}\ddot{\mathbf{y}} + \mathbf{K}\mathbf{y} = \mathbf{0}, \tag{4.37}$$

where $\mathbf{y} \in \mathbb{R}^{2m} = \mathbb{R}^n$, and m is the number of elements used in the discretization. Each node of the beam has two coordinates related to the transverse displacement $w(x)$ and the rotation angle $-\partial_x w(x)$ of the cross section. Structural damping is assumed by considering the damping matrix

$$\mathbf{C} = \alpha\mathbf{M} + \beta\mathbf{K}, \tag{4.38}$$

with parameters α and β. We apply cosinusoidal external forcing on the transverse displacement coordinate at the free end of the beam with forcing frequency Ω and forcing amplitude εP. Additionally, we add a cubic spring and damper along this coordinate, with coefficients κ and γ, respectively. As a result, the second-order equations of motion can be written as

$$\mathbf{M}\ddot{\mathbf{y}} + \mathbf{C}\dot{\mathbf{y}} + \mathbf{K}\mathbf{y} + \mathbf{g}(\mathbf{y}, \dot{\mathbf{y}}) = \varepsilon \mathbf{f}(\Omega t). \tag{4.39}$$

We give an illustration of the beam in Fig. 4.8.

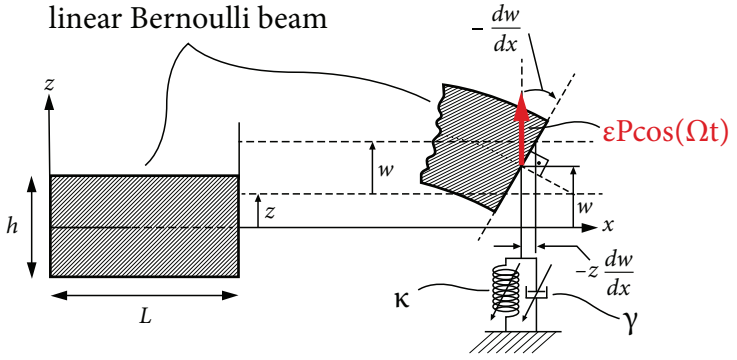

Figure 4.8: Forced Bernoulli beam with a cubic spring and damper.

We select $m = 25$ for the number of discretized elements, which gives $\mathbf{x} \in \mathbb{R}^{50}$, resulting in a 100-dimensional phase space. We list the geometric and material parameter values in Table 4.3.

Table 4.3: Geometric and material parameters for the Bernoulli beam.

Symbol	Value
L	$2700\,\mathrm{mm}$
h	$10\,\mathrm{mm}$
b	$10\,\mathrm{mm}$
ρ	$1780 \cdot 10^{-9}\,\mathrm{kg/mm^3}$
E	$45 \cdot 10^{6}\,\mathrm{kPa}$
κ	$6\,\mathrm{mN/mm^3}$
γ	$-0.02\,\mathrm{mN \cdot s/mm^3}$
α	$1.25 \cdot 10^{-4}\,\mathrm{s^{-1}}$
β	$2.5 \cdot 10^{-4}\,\mathrm{s}$
P	$0.1\,\mathrm{mN}$

For these parameter values, the eigenvalues corresponding to the slowest eigenspace are

$$\lambda_{1,2} = -0.0061884 \pm 7.0005\mathrm{i}. \tag{4.40}$$

As earlier, introducing the scaling $\mathbf{s} \to \varepsilon^{\frac{1}{4}}\mathbf{s}$, we obtain the approximations

$$a(\rho) = -0.0061884\rho + 0.036202\rho^3, \tag{4.41}$$

$$b(\rho) = 7.0005 + 0.031689\rho^2, \tag{4.42}$$

$$c_{1,\mathbf{0}} = 0.54645 + 0.00048\mathrm{i}. \tag{4.43}$$

The function $a(\rho)$ in Eq. (4.41) has a non-trivial, transverse, positive zero at $\rho_1^+ = 0.413$. Fig. 4.9 shows this zero to be non-spurious. Therefore, by Theorem 4.3, an isola will perturb from the point $(\Omega = b(\rho_1^+), \rho_1^+)$ of the autonomous backbone curve. Also by Theorem 4.3, the isola will merge with the main branch of the FRC approximately for

$$\varepsilon_{\mathrm{m}} = \frac{1}{\|c_{1,\mathbf{0}}\|}\sqrt{\frac{4|\mathrm{Re}(\lambda_1)|^3}{27\mathrm{Re}(\gamma_1)}} = 0.0018. \tag{4.44}$$

To verify our predicted merger amplitude in (4.44), we perform a discrete numerical sweep of the full system, in which we force the system at different forcing frequencies and plot the resulting maximum absolute value of the transverse displacement of the tip of the beam, while keeping the forcing amplitude fixed (see Fig. 4.10).

While numerical continuation using the `po` toolbox of COCO remains a powerful tool in verifying our analytic predictions in lower dimensions, its use becomes computationally expensive in higher dimensions. For this reason, Fig. 4.10 only shows a discrete set of periodic responses computed from a point-wise, long-term numerical integration leading to a steady state, as opposed to a continuous FRC obtained from numerical continuation.

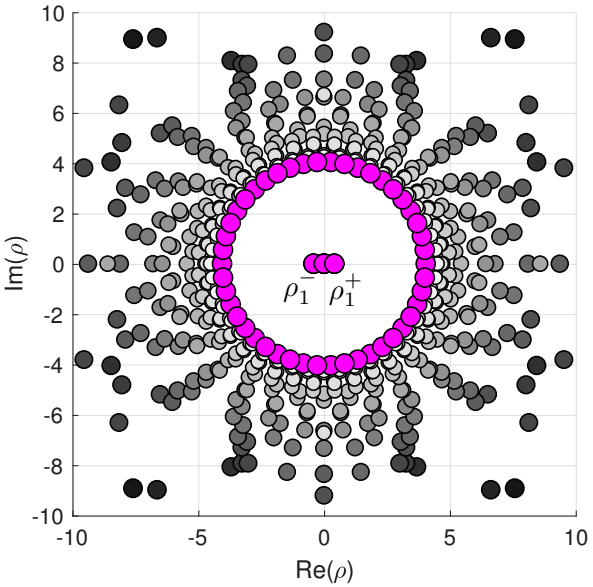

Figure 4.9: Plot of the roots of $a(\rho)$ in the complex plane for Example 4.5.2, with brighter colors indicating an increasing order M in the expansion of $a(\rho)$, up to 50th order (roots that are negative of each other are to be identified). The zeros from the highest approximation are highlighted in magenta. We observe that a non-trivial transverse zero $\rho_1^{\pm}$ persists for higher-order approximations and is clearly within the domain of convergence of the function $a(\rho)$.

4.6 Conclusions

We have used the exact reduced dynamics on two-dimensional time-periodic spectral submanifolds (SSMs) to extract forced-response curves (FRCs) and predict isolas in arbitrary multi-degree-of-freedom mechanical systems without performing costly numerical simulations. We showed that for a cubic-order approximation, the reduced dynamics on the SSM gives an analytic prediction for the isolas, valid for any mode of a multi-degree-of-freedom oscillatory system. For simple examples, these predictions can explicitly be expressed as functions of the system parameters. Our lower-order predictions can be refined to higher-orders using the publicly available MATLAB script SSMtool[2].

For mechanical systems of high degrees of freedom, numerical continuation techniques for forced response curves become computationally expensive. Instead, using the non-autonomous SSM and the corresponding reduced dynamics on the SSM, we are able to approximate all possible FRCs for different forcing amplitudes, as our

[2]SSMtool is available at: www.georgehaller.com

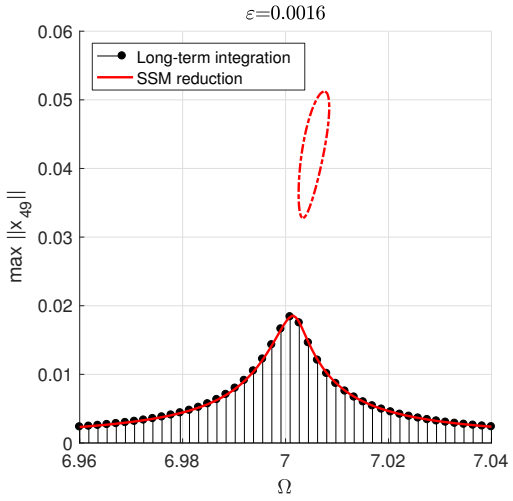

(a)

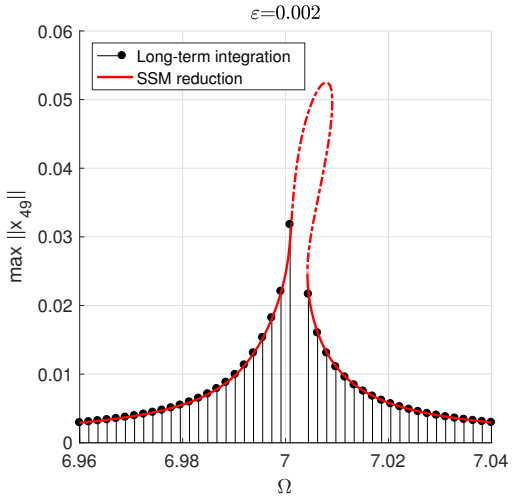

(b)

Figure 4.10: (a) Extracted forced response curve for $\varepsilon = 0.0016$ in Example 4.5.2. An unstable isola is born out of the non-trivial transverse zero of $a(\rho)$, located at $(\Omega = b(\rho_1^+), \rho_1^+)$ on the autonomous backbone curve. (b) Extracted forced response curve from the reduced dynamics for $\varepsilon = 0.002 > \varepsilon_{\mathrm{m}}$. The main FRC branch has merged with the unstable isola. A discrete frequency sweep has been performed on the full 100-dimensional system to verify the accuracy of our two-dimensional reduced model. The frequency region in which the FRC becomes unstable, as predicted by the SSM-based reduced dynamics, is confirmed by the full numerical frequency sweep.

expressions depend symbolically on the forcing amplitude ε. An additional advantage of the results derived here is that the isolas are uncovered by the transverse intersection of the zero-level sets of our two reduced equations. The isolas will generally be missed by numerical continuation techniques, which require starting on an isolated solution branch. As we have shown, our predictions for the main FRC branches, as well as for isolas, remain valid and computable in high dimensional problems in which numerical continuation is no longer a viable alternative for constructing these curves. Using the general results of Haller and Ponsioen [4], one can extend the periodic approach to detect quasi-periodic responses and isolas under quasi-periodic forcing.

Appendix

4.A Extracting the forced response curve

For convenience, we restate our zero problem (4.16),

$$\mathbf{F}(\mathbf{u}) = \begin{bmatrix} F_1(\mathbf{u}) \\ F_2(\mathbf{u}) \end{bmatrix} = \begin{bmatrix} a(\rho) + \varepsilon \left(f_1(\rho, \Omega)\cos(\psi) + f_2(\rho, \Omega)\sin(\psi) \right) \\ (b(\rho) - \Omega)\rho + \varepsilon \left(g_1(\rho, \Omega)\cos(\psi) - g_2(\rho, \Omega)\sin(\psi) \right) \end{bmatrix} = \mathbf{0}, \tag{4.45}$$

where

$$\mathbf{F}(\mathbf{u}) : \mathbb{R}^3 \to \mathbb{R}^2, \quad \mathbf{u} = \begin{bmatrix} \rho \\ \Omega \\ \psi \end{bmatrix}.$$

If there exists a regular point $\mathbf{p} = (\rho, \Omega, \psi)$, such that $\mathbf{F}(\mathbf{p}) = \mathbf{0}$ in (4.45) and the Jacobian of $\mathbf{F}$ evaluated at $\mathbf{p}$ is surjective, then by the implicit function theorem, locally there exists a one-dimensional submanifold of $\mathbb{R}^3$ which will represent the forced response curve when projected onto the (Ω, ρ)-space. Equivalently, the zero-level sets of $F_1(\mathbf{u})$ and $F_2(\mathbf{u})$ in (4.45), which we will denote by $\mathcal{M}_1^{\mathbf{p}}$ and $\mathcal{M}_2^{\mathbf{p}}$, will be two two-dimensional submanifolds in the (ρ, ψ, Ω)-space that, locally around $\mathbf{p}$, intersect each other transversely, yielding the forced response curve. We illustrate this concept in Fig. 4.A.1, which is a typical picture for a damped non-linear periodically forced mechanical system with a hardening nonlinearity.

4.B Proof of Theorem 4.1

Let $\mathbf{u}_0$ be a regular point of the map $\mathbf{F}(\mathbf{u})$ (4.16) such that $\mathbf{F}(\mathbf{u}_0) = \mathbf{0}$, and $D_{\mathbf{u}}\mathbf{F}(\mathbf{u}_0)$ is surjective. Then, by the implicit function theorem, locally there exists a one-dimensional submanifold of $\mathbb{R}^3$ around $\mathbf{u}_0$. We express ψ as a function of ρ and Ω, using the tangent half-angle substitution and the trigonometric identities,

$$\frac{\psi}{2} = \tan^{-1}(K), \quad \cos(\psi) = \frac{1 - K^2}{1 + K^2}, \quad \sin(\psi) = \frac{2K}{1 + K^2}. \tag{4.46}$$

Setting Eq. (4.8) equal to zero and substituting the identities into Eq. (4.8), we obtain a quadratic equation in K,

$$(a(\rho) - \varepsilon f_1(\rho, \Omega))\, K^2 + 2\varepsilon f_2(\rho, \Omega) K + (a(\rho) + \varepsilon f_1(\rho, \Omega)) = 0, \tag{4.47}$$

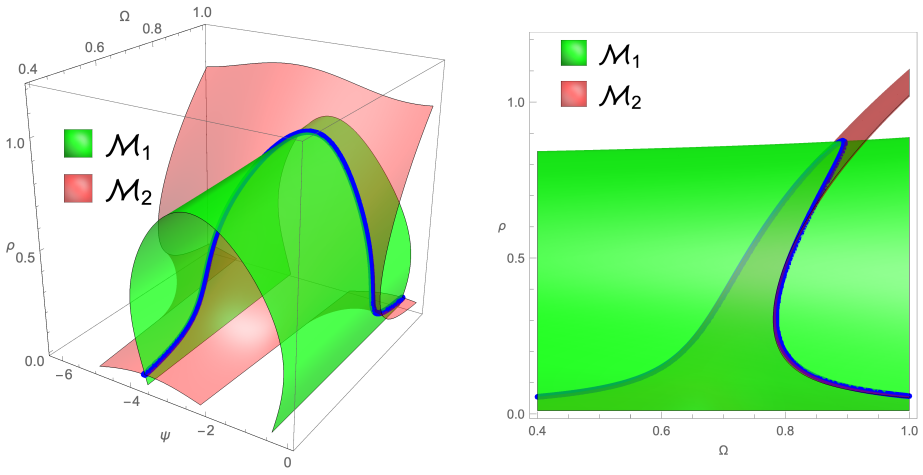

Figure 4.A.1: (a)-(b): Intersection of $\mathcal{M}_1$ (green) and $\mathcal{M}_2$ (red), yielding the frequency-response curve in blue.

which has the solution,

$$K(\rho;\Omega)^{\pm} = \frac{-\varepsilon f_2(\rho,\Omega) \pm \sqrt{\varepsilon^2\left(f_1(\rho,\Omega)^2 + f_2(\rho,\Omega)^2\right) - a(\rho)^2}}{a(\rho) - \varepsilon f_1(\rho,\Omega)}. \tag{4.48}$$

Substituting Eq. (4.48), together with the trigonometric identities in (4.46), into Eq. (4.9), we obtain the result stated in Theorem 4.1.

4.C Proof of Theorem 4.2

We now consider ε to be a variable in our zero problem (4.16), i.e.

$$\mathbf{F}(\mathbf{u},\varepsilon) : \mathbb{R}^4 \to \mathbb{R}^2, \quad \mathbf{u} = \begin{bmatrix} \rho \\ \Omega \\ \psi \end{bmatrix}.$$

If there exists a non-spurious non-trivial transverse zero $\rho_0 : a(\rho_0) = 0$ and $\partial_\rho a(\rho_0) \neq 0$, then by restricting ourselves to the autonomous backbone curve (see Ponsioen et al. [6]), i.e.

$$\mathbf{u}_0 = [\rho_0, \Omega_0, \psi_0,]^\top, \quad \Omega_0 = b(\rho_0), \quad \psi_0 = \text{const.}, \quad \varepsilon = 0,$$

we have found a solution

$$\mathbf{F}(\mathbf{u}_0, 0) = \mathbf{0}. \tag{4.49}$$

The Jacobian of $\mathbf{F}$ with respect to ρ and Ω, evaluated at the solution $(\mathbf{u}_0, 0)$, is given by the square matrix

$$D_{(\rho,\Omega)}\mathbf{F}(\mathbf{u}_0, 0) = \begin{bmatrix} \partial_\rho a(\rho_0) & 0 \\ \partial_\rho b(\rho_0)\rho_0 & -\rho_0 \end{bmatrix}, \tag{4.50}$$

which is invertible. Therefore, by the implicit function theorem, we can continue our solution as a two-dimensional submanifold of $\mathbb{R}^4$. Locally, we can express ρ and Ω as a function of ψ and ε. For $\varepsilon > 0$, an isola is born out of the non-trivial transverse zero on the autonomous backbone curve located at $(\Omega, \rho) = (b(\rho_0), \rho_0)$. For a fixed forcing ampltide ε, the isola is parameterized by ψ (as illustrated in Fig. 4.3).

4.D Proof of Theorem 4.3

In the setting of (4.20), our implicit function (4.17) will reduce to

$$G(\rho, \Omega) = (b(\rho) - \Omega)\rho \pm \sqrt{\varepsilon^2 \|c_{1,\mathbf{0}}\|^2 - a(\rho)^2} = 0. \tag{4.51}$$

Any zero ρ_0 that makes the square root term in Eq. (4.51) vanish, will also be a zero of (4.51) itself by setting $\Omega = b(\rho_0)$, and therefore will be on the forced response curve and on the autonomous backbone curve. Additionally, at this point, two segments of the FRC will meet and create a fold over the Ω direction. We set the argument inside the square root in Eq. (4.51) equal to zero and rewrite it as

$$\Delta(\rho) = a(\rho) \pm \varepsilon \|c_{1,\mathbf{0}}\| = 0. \tag{4.52}$$

Restricting $\rho \in \mathbb{R}_0^+$, then for $\mathrm{Re}(\gamma_1) > 0$, the third-order autonomous function $a(\rho)$ will have a trivial transverse zero and a non-trivial transverse zero located at

$$\rho_0 = 0, \quad \rho_1 = \sqrt{\frac{|\mathrm{Re}(\lambda_1)|}{\mathrm{Re}(\gamma_1)}}, \tag{4.53}$$

such that $a(\rho_0) = 0$, $a(\rho_1) = 0$, $\partial_\rho a(\rho_0) \neq 0$ and $\partial_\rho a(\rho_1) \neq 0$. Under the assumption that the cubic order zero ρ_1 is a non-spurious zero for the function $a(\rho)$, then, using the same type of argument as in the proof of Theorem 4.2, an isola will be born out of this non-trivial transverse zero for system (4.20).

We note that between ρ_0 and ρ_1, $a(\rho)$ will have a local minimum at,

$$\partial_\rho a(\rho) = -|\mathrm{Re}(\lambda_1)| + 3\mathrm{Re}(\gamma_1)\rho^2 = 0 \quad \Rightarrow \quad \tilde{\rho} = \sqrt{\frac{|\mathrm{Re}(\lambda_1)|}{3\mathrm{Re}(\gamma_1)}}. \tag{4.54}$$

Therefore, for $\varepsilon > 0$ small enough, the function $a(\rho)$ will have three intersections with the constant curves $\pm\varepsilon\|c_{1,\mathbf{0}}\|$, meaning that we have found three zeros, $0 <$

$\rho_0^{\mathrm{a}} < \rho_1^{\mathrm{a}} < \rho_1^{\mathrm{b}}$ of Eq. (4.52), that correspond to three folding points of the FRC over the Ω direction. In this setting, ρ_0^{a} corresponds to the maximum amplitude of the main FRC branch, ρ_1^{a} corresponds to the minimum amplitude of the isola, whereas ρ_1^{b} will be the maximum amplitude of the isola.

We can increase ε such that $\rho_0^{\mathrm{a}} = \rho_1^{\mathrm{a}}$, which merges the maximum amplitude of the main FRC branch with the minimum amplitude of the isola, which is exactly at

$$\varepsilon_{\mathrm{m}} = \frac{1}{\|c_{1,\mathbf{0}}\|}\sqrt{\frac{4|\mathrm{Re}(\lambda_1)|^3}{27\mathrm{Re}(\gamma_1)}}, \tag{4.55}$$

whereas for

$$0 < \varepsilon < \frac{1}{\|c_{1,\mathbf{0}}\|}\sqrt{\frac{4|\mathrm{Re}(\lambda_1)|^3}{27\mathrm{Re}(\gamma_1)}}. \tag{4.56}$$

the isola will be disconnected from the main FRC, proving Theorem 4.3.

Chapter 5

General Conclusions

In this thesis we developed the computational tools to construct exact reduced-order models for nonlinear (non-)autonomous mechanical systems using spectral submanifold (SSM) theory, developed by Haller and Ponsioen [4]. In order to construct the SSMs, we used a systematic approach also known as the parameterization method from Cabré et al. [22, 23, 24]. In the autonomous setting, the reduced dynamics on the SSM can be used to extract damped backbone curves, uncovering insightful information about the nonlinear response of the full system without using any numerical integration on the full system.

We then extended the work to the non-autonomous setting, where we used the reduced dynamics on two-dimensional time-periodic SSMs to extract forced-response curves (FRCs) around vibration modes of interest. We showed that the use of multivariate recurrence relations to construct the SSMs, provides a major speed up relative to the autonomous SSM algorithm, allowing us to analyze high-degree-of-freedom mechanical systems, obtained using finite element methods, in a fraction of the time compared to other state-of-the-art numerical methods such as the harmonic balance (HB) method or a collocation method.

Using SSM theory in combination with the developed computational engine we were able to predict isolated branches of periodic responses, also known as isolas, in arbitrary multi-degree-of-freedom mechanical systems without performing costly numerical simulations. We showed that for a cubic-order approximation, the reduced dynamics on the SSM gives an analytic prediction for the isolas, valid for any mode of a multi-degree-of-freedom oscillatory system. For simple examples, these predictions can explicitly be expressed as functions of the system parameters.

Finally, we created a MATLAB based computational tool called SSMtool for computing two-dimensional SSMs in nonlinear mechanical systems with arbitrary degrees of freedom. SSMtool is created for researchers and students who are interested in applying SSM theory to nonlinear, non-conservative mechanical systems with a potentially large number of degrees of freedom in order to extract reduced-order models, backbone curves or forced-response curves

As future work, using the general results of Haller and Ponsioen [4], we can ex-

tend the time-periodic results to a quasi-periodic setting to extract quasi-periodic responses and isolas under quasi-periodic forcing. Additionally, the dimension of the SSMs can be increased in order to deal with internal resonances, which has not been done so far.

Bibliography

[1] R. Rosenberg, The normal modes of nonlinear n-degree-of-freedom systems, J. Appl. Mech. 29 (1) (1962) 7–14. doi:10.1115/1.3636501.

[2] S. Shaw, C. Pierre, Normal modes for non-linear vibratory systems, J. Sound Vib. 164 (1) (1993) 85–124. doi:10.1006/jsvi.1993.1198.

[3] A. Lyapunov, The general problem of the stability of motion, Int. J. Control 55 (3) (1992) 531–534. doi:10.1080/00207179208934253.

[4] G. Haller, S. Ponsioen, Nonlinear normal modes and spectral submanifolds: existence, uniqueness and use in model reduction, Nonlinear Dyn. 86 (3) (2016) 1493–1534. doi:10.1007/s11071-016-2974-z.

[5] N. Fenichel, J. Moser, Persistence and smoothness of invariant manifolds for flows, Indiana University Mathematics Journal 21 (3) (1971) 193–226. doi:10.1512/iumj.1972.21.21017.

[6] S. Ponsioen, T. Pedergnana, G. Haller, Automated computation of autonomous spectral submanifolds for nonlinear modal analysis, Journal of Sound and Vibration 420 (2018) 269–295. doi:10.1016/j.jsv.2018.01.048.

[7] S. Ponsioen, G. Haller, Exact Model Reduction and Fast Forced Response Calculation in High-Dimensional Nonlinear Mechanical Systems, arXiv preprint arXiv:1912.11399.

[8] T. Breunung, G. Haller, Explicit backbone curves from spectral submanifolds of forced-damped nonlinear mechanical systems, Proc. R. Soc. A 474 (2213) (2018) 20180083. doi:10.1098/rspa.2018.0083.

[9] S. Ponsioen, T. Pedergnana, G. Haller, Analytic Prediction of Isolated Forced Response Curves from Spectral Submanifolds, Nonlinear Dynamics 98 (4) (2019) 2755–2773. doi:https://doi.org/10.1007/s11071-019-05023-4.

[10] Z. Veraszto, S. Ponsioen, G. Haller, Explicit third-order model reduction formulas for general nonlinear mechanical systems, Journal of Sound and Vibration 468 (2020) 115039. doi:https://doi.org/10.1016/j.jsv.2019.115039.

[11] G. Kerschen, M. Peeters, J.-C. Golinval, A. Vakakis, Nonlinear normal modes, Part I: A useful framework for the structural dynamicist, Mech. Syst. Sig. Process. 23 (1) (2009) 170–194. doi:10.1016/j.ymssp.2008.04.002.

[12] M. Peeters, R. Viguié, G. Sérandour, G. Kerschen, J.-C. Golinval, Nonlinear normal modes, Part II: Toward a practical computation using numerical continuation techniques, Mech. Syst. Sig. Process. 23 (1) (2009) 195–216. doi:10.1016/j.ymssp.2008.04.003.

[13] Y. Mikhlin, K. Avramov, Nonlinears normal modes for vibrating mechanical systems. Review of theoretical developments, Appl. Mech. Rev. 63 (6) (2010) 060802. doi:10.1115/1.4003825.

[14] A. Vakakis, L. Manevitch, Y. Mikhlin, V. Pilipchuk, A. Zevin, Normal modes and localization in nonlinear systems, Springer, 2001. doi:10.1002/9783527617869.

[15] A. Kelley, Analytic two-dimensional subcenter manifolds for systems with an integral, Pac. J. Math. 29 (1969) 335–350. doi:10.2140/pjm.1969.29.335.

[16] R. Szalai, D. Ehrhardt, G. Haller, Nonlinear model identification and spectral submanifolds for multi-degree-of-freedom mechanical vibrations, in: Proc. R. Soc. A, Vol. 473, The Royal Society, 2017, p. 20160759. doi:10.1098/rspa.2016.0759.

[17] G. Kerschen, K. Worden, A. Vakakis, J.-C. Golinval, Past, present and future of nonlinear system identification in structural dynamics, Mech. Syst. Sig. Process. 20 (3) (2006) 505–592. doi:10.1016/j.ymssp.2005.04.008.

[18] M. Peeters, G. Kerschen, J.-C. Golinval, Dynamic testing of nonlinear vibrating structures using nonlinear normal modes, J. Sound Vib. 330 (3) (2011) 486–509. doi:10.1016/j.jsv.2010.08.028.

[19] F. Blanc, C. Touzé, J. Mercier, K. Ege, A. Ben-Dhia, On the numerical computation of nonlinear normal modes for reduced-order modelling of conservative vibratory systems, Mech. Syst. Sig. Process. 36 (2) (2013) 520–539. doi:10.1016/j.ymssp.2012.10.016.

[20] E. Pesheck, C. Pierre, S. Shaw, A new Galerkin-based approach for accurate non-linear normal modes through invariant manifolds, J. Sound Vib. 249 (5) (2002) 971–993. doi:10.1006/jsvi.2001.3914.

[21] L. Renson, G. Deliége, G. Kerschen, An effective finite-element-based method for the computation of nonlinear normal modes of nonconservative systems, Meccanica 49 (8) (2014) 1901–1916. doi:10.1007/s11012-014-9875-3.

[22] X. Cabré, E. Fontich, R. De La Llave, The parameterization method for invariant manifolds I: manifolds associated to non-resonant subspaces, Indiana Univ. Math. J. 52 (2) (2003) 283–328. doi:10.1512/iumj.2003.52.2245.

[23] X. Cabré, E. Fontich, R. De La Llave, The parameterization method for invariant manifolds II: regularity with respect to parameters, Indiana Uni. math. j. 52 (2) (2003) 329–360. doi:10.1512/iumj.2003.52.2407.

[24] X. Cabré, E. Fontich, R. De La Llave, The parameterization method for invariant manifolds III: overview and applications, J. of Diff. Eq. 218 (2) (2005) 444–515. doi:10.1016/j.jde.2004.12.003.

[25] À. Haro, M. Canadell, J.-L. Figueras, A. Luque, J.-M. Mondelo, The Parameterization Method for Invariant Manifolds, Springer, 2016. doi:10.1007/978-3-319-29662-3.

[26] J. van den Berg, J. Mireles James, Parameterization of Slow-Stable Manifolds and their Invariant Vector Bundles: Theory and Numerical Implementation, Discrete Contin. Dyn. Syst 36 (9). doi:10.3934/dcds.2016002.

[27] J. Mireles James, Polynomial approximation of one parameter families of (un) stable manifolds with rigorous computer assisted error bounds, Indagationes Mathematicae 26 (1) (2015) 225–265. doi:10.1016/j.indag.2014.10.002.

[28] A. Laub, Matrix analysis for scientists and engineers, SIAM, Philadelphia, 2005. doi:10.1137/1.9780898717907.

[29] M. Géradin, D. Rixen, Mechanical vibrations: theory and application to structural dynamics, John Wiley & Sons, 2014. doi:10.1017/aer.2018.27.

[30] S. Shaw, C. Pierre, Normal modes of vibration for non-linear continuous systems, J. Sound Vib.doi:10.1006/jsvi.1994.1021.

[31] H. Dankowicz, F. Schilder, Recipes for Continuation, Computational Science and Engineering, Society for Industrial and Applied Mathematics, Philadelphia, PA.doi:10.1137/1.9781611972573.

[32] G. Cirillo, A. Mauroy, L. Renson, G. Kerschen, R. Sepulchre, A spectral characterization of nonlinear normal modes, J. Sound Vib. 377 (2016) 284–301. doi:10.1016/j.jsv.2016.05.016.

[33] J. Reddy, P. Mahaffey, Generalized beam theories accounting for von Kármán nonlinear strains with application to buckling, J. of Coup. Sys. and Mult. Dyn. 1 (1) (2013) 120–134. doi:10.1166/jcsmd.2013.1006.

[34] W. Lai, D. Rubin, E. Krempl, Introduction to continuum mechanics, Butterworth-Heinemann, 2009. doi:10.1016/B978-0-7506-8560-3.X0001-1.

[35] J. Skrzypek, A. Ganczarski, Constitutive equations for isotropic and anisotropic linear viscoelastic materials, in: Mechanics of Anisotropic Materials, Springer, 2015, pp. 57–85. doi:10.1007/978-3-319-17160-9_2.

[36] G. Lesieutre, J. Kauffman, 'Geometric' Viscous Damping Model for Nearly Constant Beam Modal Damping, AIAA J. 51 (7) (2013) 1688–1694. doi:10.2514/1.j052174.

[37] G. Lesieutre, Frequency-independent modal damping for flexural structures via a viscous "Geometric" damping model, J. of guid., cont., and dyn. 33 (6) (2010) 1931–1935. doi:10.2514/1.49864.

[38] G. Takács, Basics of Vibration Dynamics, in: Model Predictive Vibration Control, Springer, 2012, pp. 25–64. doi:10.1007/978-1-4471-2333-0_2.

[39] J. Reddy, An introduction to nonlinear finite element analysis : with applications to heat transfer, fluid mechanics, and solid mechanics, 2nd Edition, Oxford University Press, Oxford, 2015.

[40] R. Stanley, Enumerative Combinatorics. Vol. 1, vol. 49 of Cambridge Studies in Advanced Mathematics, Cambridge University Press, Cambridge, 1997. doi:10.1017/CBO9781139058520.

[41] R. Guyan, Reduction of stiffness and mass matrices, AIAA journal 3 (2) (1965) 380–380. doi:10.2514/3.2874.

[42] B. Irons, Structural eigenvalue problems-elimination of unwanted variables, AIAA journal 3 (5) (1965) 961–962. doi:10.2514/3.3027.

[43] R. Craig, M. Bampton, Coupling of substructures for dynamic analyses, AIAA journal 6 (7) (1968) 1313–1319. doi:10.2514/3.4741.

[44] K. Karhunen, Über lineare methoden in der wahrscheinlichkeitsrechnung, Annals of Academic Science Fennicae, Series A1 Mathematics and Physics 37 (1946) 3–79.

[45] D. Kosambi, Statistics in function space, Journal of Indian Mathematical Society 7 (1943) 76–88.

[46] M. Loeve, Fonctions Aléatoires du Second Ordre, Processus stochastiques et mouvement Brownien, Gauthier-Villars, Paris, 1948.

[47] M. A. Obukhov, Statistical description of continuous fields, Transactions of the Geophysical International Academy Nauk USSR 24 (1954) 3–42.

[48] V. S. Pougachev, General theory of the correlations of random functions, Izvestiya Akademii Nauk USSR 17 (1953) 1401–1402.

[49] S. Idelsohn, A. Cardona, A reduction method for nonlinear structural dynamic analysis, Computer Methods in Applied Mechanics and Engineering 49 (3) (1985) 253–279. doi:10.1016/0045-7825(85)90125-2.

[50] G. Haller, S. Ponsioen, Exact model reduction by a slow–fast decomposition of nonlinear mechanical systems, Nonlinear Dynamics 90 (1) (2017) 617–647. doi:10.1007/s11071-017-3685-9.

[51] S. Jain, P. Tiso, G. Haller, Exact nonlinear model reduction for a von Kármán beam: slow-fast decomposition and spectral submanifolds, J. Sound Vib. 423 (2018) 195–211. doi:10.1016/j.jsv.2018.01.049.

[52] F. Kogelbauer, G. Haller, Rigorous model reduction for a damped-forced nonlinear beam model: An infinite-dimensional analysis, Journal of Nonlinear Science (2018) 1–42doi:10.1007/s00332-018-9443-4.

[53] N. Kryloff, N. Bogoliuboff, Introduction to Nonlinear Mechanics, Princeton Univ, Press, Princeton, NJ.
URL https://press.princeton.edu/titles/3303.html

[54] G. von Groll, D. Ewins, The harmonic balance method with arc-length continuation in rotor/stator contact problems, Journal of sound and vibration 241 (2) (2001) 223–233. doi:10.1006/jsvi.2000.3298.

[55] B. Cochelin, C. Vergez, A high order purely frequency-based harmonic balance formulation for continuation of periodic solutions, Journal of sound and vibration 324 (1-2) (2009) 243–262. doi:10.1016/j.jsv.2009.01.054.

[56] R. Mickens, Comments on the method of harmonic balance, Journal of Sound and Vibration 94 (3) (1984) 456–460.

[57] T. Breunung, G. Haller, When does a periodic response exist in a periodically forced multi-degree-of-freedom mechanical system?, Nonlinear Dyn. (2019) 1–20doi:https://doi.org/10.1007/s11071-019-05284-z.

[58] J. Slater, A numerical method for determining nonlinear normal modes, Nonlinear dynamics 10 (1) (1996) 19–30. doi:10.1007/bf00114796.

[59] S. Roberts, J. Shipman, Two-point boundary value problems: shooting methods, American Elsevier Publishing Company Inc., New York, 1972. doi:10.2307/2005269.

[60] S. Jain, T. Breunung, G. Haller, Fast Computation of Steady-State Response for Nonlinear Vibrations of High-Degree-of-Freedom Systems, arXiv preprint arXiv:1810.10103.

[61] M. Krack, J. Gross, Harmonic Balance for Nonlinear Vibration Problems, Springer, 2019. doi:10.1007/978-3-030-14023-6.

[62] S. Rao, Mechanical vibrations, sixth edition Edition, Pearson, Hoboken, 2017.

[63] T. Cameron, J. Griffin, An alternating frequency/time domain method for calculating the steady-state response of nonlinear dynamic systems, J Appl Mech 56 (1) (1989) 149–154. doi:10.1115/1.3176036.

[64] T. Detroux, L. Renson, L. Masset, G. Kerschen, The harmonic balance method for bifurcation analysis of large-scale nonlinear mechanical systems, Computer Methods in Applied Mechanics and Engineering 296 (2015) 18–38. doi:10.1016/j.cma.2015.07.017.

[65] A. Cardona, A. Lerusse, M. Géradin, Fast Fourier nonlinear vibration analysis, Comput. Mech. 22 (2) (1998) 128–142. doi:10.1007/s004660050347.

[66] Z. Zhang, Y. Chen, Harmonic balance method with alternating frequency/time domain technique for nonlinear dynamical system with fractional exponential, Appl. Math. Mech. 35 (4) (2014) 423–436. doi:10.1007/s10483-014-1802-9.

[67] J. Sinou, A. Lees, A non-linear study of a cracked rotor, Eur. J. Mech. A-Solids 26 (1) (2007) 152–170. doi:10.1016/j.euromechsol.2006.04.002.

[68] G. Hill, On the part of the motion of the lunar perigee which is a function of the mean motions of the sun and moon, Acta mathematica 8 (1) (1886) 1–36. doi:10.1007/bf02417081.

[69] T. Detroux, J.-P. Noël, L. Virgin, G. Kerschen, Experimental study of isolas in nonlinear systems featuring modal interactions, PLOS One 13 (3) (2018) e0194452. doi:10.1371/journal.pone.0194452.

[70] J.-P. Noël, T. Detroux, L. Masset, G. Kerschen, L. Virgin, Isolated response curves in a base-excited, two-degree-of-freedom, nonlinear system, in: ASME 2015 International Design Engineering Technical Conferences and Computers and Information in Engineering Conference, American Society of Mechanical Engineers, 2015. doi:10.1115/detc2015-46106.

[71] H. Abramson, Response curves for a system with softening restoring force, J. Appl. Mech. 22 (3) (1955) 434–435.

[72] G. Habib, G. Cirillo, G. Kerschen, Uncovering detached resonance curves in single-degree-of-freedom systems, Procedia Eng. 199 (2017) 649 – 656. doi:10.1016/j.proeng.2017.09.116.

[73] J. Sanders, F. Verhulst, J. Murdock, Averaging methods in nonlinear dynamical systems, Appl. Math. Sci 59. doi:10.1007/978-0-387-48918-6.

[74] T. Hill, S. Neild, A. Cammarano, An analytical approach for detecting isolated periodic solution branches in weakly nonlinear structures, Journal of Sound and Vibration 379 (2016) 150–165. doi:10.1016/j.jsv.2016.05.030.

[75] R. Jentzsch, Untersuchungen zur Theorie der Folgen analytischer Funktionen, Acta Mathematica 41 (1) (1916) 219–251. doi:10.1007/bf02422945.

[76] A. Hurwitz, Ueber die Nullstellen der Bessel'schen Function, Mathematische Annalen 33 (2) (1888) 246–266. doi:10.1007/bf01443855.

[77] S. Christiansen, P. Madsen, On truncated Taylor series and the position of their spurious zeros, Applied numerical mathematics 56 (1) (2006) 91–104. doi:10.1016/j.apnum.2005.02.009.